

# Transport durch ein Quantenpunkt-Spinventil

Dissertation zur Erlangung des Grades eines  
DOKTORS DER NATURWISSENSCHAFTEN  
in der Fakultät für Physik und Astronomie der  
Ruhr-Universität Bochum

von

**Matthias Braun, M.A.**

aus Bamberg

Tag der mündlichen Prüfung: 06. 07. 2006

Hauptreferent: Prof. Dr. Jürgen König

Koreferent: Prof. Dr. Herbert Schoeller

Promotionskommission: Prof. Dr. Köhler

Prof. Dr. Zabel

Prof. Dr. Chini



# Transport through a Quantum-Dot Spin Valve

**Matthias Braun, M.A.**

Ruhr-Universität Bochum, Germany



# Contents

<b>1</b>	<b>Introduction to Coulomb Blockade, Tunnel Magnetoresistance and Spin Accumulation</b>	<b>15</b>
1.1	Coulomb Blockade . . . . .	15
1.2	Tunnel magnetoresistance . . . . .	19
1.3	Spin accumulation . . . . .	22
<b>2</b>	<b>The Quantum-Dot Spin Valve</b>	<b>25</b>
2.1	Model Hamiltonian . . . . .	26
2.2	Definition of the tunnel coupling strength . . . . .	28
2.3	Reduced density matrix of the quantum dot . . . . .	29
2.4	Experimental realizations of a quantum-dot spin valve . . . . .	30
<b>3</b>	<b>Dynamics of the Quantum-Dot Charge and Spin</b>	<b>33</b>
3.1	Balancing charge currents . . . . .	34
3.2	Balancing spin currents . . . . .	36
3.2.1	Spin current through one tunnel barrier . . . . .	36
3.2.2	Spin current between lead and quantum dot . . . . .	38
3.2.3	Angular momentum continuity equation . . . . .	40
3.3	Chapter summary . . . . .	40
<b>4</b>	<b>Manipulation and Detection of the Dot Spin via Electrical <math>dc</math>-Transport</b>	<b>41</b>
4.1	Gate voltage effect in linear response regime . . . . .	42
4.2	Bias voltage effect in non-linear regime . . . . .	46
4.3	External magnetic fields and the Hanle effect . . . . .	51
4.3.1	Antiparallel aligned lead magnetizations . . . . .	52
4.3.2	Magnetic field applied along $\hat{\mathbf{n}}_L + \hat{\mathbf{n}}_R$ . . . . .	54
4.4	Chapter summary . . . . .	55

<b>5</b>	<b>Time Resolved Spin Dynamics via Frequency Dependent Current Noise</b>	<b>57</b>
5.1	Introduction . . . . .	57
5.2	Diagrammatic Technique . . . . .	59
5.2.1	Quantum-dot density matrix . . . . .	59
5.2.2	Current . . . . .	62
5.2.3	Current-current correlation . . . . .	63
5.2.4	Low-frequency noise in the sequential-tunnel limit . . . . .	65
5.2.5	Technical summary . . . . .	66
5.3	Results . . . . .	67
5.3.1	Zero-frequency noise . . . . .	68
5.3.2	Finite-frequency noise and weak magnetic fields . . . . .	70
5.3.3	Limit of strong magnetic fields . . . . .	75
5.3.4	Influence of spin relaxation . . . . .	79
5.4	Chapter summary . . . . .	80
<b>6</b>	<b>Correspondence of a Quantum-Dot Spin Valve to a Double Quantum Dot</b>	<b>83</b>
6.1	Introduction . . . . .	83
6.2	Mapping of the double dot on a spin valve . . . . .	84
6.3	Model Hamiltonian . . . . .	86
6.4	Kinetic equations . . . . .	87
6.5	Discussion . . . . .	89
6.5.1	Current-voltage characteristics . . . . .	90
6.5.2	Stability diagrams . . . . .	92
6.6	Chapter summary . . . . .	96
<b>7</b>	<b>Faraday-Rotation Fluctuation Spectroscopy</b>	<b>97</b>
7.1	Introduction . . . . .	97
7.2	Experimental setup . . . . .	98
7.2.1	The experiment of Crooker <i>et al.</i> . . . . .	99
7.2.2	The experiment of Oestreich <i>et al.</i> . . . . .	99
7.3	Theoretical description . . . . .	99
7.4	Spin life time and line broadening . . . . .	103
7.4.1	Spin-orbit coupling . . . . .	103
7.4.2	Hyperfine interaction . . . . .	104
7.4.3	Inhomogeneous line broadening . . . . .	104

7.5	Proposal to reduce inhomogeneous broadening . . . . .	105
7.6	Connection to quantum computation . . . . .	109
7.7	Chapter summary . . . . .	111
<b>8</b>	<b>Conclusions</b>	<b>113</b>
<b>A</b>	<b>Green's Functions of the Quantum Dot</b>	<b>117</b>
<b>B</b>	<b>Generalized Transition Rates for a Quantum-Dot Spin Valve</b>	<b>121</b>
B.1	Choice of reference frame . . . . .	121
B.2	Diagrammatic calculation of the matrix $\mathbf{W}$ . . . . .	122
<b>C</b>	<b>Master Equations for the Double-Dot Problem</b>	<b>125</b>
C.1	Diagrammatic rules . . . . .	125
C.2	System of master equations . . . . .	129
<b>D</b>	<b>Calculation of the Spin-Spin Correlation Function</b>	<b>133</b>





# Publications

The following parts of the presented work were already published

**Matthias Braun and Jürgen König**

*Proposal to Measure the Spin Coherence Time  $T_2$  with Reduced Inhomogeneous Broadening by Faraday-Rotation Fluctuation Spectroscopy,*

cond-mat/0601607

contains parts of Chapter 7

**Matthias Braun, Jürgen König and Jan Martinek**

*Current Noise in a Quantum-Dot Spin Valve,*

cond-mat/0601366

contains parts of Chapter 5

**Matthias Braun, Jürgen König, and Jan Martinek**

*Manipulating Single Spins in Quantum Dots Coupled to Ferromagnetic Leads,*

cond-mat/0512519, to be published in Lecture Notes in Physics

contains parts of Chapter 3, and 4

**Bernhard Wunsch, Matthias Braun, Jürgen König, and Daniela Pfannkuche**

*Probing Level Renormalization by Sequential Transport Through Double Quantum Dots,*

Physical Review B **72**, 205319 (2005), cond-mat/0508458

contains parts of Chapter 6

**Matthias Braun, Jürgen König, and Jan Martinek**

*Spin Current Through a Tunnel Junction,*

Superlattices and Microstructures **37**, 333 (2005), cond-mat/0411562

contains parts of Chapter 3

**Matthias Braun, Jürgen König, and Jan Martinek**

*Hanle Effect in Transport through Quantum Dots Coupled to Ferromagnetic Leads,*

Europhysics Letters **72**, 294 (2005), cond-mat/0411477

contains parts of Chapter 4

**Matthias Braun, Jürgen König, and Jan Martinek**

*Theory of Transport through Quantum-Dot Spin Valves in the Weak-Coupling Regime,*

Physical Review B **70**, 195345 (2004), cond-mat/0404455

contains parts of Chapter 3



# Deutsche Zusammenfassung

Zentrales Thema dieser Arbeit ist die theoretische Untersuchung von Spintransport durch Nanostrukturen, in denen es zu starker Elektron-Elektron-Wechselwirkung kommt. Als Modellsystem betrachten wir einen Quantenpunkt mit einem einzelnen Energieniveau, der über Tunnelkontakte schwach an ferromagnetische Zuleitungen gekoppelt wird. Eine solche Struktur nennen wir Quantenpunkt-Spinventil.

Diese Arbeit liegt im Überschneidungsbereich der Themenkreise Spinelektronik und Transport durch Nanostrukturen. Ein Quantenpunkt-Spinventil zeigt sowohl die Ladungseffekte wie Coulomb-Blockade eines gewöhnlichen Quantenpunktes, aber auch die spinabhängigen Phänomene Spinakkumulation und Tunnelmagnetowiderstand, welche von magnetischen nichtwechselwirkenden Strukturen bekannt sind. Zusätzlich zu den bereits bekannten Effekten kann man in einem Quantenpunkt-Spinventil ein weiteres Phänomen beobachten, das aus dem Wechselspiel von spinabhängigen Tunneln und starker Ladungswechselwirkung entsteht: eine intrinsische Koppelung des Spins auf dem Quantenpunkt an die Kontaktmagnetisierungen, die zu einer Präzession des Quantenpunktspins führen kann. Die starke Wechselwirkung der Leitungselektronen innerhalb des Quantenpunktes beeinflusst daher den Spintransport nicht nur indirekt über ihren Einfluss auf den Ladungstransport, sondern auch direkt durch diesen Vielteilcheneffekt. Das ist die Kernaussage dieser Dissertation.

Ein Quantenpunkt verstärkt die elektromagnetische Wechselwirkung zwischen Leitungselektronen durch seine geringe Kapazität. Mit abnehmender Kondensatorgröße verringert sich auch dessen Kapazität und die Ladungsenergie pro Elektron  $E_C = e^2/2C$  steigt. Dieser Zusammenhang wird im Quantenpunkt ausgenutzt. Wenn die Längenskala des Quantenpunktes nur noch die Größenordnung von Nanometern (nm) beträgt, besitzt er eine Kapazität der Größe  $C = 10^{-15}$  Farad. Bei einer solch geringen Kapazität übersteigt die nötige Energie, um auch nur eine einzelne Elektronenladung von  $e \approx 1.602 \times 10^{-19}$  Coulomb auf den Quantenpunkt aufzubringen, die Energieskala der Temperatur. In diesem Falle führt die klassische Ladungsenergie des Quantenpunktes zu stark korreliertem Transport. Durch das Anlegen einer passenden Gatterspannung kann ein Quantenpunkt in die so genannte Coulomb-Blockade getrieben werden. Dann blockiert die Ladungsenergie weiteren Transport durch den Punkt, und die Leitfähigkeit des Bauteils wird stark reduziert. Deshalb fallen Quantenpunkte auch in die Klasse der Einzel-Elektronen-Transistoren.

Durch die ferromagnetische Ordnung in den Zuleitungen zu dem Quantenpunkt ist deren Zustandsdichte an der Fermienergie spinabhängig. Daher sind auch die Tunnelraten zwischen dem Quantenpunkt und den magnetischen Kontakten selbst spinabhängig, und damit der Tunnelstrom spinpolarisiert. In einem gewöhnlichen Spinventil befinden sich zwei Ferromagnete in direktem Kontakt über nur eine einzelne Tunnelbarriere. Die Leitfähigkeit dieser Kontaktstelle wird durch die relative Ausrichtung der beiden Kontaktmagnetisierungen beeinflusst. Für parallele Magnetisierungen ist der elektrische Widerstand normalerweise geringer als für anti-parallele Magnetisierungen. Dieses Phänomen, welches technologisch z.B. in modernen Festplattenleseköpfen eingesetzt wird, bezeichnet man als Tunnelmagnetowiderstand.

In einem Quantenpunkt-Spinventil sind die beiden ferromagnetischen Zuleitungen durch einen einzelnen Quantenpunkt getrennt. Um in diesem Bauteil Tunnelmagnetowiderstand zu beobachten muss die Spininformation von einem ferromagnetischen Kontakt durch den Quantenpunkt zum anderen Kontakt übertragen werden. Dies geschieht durch Nichtgleichgewichts-Spinakkumulation. Beim Anlegen einer Durchlassspannung führen die spinabhängigen Tunnelraten zur Akkumulation von Spin auf dem ansonsten nichtmagnetischen Quantenpunkt. In diesem Fall gleicht ein einzelnes Quantenpunkt-Spinventil zwei gewöhnlichen Spinventilen, die in Serie geschaltet wurden. An jeder der beiden Tunnelbarrieren, zwischen dem Ferromagneten auf der einen Seite und dem akkumulierten Spin auf der anderen, tritt ein Tunnelmagnetowiderstand auf. Daher ist der Strom durch das Quantenpunkt-Spinventil durch den Spinzustand des einzelnen Niveaus im Quantenpunkt bestimmt. Da die Richtung des akkumulierten Spins nicht statisch ist, sondern sich den äußeren Gegebenheiten anpasst, kann der Spin als Messinstrument verwendet werden, um den Einfluss der Ladungswechselwirkung auf den Spintransport zu beobachten.

Durch die Tunnelkopplung eines einzelnen Energieniveaus in einem Quantenpunkt an einen metallischen Kontakt kommt es zu einer Renormierung dieses Energieniveaus. Wenn der Kontakt ferromagnetisch ist, wird diese Renormierung spinabhängig, was zu einer Zeeman-ähnlichen Aufspaltung des Niveaus führt. Deshalb kann man diese Renormierung als eine Art magnetisches Austauschfeld betrachten. Im Kontext von Spintransport wird diese Renormierung durch eine neue Spinstromkomponente beschrieben. Die Ausrichtung dieses Spinstroms ist transversal zur Kontaktmagnetisierung wie auch transversal zum Quantenpunkts spin. Dieser Austauschmechanismus ist abhängig von der Gatter- wie von der Durchlassspannung. Deshalb kann man über diesen Vielteilcheneffekt den Spinfreiheitsgrad des Quantenpunktes direkt mit der angelegten Spannung ansteuern.

Um den Quantenpunkts spin zu beeinflussen kann natürlich auch direkt ein externes magnetisches Feld verwendet werden. In diesem Magnetfeld präzediert der Quantenpunkts spin, was die Entstehung von Tunnelmagnetowiderstand unterdrückt. Mittels Messung der Leitfähigkeit des Quantenpunkt-Spinventils als Funktion des angelegten magnetischen Feldes kann man die Spinkohärenzzeit des Quantenpunktes bestimmen. Eine solches Experiment stellt eine elektrische Realisierung einer optischen Hanle-Messung an einem einzelnen Quantenpunkt dar.

Die Arbeit gliedert sich wie folgt. Im Kapitel 1 werden die dem Quantenpunkt-Spinventil zugrunde liegenden physikalischen Phänomene wie Coulomb Blockade, Spinakkumulation und Tunnelmagnetowiderstand eingeführt. Die Struktur des Quantenpunkt-Spinventils selber wird in Kapitel 2 besprochen. Dieses Kapitel geht auch auf die große Auswahl von Realisierungsmöglichkeiten eines solchen Systems ein. Im Kapitel 3 wird beschrieben, wie sich Spin und Ladung auf dem Quantenpunkt an die äußeren Rahmenbedingungen anpassen. Zuerst wird der Spin- und der Ladungsstrom durch eine Tunnelbarriere streng mathematisch abgeleitet. Danach berechnen wir den statischen Spin und die Ladung auf dem Quantenpunkt durch deren jeweilige Kontinuitätsgleichung. Der sozusagen erzeugte Quantenpunktspin kann dann über seinen Einfluss auf die Gleichstromleitfähigkeit ausgelesen werden, was im Kapitel 4 diskutiert wird. Während die Gleichstromleitfähigkeit den zeitgemittelten Quantenpunktspin mißt, kann eine Messung des Stromrauschens auch die zeitabhängige Präzession einzelner Elektronenspins detektieren (siehe Kapitel 5).

Unsere physikalische Vorhersagen sind nicht nur auf ein Spinsystem anwendbar, sondern auf jedes tunnelkontaktierte Zweiniveausystem. Zur Verdeutlichung dieses Punktes untersuchen wir im Kapitel 6 den Transport durch zwei Quantenpunkte, die in Serie geschaltet sind. In diesem System sind die relevanten Zustände nicht “spin-up” und “spin-down”, sondern “Elektron links” und “Elektron rechts”.

Im Kapitel 7 widmen wir uns schließlich der Möglichkeit, den Quantenpunktspin nicht nur mittels Transportmessungen durch ferromagnetische Zuleitungen zu detektieren, sondern auch optisch mittels Faraday-rotations-fluktuations-Spektroskopie. Hierzu präsentieren wir eine theoretische Beschreibung von kürzlich veröffentlichten Experimenten. Darüber hinaus schlagen wir eine Modifikation dieser Experimente vor, die es gestattet die inhomogene Verbreiterung zu reduzieren, welche ansonsten die Messung der Spinkohärenzzeit  $T_2$  verfälscht.

Am Ende der Arbeit fassen wir unsere Hauptergebnisse im Kapitel 8 zusammen.



# Introduction

The scope of this work will be the study of spin transport through nanostructures, which exhibit strong charge interaction. Therefore, we theoretically discuss the simplest non-trivial model system which is a single-level quantum dot weakly tunnel coupled to two ferromagnetic leads. We call this structure a *quantum-dot spin valve*.

The work presented here resides at the intersection of the two highly-interesting and extensively-pursued research fields of spintronics on the one hand and transport through strongly-interacting nanostructures on the other hand. A quantum-dot spin valve shows charge-related physical phenomena, like Coulomb blockade, which are known for non-magnetically contacted quantum dots. Furthermore it also shows spin-related effects like spin accumulation and tunnel magnetoresistance, just like non-interacting magnetic structures would do. In addition to these already known effects, the strong charge interaction leads to a new phenomena, to an intrinsic coupling of the dot spin to the lead magnetizations, which can be an intrinsic source of spin precession on the quantum dot. In other words, the charge interaction does not only affects spin transport indirectly, via modifying the charge transport, but directly via a many-body effect. This is the key observation in this thesis.

The quantum dot amplifies the charge interaction between conduction electrons by its small capacity. The device makes use of the fact, that with shrinking system size, also the capacity  $C$  decreases, and the charging energy  $E_C = e^2/2C$  per excess electron increases. For an island with a length scale of the order of nanometer (nm), typical capacities are of the order of  $C = 10^{-15}$  Farad. Then, the charging energy even for a single excess electron charge  $e \approx 1.602 \times 10^{-19}$  Coulomb can exceed the energy scale set by temperature. In this regime, the interaction strongly correlates electronic transport through the device. By applying an appropriate gate voltage, the device can also be tuned to the so called *Coulomb blockade regime*, where this charging energy blocks transport. Due to this functionality, to change the conductance by a gate voltage, quantum dots are also referred to as single-electron transistors.

The ferromagnetic leads bear a spin-dependent density of states at the Fermi energy. Since the tunnel rates through a barrier depend on these density of states, also the tunnel rates get spin dependent. In this way, the lead magnetizations cause a spin polarization of the current, which crosses a tunnel barrier. In an ordinary *spin valve*, two ferromagnets

are directly in contact via a single tunnel barrier. Thereby the conductance of the junction depends on the alignment of the magnetizations. For a parallel alignment, the conductance is usually higher than for an antiparallel alignment. This phenomena is called tunnel magnetoresistance, and it already has technological applications for example in magnetic read heads in modern hard drives.

In the quantum-dot spin valve, the two ferromagnets are separated by a non-magnetic quantum dot. To observe magnetoresistance in this device, the information about the magnetization direction of one ferromagnetic lead must somehow be transmitted to the other lead through the quantum dot. This can happen via a non-equilibrium spin on the quantum dot. In the presence of a bias voltage applied at the ferromagnetic leads, the spin dependence of the tunnel rates causes non-equilibrium spin accumulation on the single-level quantum dot. In this case, one quantum-dot spin valve resembles two ordinary spin valves connect in series. At each interface, between a magnetized lead and the polarized dot state, tunnel magnetoresistance occurs. In this way electronic transport through the quantum-dot spin valve is governed by the behavior of the *single electron spin* inside the dot. Since the direction of dot-spin accumulation is not static, but adapts according to the circumstances, the dot spin can be utilized for the detection of the influence of the strong charge interaction on spin transport.

By tunnel coupling a single electronic level with strong charge interaction to a lead, the level experiences a renormalization of its energy. In the case of a ferromagnetic lead, this renormalization depends on the spin degree of freedom, resulting in a Zeeman-like spin splitting of the single level. This splitting can be interpreted as a magnetic-like exchange field. Having the transfer of angular momentum in mind, this level renormalization can be seen as a component of the spin current, which is perpendicular to both, the lead magnetization and the dot spin. This exchange interaction sensitively depends on system parameters such as gate and bias voltage. Therefore the voltages, via the exchange field dependences, also provide suitable handles to *manipulate* the quantum-dot spin.

However, also an externally applied magnetic field can directly *manipulate* the dot spin. In such an applied magnetic field, the dot spin precesses, which reduces the magnetoresistance of the device. By recording the increase of the conductance as response to the external magnetic field, which turns out to be an all electrical realization of an optical Hanle experiment, one can determine the spin-coherence time in a quantum dot.

The outline of this dissertation is as follows. Chapter 1 contains a general introduction to transport through quantum dots, spin accumulation, and tunnel magnetoresistance. The quantum-dot spin-valve structure is introduced in Chapter 2. This Chapter also discusses the different possible physical realizations of such a device. In Chapter 3 the dynamics of the dot spin and charge is addressed. Starting from a rigid calculation of the spin and charge current through each tunnel junction, the master/Bloch equation for the charge/angular momentum degree of freedom is constructed from the charge/spin continuity equation. From the Bloch equation we discuss how to prepare and manipulate the dot spin via bias voltage, gate voltage, and an externally applied magnetic field. The dot spin can be



detected by its imprint on the  $dc$ -conductance of the spin valve as shown in Chapter 4. While the  $dc$ -conductance is an adequate experimental tool to access the time averaged dot spin, the spin precession of the individual electrons, tunneling through the device, can be examined via the frequency dependent current noise as discussed in Chapter 5.

The spin of the quantum dot represents a generic two level system. Therefore, the physical predictions for the quantum-dot spin valve can also be translated to different contexts, for example to transport through double quantum dots. To demonstrate this point, we examine the serial double quantum-dot system in Chapter 6.

In Chapter 7 we discuss the possibility, to detect the spin dynamics not only by transport but also in an optical way, namely by Faraday-rotation fluctuation spectroscopy. We theoretically describe recent experiments and furthermore propose a modification of this experimental technique, which allows one to measure the spin relaxation time  $T_2$  in semiconductors with reduced inhomogeneous broadening.

Finally, in Chapter 8 we summarize the main results presented in this work.



# Chapter 1

## Introduction to Coulomb Blockade, Tunnel Magnetoresistance and Spin Accumulation

In this Chapter we give an elementary introduction to the different physical effects, appearing simultaneously in a quantum-dot spin-valve device.

### 1.1 Coulomb Blockade

The most elementary device to examine the quantization of charge in a transport experiment is the single-electron transistor (SET). The device consists of an island, either metallic or semiconductor, which is contacted by tunnel barriers to two leads, see Fig. 1.1.

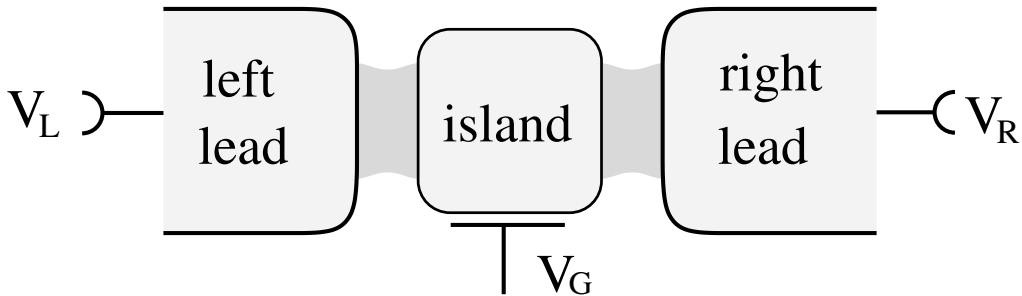


Figure 1.1: A single-electron transistor.

A current can be driven through the island by applying a bias voltage  $V = V_L - V_R$ . With a gate voltage  $V_G$  the electrochemical potential of the island can be controlled. If the

size of the island, and therefore its capacity is sufficiently small, the energy to charge the island with a single electron can exceed the energy scale set by temperature. In this regime, the classical charging energy causes a strong interaction between the excess electrons on the dot, which severely modifies the transport behavior of the SET device.

In the simplest case, a small applied bias voltage transfers electrons one by one through the structure, see Fig. 1.2. If the island is empty, an electron from the source (left) electrode can tunnel in. Due to the electrostatic repulsion, no other electron can tunnel onto the island, as long as this one excess electron is occupying the central region. The electron must first leave the island to the drain (right) lead, before the next transport cycle can start. This transport mechanism is named *sequential tunneling* of electrons, and is described by the so called *orthodox theory* [1–3].

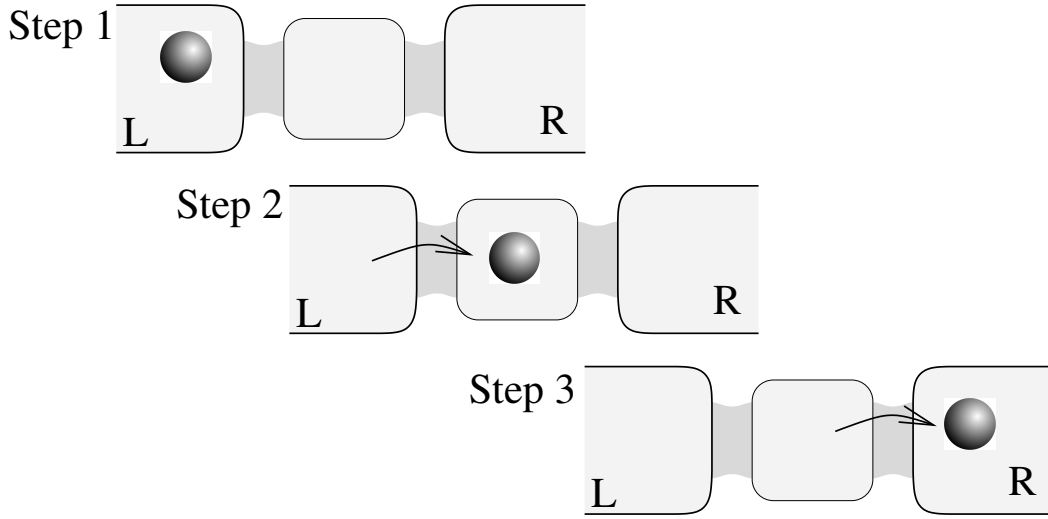


Figure 1.2: By sequential tunneling, an electron is transferred through the single-electron transistor. Thereby, charge interaction prohibits the island to be occupied by two excess electrons at any time.

The charging energy of the island is given by its total capacity, which is the sum of the capacities of the tunnel barriers  $C_L$  and  $C_R$ , as well as the capacity to the gate electrode  $C_G$ . By applying a gate and bias voltage, the energetically most favorable excess charge on the island equals  $en_x = C_L V_L + C_R V_R + C_G V_G$ . The charging energy of the island is then a function of the externally imposed charge  $n_x$  and the natural number  $N$  of excess electrons on the island

$$E_{ch}(N, n_x) = \frac{e^2}{2C}(N - n_x)^2, \quad (1.1)$$

together with additional (but unimportant) terms, which are independent of  $N$ . When at a fixed  $n_x$  the island is occupied by  $N$  electrons, an incoming electron from the source

(left) lead must bear at least the energy  $E_{ch}(N+1, n_x) - E_{ch}(N, n_x)$  to enter the island, see Fig. 1.3, otherwise the tunnel event into the island is energetically forbidden.

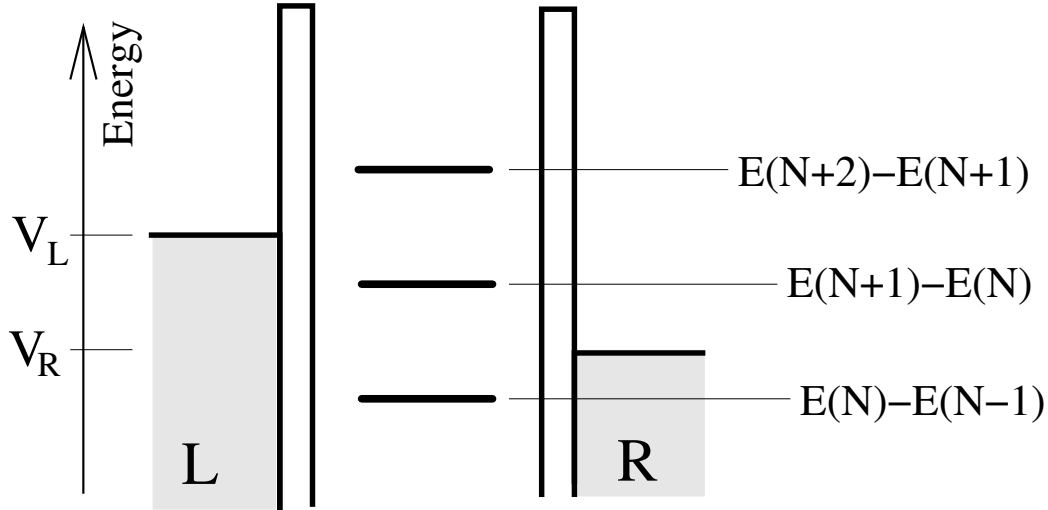


Figure 1.3: Energy profile of the quantum-dot structure.

At this point, the size of the island becomes relevant. If the size of the island is large compared to the Fermi wave length, the density of states of the island is continuous, i.e., the island has metallic character. In this regime, the electrons need an energy equal or larger than  $E_{ch}(N+1, n_x) - E_{ch}(N, n_x)$  to be able to tunnel onto the island. In this work, we consider the opposite regime, where the size of the island is comparable to the Fermi wave length. Due to the strong spatial confinement, quantum mechanical momentum quantization yields a discrete energy spectrum of the island. Therefore the incoming electrons must bear exactly the energy  $E_{ch}(N+1, n_x) - E_{ch}(N, n_x)$  to enter the island. Such a structure with a discrete density of states is usually referred as quantum dot. In the following work, we will exclusively discuss quantum dots.

The notion of such a device as a ‘transistor’ is motivated by the fact, that the current through the device can be affected by gate voltage  $V_G$  via an effect called ‘Coulomb blockade’. When transport is possible through the quantum dot depends on the condition, that an electronic level of the dot lies within the energy window defined by the source and drain chemical potential, see Fig. 1.4. If a dot state lies within this window, an electron from the source electrode can tunnel onto the dot, and subsequently tunnel out to the drain lead. If no electronic state lies within this energy window, all dot levels below the leads’ Fermi energies are occupied by electrons, while all levels above are empty. The number of electrons on the island is fixed, and transport is suppressed by *Coulomb blockade*.

For small bias voltage, the differential conductance  $G = \partial I / \partial V|_{V=0}$  of a quantum dot exhibit *Coulomb oscillations* as a function of the applied gate voltage  $V_G$ , see Fig. 1.5. At

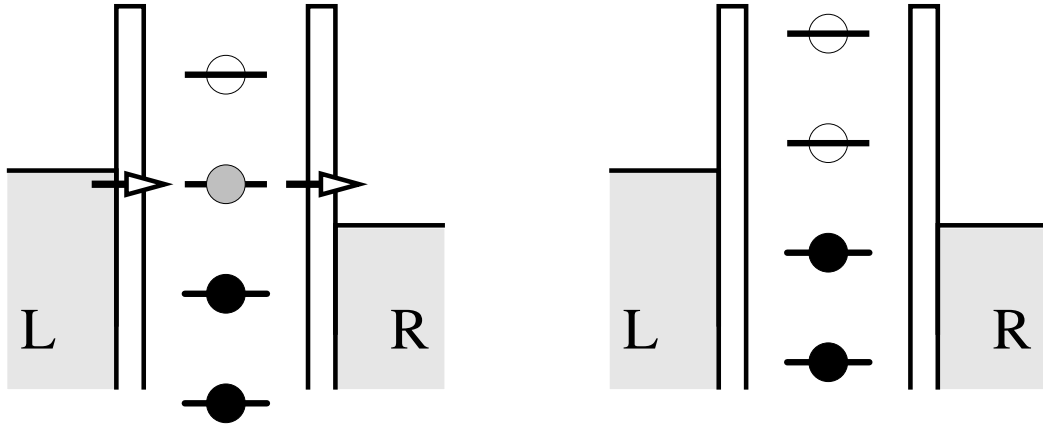


Figure 1.4: If a dot state lies within the bias voltage window of the leads, current can cross the quantum dot. If no level is available in this window, the charge of each dot level is fixed to be either zero or one, and electrostatic charging energy prohibits charge transport. This is called Coulomb blockade.

fixed bias voltage, the electronic structure of the dot can be shifted in energy proportional to  $V_G$ . Each time, a dot level coincides with the leads' Fermi surface, a conductance peak arises. Therefore the differential conductance maps the electronic structure of the quantum dot.

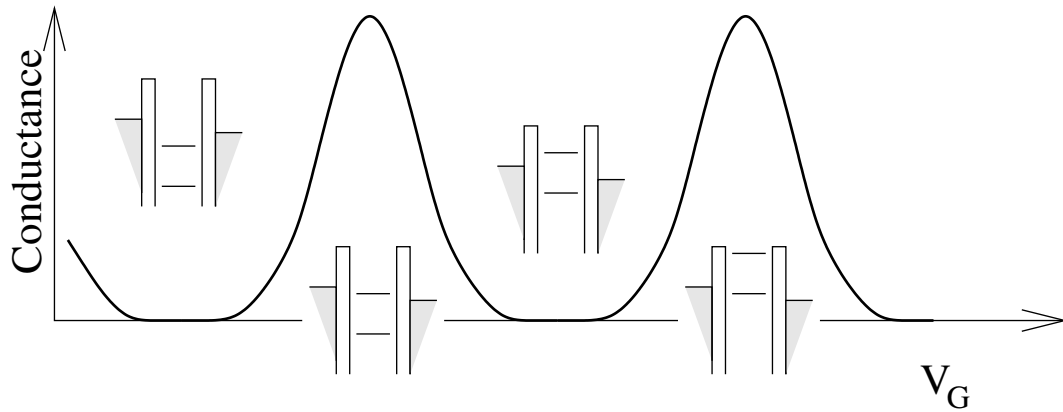


Figure 1.5: The conductance as function of the gate voltage shows Coulomb oscillations. Each time, an electronic level coincides with the leads' Fermi energy, electrons can pass through the device.

There are several different realizations of such a single-electron transistor possible. The most common realization, which was also one of the systems where Coulomb blockade was first observed by Fulton and Dolan in 1987 [4], is a lithographically patterned metallic is-

land. The currently best controlled way to form quantum dots is, to take a two-dimensional electron gas in a semiconductor heterostructure, and pattern the dot by top gate electrodes. This method was first demonstrated by Scott-Thomas *et al.* [5]. However there exist a variety of different methods to form SETs like molecular islands such as carbon nanotubes. For selected reviews, see Ref. [6].

## 1.2 Tunnel magnetoresistance

Spintronics, or spin electronics, refers to the idea of employing not only the charge of electrons but also their spin for certain device operations. This idea covers quite a broad field of research, see for examples the reviews by Prinz [7], Wolf *et al.* [8], or Zutic *et al.* [9]. Here we focus on one of the most important concepts of spintronics, to generate electrical resistance changes, so called magnetoresistance effects, by the use of spin polarized conduction electrons.

The simplest way to generate magnetoresistance effects is to use ferromagnetic materials. Due to the ferromagnetic order in this materials, an internal field of the order of Tesla arises, which significantly influences the band structure. Therefore relevant material parameters like density of states, Fermi wave length or mobility depend on the spin degree of the electrons. The Fig. 1.6 shows typical density of states of a  $3d$ -ferromagnetic metal, since especially the ferromagnetic elements Fe, Co, and Ni have technological relevance: they are stable at room temperature, cheap, and can be processed reliably.

There exist different types of magnetoresistance effects. The most important ones are the giant magnetoresistance (GMR) [10,11] and the tunnel magnetoresistance (TMR) [12]. If two ferromagnetic layers are separated by a thin conducting non-magnetic layer in the case of GMR, and by a tunnel barrier in the case of TMR, the resistance of the junction depends on the relative alignment of the magnetization directions. The device resistance is small for parallel magnetizations, and increases for antiparallel aligned magnetizations.

The magnetoresistance effects have already technological applications. By pinning one layer, and letting the other ferromagnetic layer align freely with an external magnetic field, the device acts as magnetic field sensor. If the free layer has two preferred alignments, leading to a stable high or low resistance state, the device can be used as non-volatile memory cell, creating a magnetic random access memory (MRAM) [13,14]. While the sensing device is already in use in modern hard drives, and as rev meter in anti-lock breaking systems, MRAMs are expected to become ready for market in the next years.

The first measurement of tunnel-magnetoresistance in a single  $F/I/F$  junction was reported by Jullière [12], and reproducibly observed by Maekawa and Gäfvert [15]. The study of tunnel magnetoresistance became technological relevant when Miyazaki *et al.* [16] and Moodera *et al.* [17] developed devices, which showed reasonable tunnel magnetoresistance at room temperature.

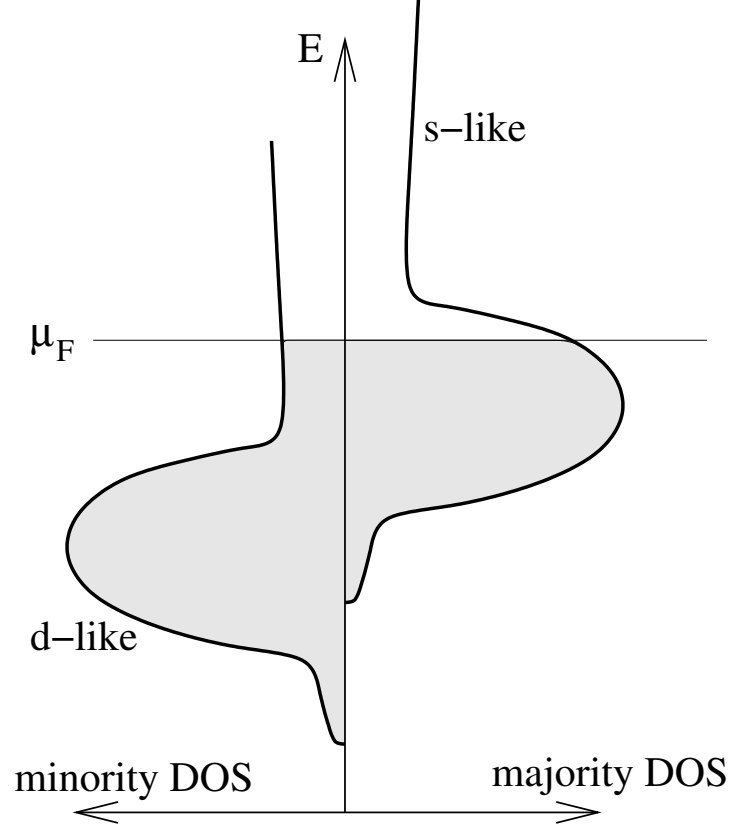


Figure 1.6: Typical density of states of a 3d-ferromagnetic metal. The internal field shifts the band structure of spin up and spin down electrons against each other. This causes a different density of states of the two spin components at the Fermi energy  $\mu_F$ .

In order to interpret his measurement, Jullière proposed, that for each spin channel  $\sigma$ , the tunnel probability is proportional to the density of states (DOS)  $\rho_{\sigma r}(E_F)$  in the source ( $r = L$ ) lead, and in the drain ( $r = R$ ) lead. For parallel aligned ferromagnets, the current is therefore proportional to the product of the DOS in the two leads

$$I_{\uparrow\uparrow} \propto \rho_{\uparrow L}(E_F) \rho_{\uparrow R}(E_F) + \rho_{\downarrow L}(E_F) \rho_{\downarrow R}(E_F), \quad (1.2)$$

and similar for an antiparallel alignment

$$I_{\uparrow\downarrow} \propto \rho_{\uparrow L}(E_F) \rho_{\downarrow R}(E_F) + \rho_{\downarrow L}(E_F) \rho_{\uparrow R}(E_F). \quad (1.3)$$

From the spin dependence of the DOS in ferromagnets  $\rho_{\uparrow r}(E_F) > \rho_{\downarrow r}(E_F)$  directly follows the occurrence of tunnel magnetoresistance since  $I_{\uparrow\uparrow} > I_{\uparrow\downarrow}$ .

In the parallel case, the main contribution of the current is carried by electrons tunneling from a majority state in the source lead to a majority state in the drain lead. In the antiparallel case, transport must occur either through the minority states in the source



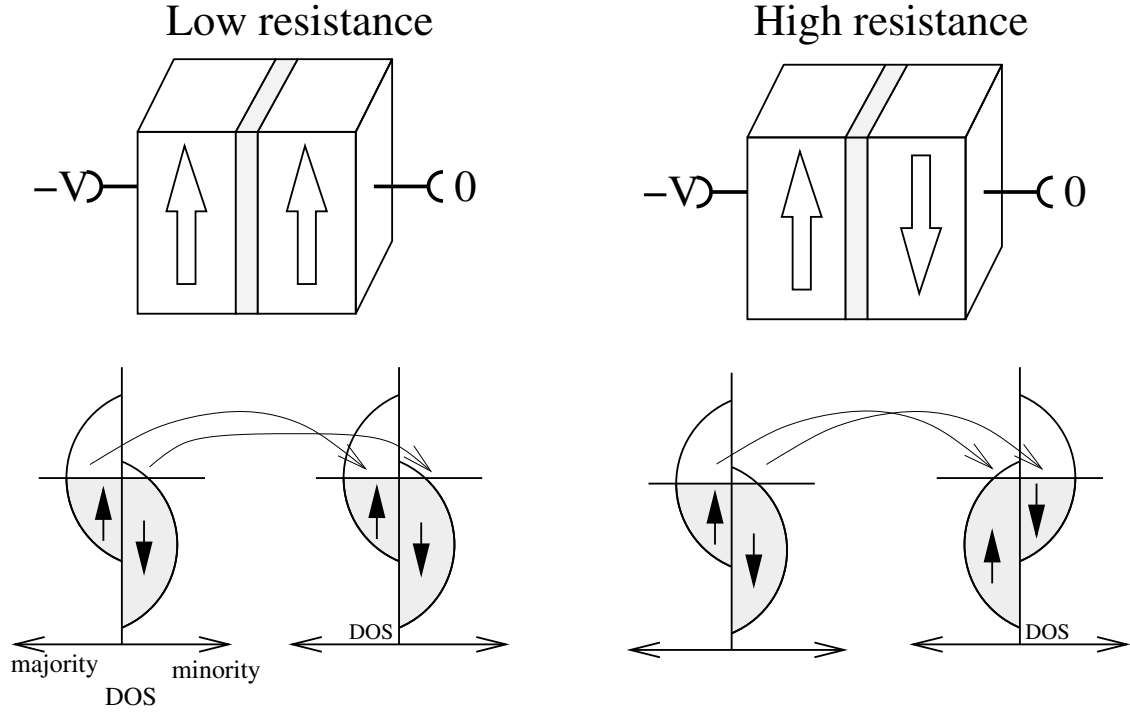


Figure 1.7: Tunnel magnetoresistance is caused by the spin dependence of the density of states at the Fermi energy.

lead or the minority states in the drain lead. Quantitatively, the tunnel magnetoresistance is described by the TMR-ratio

$$\text{TMR} = \frac{I_{\uparrow\uparrow} - I_{\uparrow\downarrow}}{I_{\uparrow\downarrow}} = \frac{2p_L p_R}{1 - p_L p_R}, \quad (1.4)$$

where  $p_r = (\rho_{\uparrow r} - \rho_{\downarrow r})/(\rho_{\uparrow r} + \rho_{\downarrow r})$  describes the degree of spin polarization of the respective lead at the Fermi edge. A non-magnetic lead would bear a polarization of  $p_r = 0$ , and  $p_r = 1$  corresponds to a half metallic lead, carrying majority spins only. Jullière's model was extended by Sloncewski [18], to describe spin valves with arbitrary angles between the magnetization directions of the two layers. If the two magnetizations enclose an arbitrary angle  $\phi$ , the probability of a majority-source electron to tunnel in a majority-drain state is proportional to  $\cos^2(\phi/2)$ , and its probability to tunnel in a minority-drain state equals  $\sin^2(\phi/2)$ . These coefficients just reflect the projection of the spin state of the electron in the source lead on the drain lead magnetization direction. The tunnel magnetoresistance then becomes

$$\frac{I(\phi) - I_{\uparrow\downarrow}}{I_{\uparrow\downarrow}} = \frac{2p_L p_R}{1 - p_L p_R} \cos^2 \frac{\phi}{2}. \quad (1.5)$$

This cosine-like angular dependence of the tunnel magnetoresistance was experimentally observed by Moodera *et al.* [19] and Jaffrès *et al.* [20]. It is worth to mention, that Sloncewski's model of tunnel magnetoresistance is a very crude one, which neglects for example any sort of interface effects. Therefore the model is more suitable to understand the general tendency rather than to make quantitative prediction. For latter, more sophisticated theories are required like a spin mixing conductance approach [21].

### 1.3 Spin accumulation

Another important concept of spintronics will appear in a quantum-dot spin valve: spin accumulation. Consider a large (non-interacting) metallic region, which has two ferromagnetic contacts, and the magnetizations of the contacts are aligned antiparallel, see Fig. 1.8. In this structure, we can assume, that electrons with an up spin are completely independent from electrons with down spin [22, 23]. If a bias voltage is applied at the contacts, the chemical potential of the middle region will adjust in such a way, that the incoming particle flow from the left lead will be equal to the outgoing flow to the right lead.

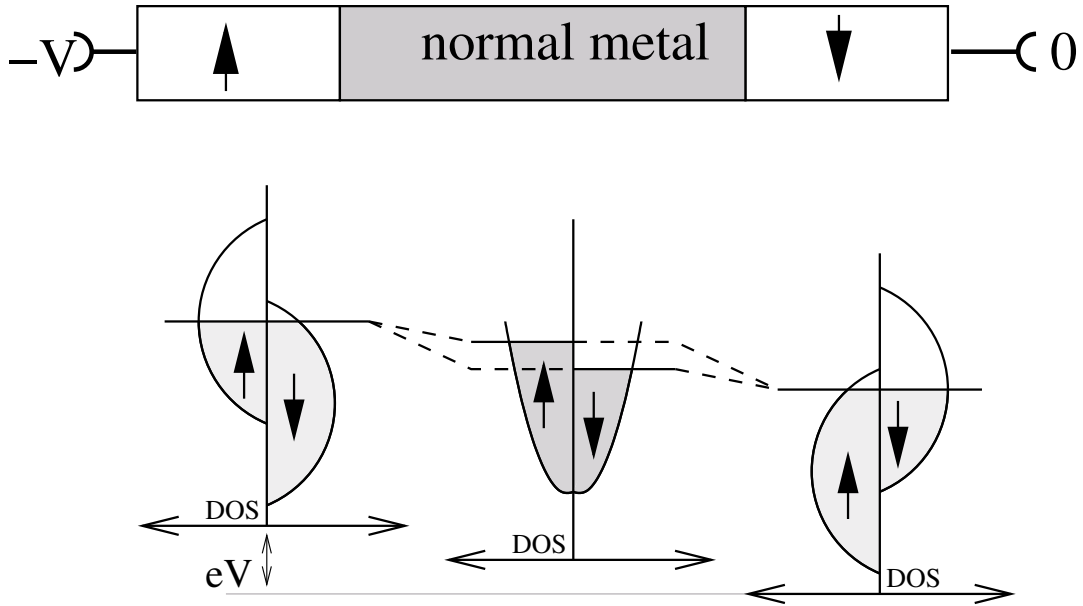


Figure 1.8: Due to the spin dependent interface resistances, electrons with up and down spins have different Fermi energies on the island.

The current through each interface is given by the respective voltage difference and interface resistance. Due to magnetoresistance, these interface resistances differ for the two spin channels. For one spin component the left interface is more transparent than the

right, for the other spin, the right is more transparent than the left. Therefore the chemical potential on the island is different for the two spin components, i.e., one spin component accumulates on the island. This effect was first observed by Johnson *et al.* [24] in an Al bar contacted by Fe leads, and nowadays spin accumulation is extensively studied, see for example Ref. [25]. It is worth to mention, that spin accumulation is a non-equilibrium effect, i.e., it vanishes without bias voltage.



## Chapter 2

# The Quantum-Dot Spin Valve

A quantum-dot spin valve consists of a single-level quantum dot, which is tunnel contacted to ferromagnetic leads, see Fig. 2.1. The direction of magnetization of the lead  $r$  ( $r = L/R$ ) is given by the vector  $\hat{\mathbf{n}}_r$ . Further, gate and bias voltage can be applied. The latter can cause the accumulation of a non-equilibrium spin  $\mathbf{S}$  on the dot. Since the tunnel barrier capacitances scale only linearly with contact area and thickness, they are often fabricated in a controlled fashion. Therefore, for simplicity, we assume, that the capacitance of the left and right tunnel contact is equal. The bias voltage drop over the two barriers is then symmetric and equals  $\pm V/2$ .

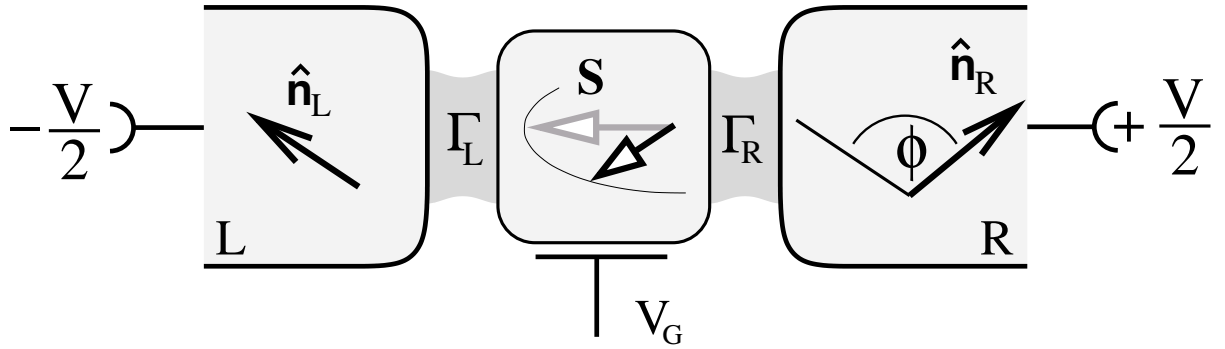


Figure 2.1: Sketch of a quantum-dot spin valve.

In the literature the problem of contacting an interacting nanostructure to ferromagnetic leads is discussed in a variety of different limits. Mostly it is assumed, that the magnetizations of the leads contacting the quantum dot [26–29], or the metallic island [30–34] are aligned collinear. The assumption of collinearity considerably simplifies the theoretical analysis, and the mostly used approach to guess the transition rates between lead and dot is successful. However, in these collinear structures, the majority and minority spin states, which are injected from the leads into the dot are energy eigenstates of the dot system. Therefore, in contrast to the non-collinear setup, there is no coherent evolution of

the spin state, i.e., spin precession, observable. If one wants to examine the influence of a coherent spin evolution on transport, one has to break the rotational symmetry of the system around the lead magnetizations by either non-collinear lead magnetizations or by a transversal applied magnetic field. However, as we will see in the following Chapters, the breaking of the rotational symmetry lead to a much more complicated situation, which can no longer be handled correctly with the approach to guess the rates, but a rigid calculation will be necessary.

Another already discussed limit is to allow arbitrary angles between the lead magnetizations, but to treat the charge interaction on the central island perturbatively [35]. Since in quantum dots the charge interaction is the dominant energy scale, we are interested in treating the charge interaction exact. The price to pay is in this case, that tunneling must be treated as perturbation.

## 2.1 Model Hamiltonian

The structure of a Hamiltonian describing tunneling is  $H = H_0 + H_T$ . The part  $H_0$  describes the decoupled systems and  $H_T$  the tunneling between these. In the case of the quantum-dot spin valve [36], the decoupled systems include the two ferromagnetic leads,  $H_L$  and  $H_R$ , and the quantum dot  $H_{\text{dot}}$ , that

$$H = H_{\text{dot}} + H_L + H_R + H_T. \quad (2.1)$$

Since we consider a quantum dot with a level spacing exceeding thermal broadening, intrinsic linewidth, applied bias voltage and charging energy, only a single electronic level contributes to transport. In this limit, the quantum dot can be treated as an Anderson impurity [37]:

$$H_{\text{dot}} = \sum_{n=\uparrow\downarrow} \varepsilon_n d_n^\dagger d_n + U d_\uparrow^\dagger d_\uparrow d_\downarrow^\dagger d_\downarrow. \quad (2.2)$$

The Fermion creation and annihilation operators of the dot electrons with spin  $n = \uparrow, \downarrow$  are labeled  $d_n^\dagger$  and  $d_n$ . This Hamiltonian describes an atomic like energy level at an energy  $\varepsilon$ , measured relative to the equilibrium Fermi energy of the leads. Double occupation of the level costs the additional charging energy  $U$ . If an external magnetic field  $\mathbf{B}_{\text{ext}}$  is applied, the spin quantization axis of the quantum dot is chosen to be parallel to this field. Then, the effect of the magnetic field is the spin-dependent splitting of the energy level by the Zeeman energy  $\Delta = g\mu_B|\mathbf{B}_{\text{ext}}|$ .

The two ferromagnetic leads are treated as large reservoirs of itinerant electrons

$$H_r = \sum_{rk\alpha} \varepsilon_{rk\alpha} c_{rk\alpha}^\dagger c_{rk\alpha} \quad (r = L/R). \quad (2.3)$$

The Fermion operators of the lead  $r$  are labeled by  $c_{rk\alpha}^{(\dagger)}$ , where  $k$  labels the momentum and  $\alpha = \pm$  the spin. The spin quantization axis for the electrons in reservoir  $r$  is chosen along its magnetization direction  $\hat{\mathbf{n}}_r$ . In the spirit of the Stoner model of ferromagnetism, we assume a strong spin asymmetry in the density of states  $\xi_{r,\pm}(\omega)$  for majority (+) and minority (−) spins. Without loss of generality we define the spin type as 'majority' which has the larger DOS at the Fermi energy. Furthermore we assume the direction of magnetization to be parallel to the direction of majority spins. In the following, the densities of states are approximated to be energy independent  $\rho_{r,\pm}(\omega) = \rho_{r,\pm}$ . Real ferromagnets have a structured density of states. This will modify details of our results but not change the general physical picture. The asymmetry in the density of states is characterized by the degree of spin polarization  $p_r = (\xi_{r+} - \xi_{r-})/(\xi_{r+} + \xi_{r-})$  with  $0 \leq p_r \leq 1$ . The polarization  $p_r = 0$  corresponds to a non-magnetic lead, and  $p_r = 1$  describes a half-metallic lead, carrying majority spins only. The magnetization directions of the leads can differ from each other, enclosing an angle  $\phi = \angle(\hat{\mathbf{n}}_L, \hat{\mathbf{n}}_R)$ . Furthermore, the leads shall be so large, that the electrons can always be described as in equilibrium by the Fermi distribution function  $f_r(\omega)$ . An applied bias voltage is taken into account by a symmetric shift of the chemical potential in the left and right lead by  $\pm eV/2$ . In Fig. 2.2, the energetic structure of the quantum dot is sketched.

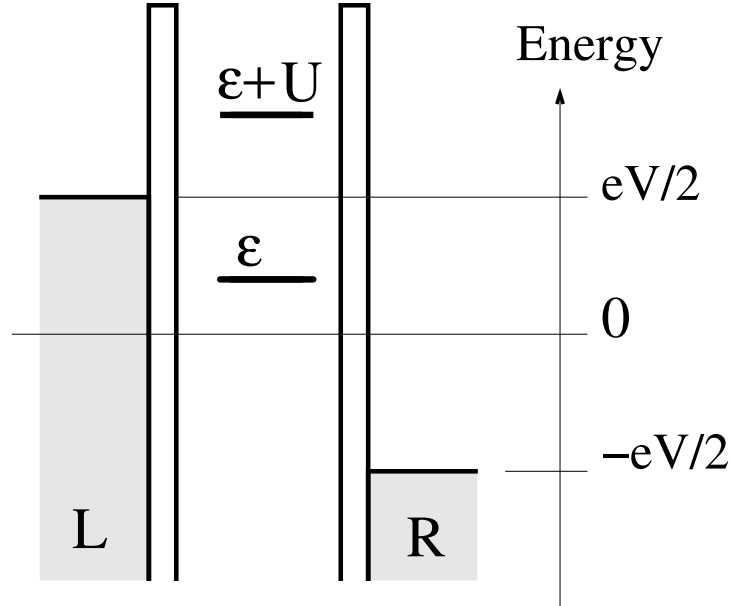


Figure 2.2: Energy scheme of the quantum dot. The central region, containing the atomic-like energy level is separated from the leads by tunnel barriers. The difference of the electrochemical potentials of the left and right lead describes a symmetrically applied bias voltage.

The tunnel Hamiltonian in Eq. (2.1) connects each lead to the quantum dot by

$$H_T = \sum_{rk\alpha n} \left( V_{rk\alpha n} c_{rk\alpha}^\dagger d_n + h.c. \right). \quad (2.4)$$

As we have chosen different spin-quantization axes for the lead subsystems (parallel to the respective magnetizations) and for the dot subsystem (parallel to an external magnetic field), the tunnel matrix elements  $V_{rk\alpha n}$  are not diagonal in spin space. However, we require that tunneling is spin conserving. The tunnel amplitudes can then be separated in  $V_{rk\alpha n} = t_{rk} \times U_{\alpha n}^r$ , i.e., a spin independent tunnel amplitude  $t_{rk}$  and a  $SU(2)$  rotation matrix  $U_{\alpha n}^r$ . The explicit shape of the matrix is determined by the geometric configuration of the lead magnetization directions and the magnetic field direction.

## 2.2 Definition of the tunnel coupling strength

The strength of the tunnel coupling is quantitatively described by  $\Gamma_{r\alpha}(\omega) = 2\pi \sum_k |t_{rk}|^2 \delta(\omega - \varepsilon_{rk\alpha})$ , which resembles Fermi's golden rule. For simplicity, we assume the density of states  $\xi_{r\alpha} = \sum_k \delta(\omega - \varepsilon_{rk\alpha})$  and the tunneling amplitudes  $t_r$  to be independent of energy, which implies constant tunnel couplings  $\Gamma_{r\alpha}$ . If the tunnel barriers themselves are not spin dependent, the couplings are also related to the leads' spin polarization by  $p_r = (\Gamma_{r+} - \Gamma_{r-}) / (\Gamma_{r+} + \Gamma_{r-})$ . Often, it is less convenient, to use the spin dependent tunnel couplings  $\Gamma_{r\alpha}$ , but instead to parameterize these by the polarization  $p_r$  and the average tunnel coupling to the lead  $\Gamma_r = \sum_{\sigma=\pm} \Gamma_{r,\sigma} / 2$ . The total lead-dot coupling is then described by the parameter  $\Gamma = \Gamma_L + \Gamma_R$ .

We will restrict ourself to the limit of weak dot-lead coupling, so that tunneling events are rather rare. Then between successive tunnel events all quantum mechanical correlations in the leads, which were generated by the tunneling of an electron, are already decayed. In this limit each tunnel event can then be treated as separate. While the average time between tunneling is given by the inverse tunnel rate, the equilibration time of the leads is given by the inverse temperature. Therefore, one parameter regime constraint is  $\Gamma_{r\alpha} \ll k_B T$ . Further we have to exclude second order transport (cotunneling) which becomes important in the Coulomb blockade regions [38] or the Kondo regime, see e.g. Ref. [39]. Technically, we present a theory, which takes into account the charge interaction and the spin dynamics on the dot exactly, but treats the tunnel rates and all other subsequently derived quantities like conductance and noise only up to first order in the parameter  $\Gamma / k_B T$ .

This approach of calculating all rates up to first order in  $\Gamma$  is often called sequential tunneling. Since in this regime, the tunnel events are often intuitively accessible, several publications try simply to guess all possible tunnel events. While this *ad hoc* approach gives the correct result for the simplest quantum-dot systems, it fails if the quantum-dot system bears another degree of freedom besides charge. In such more complicated systems, the lowest order transport is already influenced by tunnel induced energy level renormalization effects [40], which can not be guessed easily.



The energy level renormalization is of the order of the tunnel coupling strength. Therefore transport is usually only affected by this renormalization in the second or higher order contributions in  $\Gamma$ . However, the energy renormalization builds up a relative quantum mechanical phase of the electrons proportional to the renormalization energy (proportional  $\Gamma$ ) times the time, the electron stays inside the dot, which is given by  $1/\Gamma$ . The renormalization generated phase, which the electrons accumulate during their stay on the quantum dot, is therefore independent of  $\Gamma$ . If the additional degree of freedom of the quantum-dot system reflects this accumulated phase, then, already the first order tunnel current can be affected by the renormalization.

In the here discussed quantum-dot spin valve system, the additional degree of freedom of the dot is its non-equilibrium spin. The spin dependent level renormalization generates a relative phase between spin up and down, yielding a rotation of the spin. The spin precesses on the dot as long as it stays on the dot. Therefore the angle of precession is now the product of time and precession angular velocity, i.e., independent of  $\Gamma$ . Since in the quantum-dot spin valve this relative angle between dot spin and the contact magnetization direction generate magnetoresistance, the energy level renormalization affects the lowest order transport.

## 2.3 Reduced density matrix of the quantum dot

Since the leads are modeled by non-interacting fermions, which are assumed to stay always in equilibrium, their degrees of freedom can be integrated out. To describe the quantum-dot spin valve one does only need to consider the reduced density matrix  $\rho_{\text{dot}}(t)$  of the quantum dot. This density matrix contains the information about both, the charge and the spin state of the dot. Since the quantum dot consists of a single electronic level, the basis of the Hilbert space is given by the states  $\chi = 0$  (empty dot),  $\uparrow$  (dot occupied with one spin-up electron),  $\downarrow$  (dot occupied with a spin-down electron), and  $d$  (double occupancy of the dot). The reduced density matrix  $\rho_{\text{dot}}$  is a  $4 \times 4$  matrix with the elements  $P_{\chi'}^{\chi} \equiv (\rho_{\text{dot}})_{\chi\chi'}$ . In matrix notation, we get

$$\rho_{\text{dot}} = \begin{pmatrix} P_0 & 0 & 0 & 0 \\ 0 & P_{\uparrow} & P_{\downarrow}^{\uparrow} & 0 \\ 0 & P_{\uparrow}^{\downarrow} & P_{\downarrow} & 0 \\ 0 & 0 & 0 & P_d \end{pmatrix}. \quad (2.5)$$

The diagonal, real entries  $P_{\chi} \equiv P_{\chi}^{\chi}$  are the probabilities to find the dot in the state empty ( $\chi = 0$ ), occupied with one spin up ( $\chi = \uparrow$ ) or one down ( $\chi = \downarrow$ ) electron, or double occupied ( $d$ ) with a spin singlet. The zeros in Eq. (2.5) in the off diagonals are a consequence of the total particle number conservation. The inner  $2 \times 2$  matrix is the  $SU(2)$  representation of the dot spin.

The reduced dot density matrix contains five independent parameters, since the trace of the density matrix is normalized:  $P_0 + P_{\uparrow} + P_{\downarrow} + P_d = 1$ . It is often more intuitive

and convenient, to describe the quantum-dot state by the probabilities for the three charge states  $P_0$ ,  $P_1 = P_\uparrow + P_\downarrow$ , and  $P_d$  and the average spin vector  $\mathbf{S} = (P_\downarrow^\uparrow + P_\uparrow^\downarrow, iP_\downarrow^\uparrow - iP_\uparrow^\downarrow, P_\uparrow - P_\downarrow)/2$ . The magnitude of the average spin  $\mathbf{S}$  lies between zero, for an unpolarized dot, and  $\hbar/2$ , if the quantum-dot electron is in a pure spin state.

## 2.4 Experimental realizations of a quantum-dot spin valve

The experimental realization of a quantum-dot spin valve is quite challenging, since one must combine ferromagnetic, i.e., typically metallic leads with quantum dots, which are usually semiconductor structures. One way to overcome this material mismatch is to use spin injection from a ferromagnetic semiconductor into quantum dots as observed by Chye *et al.* [41].

Recent experimental approaches to measure transport through such a quantum-dot spin valve involve purely metallic systems, which are patterned by state of the art photolithographical techniques, as done by Ono *et al.* [42], or by Zaffalon *et al.* [43], see Fig. 2.3. The advantage of this approach is, that the structures can be reproducibly generated with well defined dimensions and properties, like tunnel couplings. While in these structures spin accumulation was extensively studied, the size of the structures are too large to show size quantization effects. Therefore the islands can not be described by the Anderson model we use.

By embedding metallic grains in a tunnel junction between two ferromagnetic layers, the structure dimension becomes much smaller than what can be achieved by photolithography. To form these islands, Zhang *et al.* [44] used Al grains, while Schelp *et al.* [45] and Yakushiji *et al.* [46, 47] used Co clusters embedded in an insulating Aluminum oxide tunnel barrier. The main disadvantage of these granular structures is that usually transport through an ensemble of dots is measured, which can cause an average-out of certain features.

Deshmukh *et al.* [48] succeeded in contacting a single grain. They created a nanopinhole in an isolating  $\text{Si}_3\text{N}_4$  layer, deposited an Al-lead on one side, and Al grains, isolated by an oxide layer, together with a ferromagnetic lead on the other side. Thereby only one Al grain was contacted by both leads through the pinhole. This device showed clear charge as well as size quantization effects. The only difference to the here discussed quantum-dot spin valve is, that only one lead was ferromagnetic. In that specific experiment, the other lead was chosen to become superconducting, however, a device with both leads being ferromagnetic is in work.

A different approach to form quantum dots is to contact individual molecules. A molecular device is the smallest possible structure. Due to their superior smallness, such devices can show charge and size quantization even at room temperature. A very stable realization of a molecular quantum-dot spin valve can be realized by carbon nanotubes

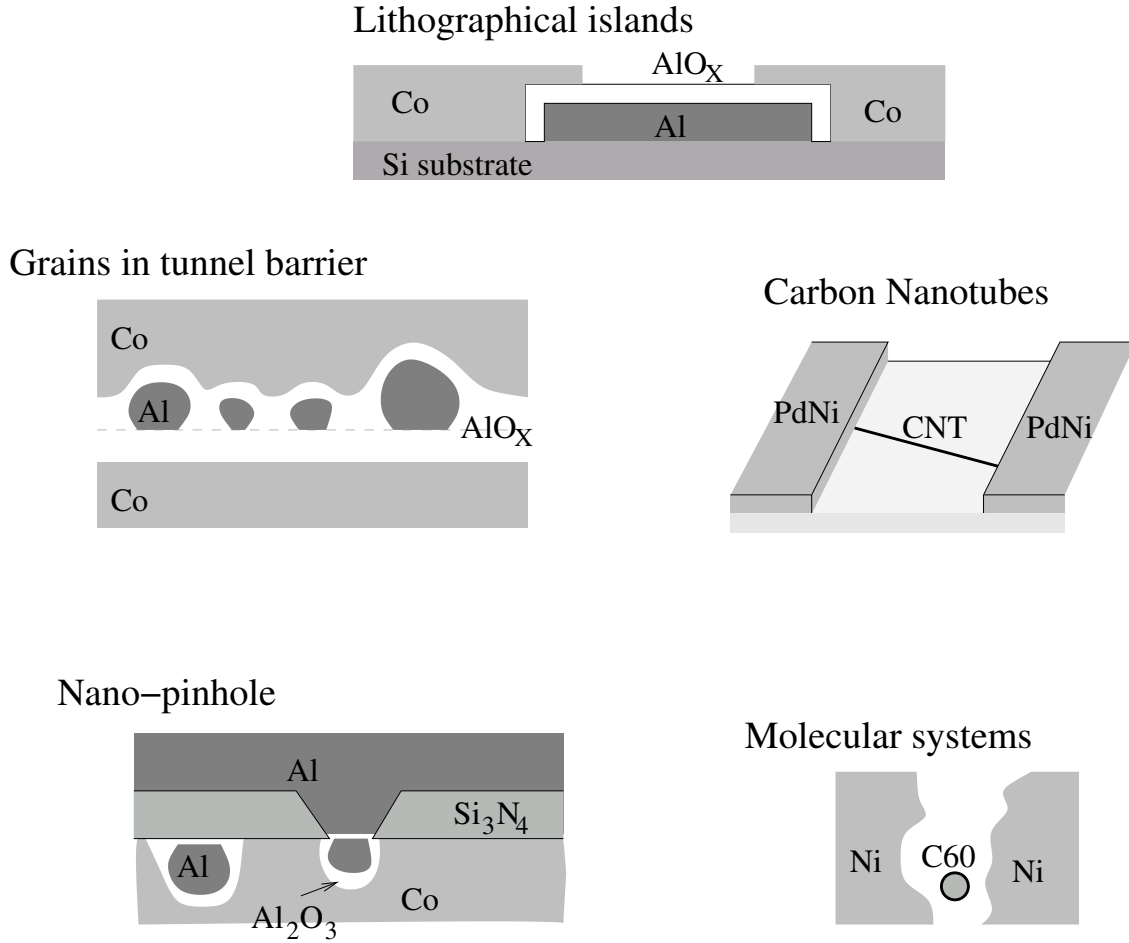


Figure 2.3: Different possible realizations of a single electron transistor with ferromagnetic leads.

[49, 50]. Due to their length, one can cover each end of a tube by a separate ferromagnetic lead like Fe [51] or Co [52, 53], and measure transport through the molecule. However, the barriers are usually rather thin, that the transport through the device can not always be described by lowest order transport, which will be the focus of this work. Recently Sahoo *et al.* [54] observed tunnel magnetoresistance in transport through a nanotube. They used a PdNi alloy for the contacts. This material has proven to form very good tunnel barriers to the nanotubes. Moreover, they observe an oscillation of the tunnel magnetoresistance as function of the gate voltage. This effect may be a result of the further discussed many-body exchange effect, or due to a single particle mixing conductance mechanism as proposed by Cottet *et al.* [55].

Another molecular spin-valve device was manufactured by Pasupathy *et al.* [56]. They

formed a nano-trench in a Ni layer by electromigration, and then trapped a  $C_{60}$  molecule in between. Thereby they observed the Kondo effect, where the Kondo peak was split. This splitting as predicted by Martinek *et al.* [39] due to the many-body exchange coupling to the ferromagnetic leads. The following work will discuss the same effect but not in the strong coupling / Kondo regime, but in the weak coupling regime, which can be described by sequential tunneling.

The rapid technological advantages of spin polarized scanning tunneling microscopy (STM) [57] offers another possible realization of a quantum-dot spin valve. One could contact a surface impurity on a ferromagnetic substrate by the ferromagnetic STM tip. Then the surface impurity would serve as quantum dot, and tip and substrate as leads. The contacting of a surface impurity (by paramagnetic leads) was already demonstrated by Manassen *et al.* [58] and Durkan *et al.* [59], which triggered a series of theoretical works [60–64], related to this dissertation.

## Chapter 3

# Dynamics of the Quantum-Dot Charge and Spin

Since the quantum dot consists only of a single atomic level, its charge state is completely characterized by the probability to measure none, one or two electrons on the structure. In equilibrium (in the weak coupling regime) these probabilities would be given by Boltzmann factors. By applying a finite source-drain voltage to the quantum-dot system, the charge occupation probabilities will not longer follow the equilibrium distribution, i.e, they are ‘a priori’ unknown. However, the static dot charge state can be determined via the conservation law of charge. The electrical currents through the interfaces change the charge on the dot. Therefore, the static dot state is characterized by the condition, that the sum of all incoming time-averaged electrical currents vanish. On the other side, the current through each interface can be calculated as function of the (unknown) charge occupation probabilities. Therefore, one can construct a system of linear equations, which determine the time-averaged charge state of the dot, out of the continuity equations. The so called orthodox theory to construct a master equation from the tunnel rates through the interfaces is conceptionally equivalent [1,2].

Since we assume the quantum dot to be non-magnetic, the average spin on the quantum dot does vanish in equilibrium. However, if the contact leads are ferromagnetic, as in the case of a quantum-dot spin valve, the dot can not only bear a non-equilibrium charge, but also a non-equilibrium spin state. The tunnel coupling between the quantum dot level and spin-polarized leads yields a transfer of angular momentum across each tunnel junction. The stationary value of the dot spin can again be determined by balancing all incoming currents of angular momentum. In contrast to the case of charge, there are also other sources of angular momentum possible beside the (spin) currents through the interface: an externally applied magnetic field can act as additional source and intrinsic spin relaxation on the dot as additional sink of angular momentum.

Instead of constructing the system of master equations out of the continuity equations, as done in this Chapter, one can also directly calculate the quantum mechanical transition

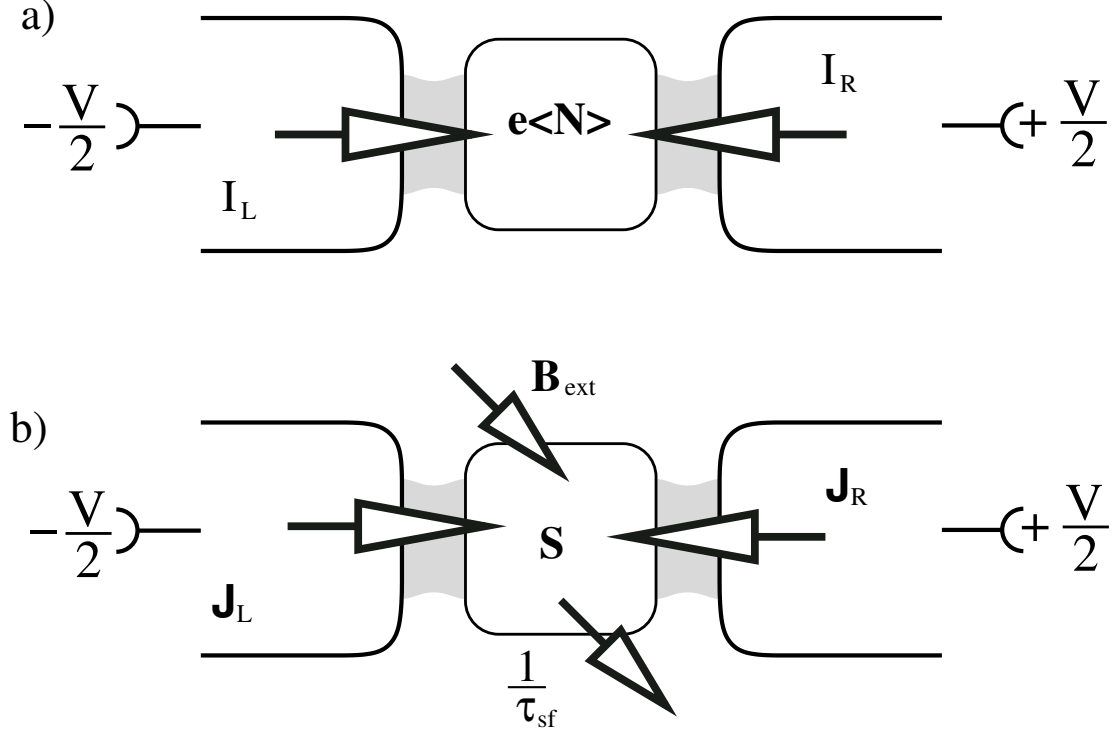


Figure 3.1: a) The dot charge changes due to the electrical current through the tunnel barriers. b) The dot-spin continuity equation contains also other sources and sinks of angular momentum: an external magnetic field  $\mathbf{B}_{\text{ext}}$  and intrinsic spin-flip relaxation on the dot on the time scale  $\tau_{\text{sf}}$ .

rates between the individual quantum dot charge and spin states [1,2]. In our first publication [Phys. Rev. **B**, 195345 (2004)], we followed this rate equation approach. Thereby we rigidly calculated the required transition rates with a diagrammatic technique [65], which was especially designed to describe transport through quantum dots. In Chapter 5, we will use this diagrammatic technique to discuss the current noise through the quantum-dot spin valve.

### 3.1 Balancing charge currents

The current through each tunnel barrier  $r = \text{L}, \text{R}$  equals the change of the charge  $e\hat{N}_r = e \sum_{k\sigma} a_{rk\sigma}^\dagger a_{rk\sigma}$  in the respective lead  $r$ . From the Heisenberg time evolution of the density

operator, we get

$$\begin{aligned}\hat{I}_r &= -e \frac{\partial \hat{N}_r}{\partial t} = -\frac{e}{i\hbar} [\hat{N}_r, H_T] \\ &= -\frac{e}{i\hbar} \sum_{k\alpha\beta n} V_{rk\alpha n} c_{rk\alpha}^\dagger d_n - V_{rk\alpha n}^* d_n^\dagger c_{rk\alpha}.\end{aligned}\quad (3.1)$$

With the definition of the Keldysh Green's functions  $G_{n,rk\alpha}^<(t) = i\langle c_{rk\alpha}^\dagger(0) d_n(t) \rangle$ , the time-averaged current through tunnel contact  $r$  equals

$$I_r = -\frac{e}{h} \sum_{k\alpha n} \int d\omega \left( V_{rk\alpha n} G_{n,rk\alpha}^<(\omega) - V_{rk\alpha n}^* G_{rk\alpha,n}^<(\omega) \right). \quad (3.2)$$

In Ref. [66] Meir and Wingreen used a Dyson equation, to relate the Green's functions, containing one dot and one lead operator each, to the full lead electron Green's function and the full dot Green's function. Since the leads are assumed to stay always in equilibrium, we can use their equilibrium Green's functions:  $g_{rk\alpha}^< = 2\pi i f_r^+(\omega) \delta(\omega - \varepsilon_{rk\alpha})$ ,  $g_{rk\alpha}^> = -2\pi i f_r^-(\omega) \delta(\omega - \varepsilon_{rk\alpha})$ ,  $g_{rk\alpha}^{\text{ret}} = 1/(\omega - \varepsilon_{rk\alpha} + i0^+)$ , and  $g_{rk\alpha}^{\text{adv}} = (g_{rk\alpha}^{\text{ret}})^*$  [67]. Thereby  $f_r^+$  labels the Fermi distribution function of the lead  $r$  and  $f_r^- = 1 - f_r^+$ .

Only the dot Green's functions must be derived. One possibility to determine the dot Green's functions is explained in Appendix A. It is worth to mention, that to calculate the current in the sequential tunneling limit, only the Green's functions, which are of zeroth order in tunneling, are needed. Thereby, the zeroth order Green's functions are not the equilibrium Green's functions, but are itself functions of the unknown density matrix elements  $P_\eta^x$  of the quantum dot. The expression for the current through a tunnel interface in first order in  $\Gamma$  follows as

$$\begin{aligned}I_r &= \Gamma_r \frac{2(-e)}{\hbar} \left[ f_r^+(\varepsilon) P_0 + \frac{f_r^+(\varepsilon + U) - f_r^-(\varepsilon)}{2} P_1 - f_r^-(\varepsilon + U) P_d \right. \\ &\quad \left. - p_r [f_r^-(\varepsilon) + f_r^+(\varepsilon + U)] \mathbf{S} \cdot \hat{\mathbf{n}}_r \right],\end{aligned}\quad (3.3)$$

with the definition of the tunnel coupling as  $\Gamma_r \equiv (\Gamma_{r\uparrow} + \Gamma_{r\downarrow})/2$ .

The time-averaged dot spin  $\mathbf{S}$  influences the conductance via the scalar product  $(\mathbf{S} \cdot \hat{\mathbf{n}}_r)$ . Therefore the tunnel magnetoresistance generated by each tunnel junction depends cosine like on the relative angle enclosed by lead magnetization and spin polarization. This tunnel magnetoresistance resembles the behavior of a tunnel junction between two ferromagnetic contacts [12, 18–20]. However, in contrast to the single tunnel junction, considered by Jullière and Slonczewski, where the directions of magnetizations are external parameters, in the quantum-dot spin valve the direction of the dot spin polarization is a dynamic variable, controllable by gate and bias voltage as well as by an external magnetic field.

The continuity equation connects the static average dot charge  $e\langle\hat{N}\rangle = e\sum_n nP_n$  to the currents through the interfaces:

$$0 = e\frac{d\langle\hat{N}\rangle}{dt} = I_L + I_R. \quad (3.4)$$

Moreover, the stationary condition does not only require, that the total charge is constant, but that each of the occupation probabilities  $P_i$  do not vary in time. In lowest order transport, which we consider here, we can split the charge continuity Eq. (3.4) into two independent equations associated with transport processes in which either a double occupied or an empty dot is involved. The affiliation to either contribution is indicated by the arguments of the Fermi functions, where the presence of the interaction energy  $U$  indicates processes with double occupation and the absence signals processes involving an empty dot. The stationary conditions for the two charge states separately are then

$$0 = \frac{dP_0}{dt} = \sum_r \Gamma_r \left( f_r^+(\varepsilon)P_0 - f_r^-(\varepsilon)P_1/2 - p_r f_r^-(\varepsilon)\mathbf{S} \cdot \hat{\mathbf{n}}_r \right) \quad (3.5)$$

$$0 = \frac{dP_d}{dt} = \sum_r \Gamma_r \left( f_r^+(\varepsilon + U)P_1/2 - f_r^-(\varepsilon + U)P_d - p_r f_r^+(\varepsilon + U)\mathbf{S} \cdot \hat{\mathbf{n}}_r \right), \quad (3.6)$$

and  $dP_1/dt = -dP_0/dt - dP_d/dt$ , which follows directly from the probability normalization condition  $P_0 + P_1 + P_d = 1$ . In this way, the charge continuity equation defines three master equations for the three charge degrees of freedom. However, these equations still depend on the time-averaged spin of the quantum dot.

## 3.2 Balancing spin currents

The static spin on the quantum dot is given by the condition, that the sum of all sources of angular momentum vanish. For a careful treatment of the total transfer of angular momentum through the tunnel barriers, first a rigid calculation of these spin currents in terms of non-equilibrium Keldysh Green's functions is presented. The outcome of the rigid calculation will show, that the spin current has two conceptional different components, associated with either particle transfer or exchange interaction. Afterwards, we specify our result to the weak coupling regime of a quantum-dot spin valve and derive in this limit Bloch-like rate equations for the quantum-dot spin.

### 3.2.1 Spin current through one tunnel barrier

The calculation of the spin current in this Section will be in close analogy to the derivation of the charge current by Meir and Wingreen [66]. Let us first consider the spin current through one, say the left, tunnel barrier. For a clearer notation, the lead index is mostly



dropped in this Section. The spin current  $\mathbf{J}_L = \langle \hat{\mathbf{J}}_L \rangle$  from the left lead into the dot is defined by minus the time derivative of the total lead spin  $\hat{\mathbf{S}}_L = (\hbar/2) \sum_{k\alpha\beta} c_{k\alpha}^\dagger \boldsymbol{\sigma}_{\alpha\beta} c_{k\beta}$ , where  $\boldsymbol{\sigma}_{\alpha\beta}$  denotes the vector of Pauli matrices. From the Heisenberg equation follows

$$\hat{\mathbf{J}}_L = -\frac{d}{dt} \hat{\mathbf{S}}_L = -\frac{1}{i\hbar} [\hat{\mathbf{S}}_L, H]. \quad (3.7)$$

With the use of Fermion commutation relations, the spin current operator is found to be

$$\hat{\mathbf{J}}_L = -\frac{1}{2i} \sum_{k\alpha\beta n} \left( V_{k\alpha n} \boldsymbol{\sigma}_{\alpha\beta}^* c_{k\beta}^\dagger d_n - V_{k\alpha n}^* \boldsymbol{\sigma}_{\alpha\beta} d_n^\dagger c_{k\beta} \right). \quad (3.8)$$

By introducing the Keldysh Green's functions  $G_{n,k\beta}^<(t) = i\langle c_{k\beta}^\dagger(0) d_n(t) \rangle$ , the expectation value of the spin current can be written as

$$\mathbf{J}_L = \frac{1}{2} \sum_{k\alpha\beta n} \int \frac{d\omega}{2\pi} \left( V_{k\alpha n} \boldsymbol{\sigma}_{\alpha\beta}^* G_{n,k\beta}^<(\omega) - V_{k\alpha n}^* \boldsymbol{\sigma}_{\alpha\beta} G_{k\beta,n}^<(\omega) \right). \quad (3.9)$$

Since the Green's functions obey the Dyson equations  $G_{k\alpha,n}^< = \sum_m V_{k\alpha,m} [g_{k\alpha}^t G_{m,n}^< - g_{k\alpha}^< G_{m,n}^t]$  and  $G_{n,k\alpha}^< = \sum_m V_{k\alpha,m}^* [g_{k\alpha}^< G_{n,m}^t - g_{k\alpha}^t G_{n,m}^<]$ , the Green's functions in Eq. (3.9) can be replaced with the dot Green's functions  $G_{n,m}^<(t) = i\langle d_m^\dagger d_n(t) \rangle$  and the free Green's functions of the lead, see Section 3.1, or Ref. [67].

Without loss of generality, we can choose the dot spin quantization axis parallel to the lead magnetization direction  $\hat{\mathbf{n}}_L$ . The tunnel matrix elements can then be substituted by  $V_{k\alpha,n} = t_k \delta_{\alpha n}$ . After a lengthy but straightforward calculation, the spin current can be written as

$$\begin{aligned} \mathbf{J}_L = & \frac{i}{4} \sum_{m,n} \int \frac{d\omega}{2\pi} \boldsymbol{\sigma}_{mn} (\Gamma_m + \Gamma_n) [f_L^+(\omega) G_{n,m}^> + f_L^-(\omega) G_{n,m}^<] \\ & + \boldsymbol{\sigma}_{mn} (\Gamma_m - \Gamma_n) \left[ f_L^+(\omega) (G_{n,m}^{\text{ret}} + G_{n,m}^{\text{adv}}) + \frac{1}{i\pi} \int' dE \frac{G_{n,m}^<(E)}{E - \omega} \right], \end{aligned} \quad (3.10)$$

with the tunnel rates  $\Gamma_n(\omega) = 2\pi \sum_k |t_{Lk}|^2 \delta(\omega - \varepsilon_{Lk\alpha}) \delta_{\alpha n}$ . This is the most general expression for the spin current flowing through a tunnel barrier. Since the Green's functions  $G_{n,m}$  were not specified during the calculation, Eq. (3.10) holds for any electronic system, not only for single-level quantum dots.

If the dot state is rotationally symmetric about the lead magnetization direction  $\hat{\mathbf{n}}_L$ , all dot Green's functions  $G_{\sigma\sigma'}$  non-diagonal in spin space vanish. Only in this special case, the spin current is proportional to the difference between the charge current  $I_L^\uparrow = i(e/h) \int d\omega \Gamma_\uparrow [f_L^+(\omega) G_{\uparrow\uparrow}^> + f_L^-(\omega) G_{\uparrow\uparrow}^<]$  carried by spin-up electrons and the charge current  $I_L^\downarrow$  carried by spin-down electrons,

$$\mathbf{J}_L = J_L^z \hat{\mathbf{e}}_z = \frac{\hbar}{2e} (I_L^\uparrow - I_L^\downarrow) \hat{\mathbf{e}}_z. \quad (3.11)$$

If the dot system breaks this rotational symmetry, for example due to spin accumulation along an axis different from  $\hat{\mathbf{n}}_L$ , the simple result of Eq. (3.11) is no longer correct. In such a situation, the second line in Eq. (3.10) yields an additional spin current component, oriented transversal to both, the magnetization of the lead and the polarization of the dot. This spin-current component describes the exchange coupling between lead and dot spin, causing both to precess around each other. Since the lead magnetization is usually pinned, only the dot spin precesses as placed in a magnetic field.

Brataas *et al.* [68, 69] showed, that at normal metal–ferromagnet interfaces, incoming electrons, with a spin orientation non-collinear to the lead magnetization direction, may experience a rotation of the spin direction during backscattering. This spin-rotation mechanism can be described by the so called spin-mixing conductance. However, the origin of this spin precession has a different physical origin as the interaction driven many-body effect discussed in this dissertation.

### 3.2.2 Spin current between lead and quantum dot

The general expressions for the spin current will now be specified to the case of a quantum-dot spin valve with weak tunnel coupling. By use of the zeroth order Keldysh Green's functions of the dot system, as calculated in Appendix A, Eq. (3.10) can be specified to the system of a ferromagnet–single-level quantum-dot interface. The gained expression relates the spin current through the interface to the dot density matrix elements

$$\mathbf{J}_r = \frac{\hbar}{2e} I_r p_r \hat{\mathbf{n}}_r - \frac{\mathbf{S} - p_r^2 (\hat{\mathbf{n}}_r \cdot \mathbf{S}) \hat{\mathbf{n}}_r}{\tau_{c,r}} + \mathbf{S} \times \mathbf{B}_r, \quad (3.12)$$

where  $I_r$  is the electrical current crossing the tunnel junction as defined in Eq. (3.3). The different terms of the spin current can be associated with different physical processes.

- The first term in Eq. (3.12) describes spin injection from the ferromagnetic lead into the quantum dot by a spin polarized charge current. The injected spin is proportional to the lead polarization  $p_r$  and the electrical current  $I_r$  crossing the junction. Since for vanishing bias voltage the charge current vanishes, also this spin current contribution vanishes.
- The second term describes relaxation of the dot spin due to coupling to the leads. Since neither an empty nor a doubly occupied dot can bear a net spin, the spin relaxation time  $\tau_{c,r}^{-1} = \Gamma_r / \hbar (1 - f_r(\varepsilon) + f_r(\varepsilon + U))$  equals the life time of the single occupation dot state. This relaxation term is anisotropic [70]. The spin polarization of the lead suppresses the relaxation of a dot spin, which is aligned parallel to the lead magnetization, but increases the relaxation of the antiparallel component.
- The third term in Eq. (3.12) describes transfer of angular momentum perpendicular to the spin polarization directions of lead and dot. The structure of this term

suggests the interpretation of  $\mathbf{B}_r$  as being an effective magnetic field that acts on the quantum-dot spin  $\mathbf{S}$ . Its value is given by [36, 71]

$$\mathbf{B}_r = p_r \frac{\Gamma_r \hat{\mathbf{n}}_r}{\pi \hbar} \int' d\omega \left( \frac{f_r^+(\omega)}{\omega - \varepsilon - U} + \frac{f_r^-(\omega)}{\omega - \varepsilon} \right), \quad (3.13)$$

where the prime at the integral indicates Cauchy's principal value.

From Eq. (3.13) it is clear that this exchange field arises due to the fact that the quantum-dot levels are tunnel coupled to a spin polarized lead. It persists also for vanishing bias voltage. It is a many body effect as all degrees of freedom in the leads contribute to the integral. In the limit of energy independent tunnel couplings, the finite Coulomb interaction  $U$  in the dot prevents cancellation of the first and second term in the integrand in Eq. (3.13), i.e., the exchange field is interaction driven. Its nature can be conceived as a spin dependent dot level renormalization due to virtual particle exchange with the spin polarized leads. Note that these virtual exchange processes do not change the charge of the dot, in contrast to the spin dependent tunneling events responsible for the first two contributions of Eq. (3.12). Therefore a simple rate equation picture can not address this exchange interaction. However, since this exchange field contribution is also linear in  $\Gamma$ , it is needed to be kept in order to have a consistent expansion of the master equation in lowest order in the tunnel coupling.

This type of exchange interaction has been discussed in literature in the context of Kondo physics for magnetic impurities in (normal) metals [72]. With the help of a Schrieffer-Wolff transformation, the Anderson Hamiltonian [37] describing the magnetic impurity can be transformed to the  $s-d$  model, in which the spin of the magnetic impurity is coupled to the conduction band electron spins of the metal. While a normal metal is spin symmetric, and therefore no net exchange field arise, the ferromagnetic leads of the quantum-dot spin valve include a finite spin polarization. By integrating out the lead electrons of the transformed Hamiltonian in the subspace of single dot occupancy, the precise mathematical form of the exchange field as given in Eq. (3.13) is recovered.

The exchange field is not only responsible for a torque on an accumulated spin as discussed here, but it also generates a spin splitting of the dot level. Such a Zeeman splitting of a Kondo resonance in a single molecule has been predicted by Martinek *et al.* [39], and was experimentally observed by Pasupathy *et al.* [56]. The reported splitting would correspond to magnetic field strength values of up to 70 Tesla. This large Zeeman splitting motivated Fransson *et al.* [73] to propose such a spin splitted level as spin filter for spintronic applications. In contrast to these experiments with strong dot-lead coupling, in the weak coupling regime, only the precession of the accumulated dot spin must be considered. The Zeeman-like splitting of the dot levels gives rise to a correction of higher order in the coupling that has to be dropped in a consistent first order transport calculation.

### 3.2.3 Angular momentum continuity equation

Similar to the charge continuity equation, the continuity equation for the dot spin reads

$$\begin{aligned}
 0 = \frac{d\mathbf{S}}{dt} &= \mathbf{J}_L + \mathbf{J}_R + \mathbf{S} \times \mathbf{B}_{\text{ext}} - \frac{\mathbf{S}}{\tau_{\text{sf}}} \\
 &= \frac{\hbar}{2e} \sum_r \left[ I_r p_r \hat{\mathbf{n}}_r - \frac{\mathbf{S} - p^2(\hat{\mathbf{n}}_r \cdot \mathbf{S})\hat{\mathbf{n}}_r}{\tau_{c,r}} \right] + \mathbf{S} \times \mathbf{B}_{\text{tot}} - \frac{\mathbf{S}}{\tau_{\text{sf}}}. \quad (3.14)
 \end{aligned}$$

In addition to the spin currents entering the quantum dot from the left and right lead, additional sources and sinks of angular momentum are possible. An external magnetic field  $\mathbf{B}_{\text{ext}}$  enters the equation in the same way as the exchange field originating from the left and right reservoir does. All three fields add up to the total field  $\mathbf{B}_{\text{tot}} = (\mathbf{B}_L + \mathbf{B}_R + \mathbf{B}_{\text{ext}})$ . Thereby frequency is used as the unit of magnetic field strength.

Furthermore, one can phenomenologically take into account the possibility of intrinsic spin relaxation on the dot by the sink term  $-\mathbf{S}/\tau$ . This term leads to an exponential decay of the spin of on the dot on the time scale  $\tau_{\text{sf}}$ . The physical origin of such an intrinsic damping could be spin-orbit coupling, hyperfine interaction with nuclei in the quantum dot, or higher order tunnel processes such as spin-flip cotunneling.

## 3.3 Chapter summary

In this Chapter, the expressions for the charge and spin currents, Eq. (3.3) and Eq. (3.12) were derived. In contrast to the charge current, the spin current is a more complex vector quantity. The total transfer of angular momentum from the leads to the dot, consists of two qualitatively different contributions. One is associated with the fact that charge currents from or to a spin polarized system are also spin polarized. This current, thus, transfers angular momentum along the magnetization direction of the ferromagnet or along the accumulated spin on the quantum dot. There is, however, also an additional transfer of angular momentum, perpendicular to both directions. The influence of this spin current on the quantum-dot spin can be expressed in terms of a many body exchange field.

With the use of the respective continuity equations, these currents determine the steady state dynamics of the dot's charge and spin by a master equation. In the next Chapter, the manipulation and detection of the quantum-dot spin is examined. Special attention is spend on the possibility to manipulate the spin either by a magnetic field, or direct by voltage, via the gate and bias voltage dependence of the exchange interaction.

## Chapter 4

# Manipulation and Detection of the Dot Spin via Electrical *dc*–Transport

The Eq. (3.5) and Eq. (3.6), together with the probability normalization condition  $P_0 + P_1 + P_d = 1$ , determine the charge occupation probabilities  $P_i$  of the quantum dot. The Bloch equation  $d\mathbf{S}/dt = 0$  in Eq. (3.14) describes the stationary dot spin  $\mathbf{S}$ . The stationary density matrix of the dot, see Eq. (2.5), can be determined by solving this system of six linear master equations. With the knowledge of the stationary density matrix, the time averaged current through the quantum-dot spin valve can then be calculated by Eq. (3.3).

Since both, charge and spin are simultaneously transported by electrons, the master equations for the charge and spin degree of freedom are coupled. In the presence of magnetized leads, the charge current causes spin accumulation on the dot, and the average spin on the dot acts back on the current via magnetoresistance. Therefore, it is possible to examine the coherent spin dynamics on the dot via electrical transport measurements. The dot-spin state is created by spin accumulation, manipulated by the source and drain voltage dependent exchange field or by an external magnetic field, and detected by the device conductance.

In the following three Sections we discuss the influence of the gate and bias voltage as well as an external magnetic field on the quantum-dot spin, and how this influence gets reflected on the electrical *dc*–transport through the quantum-dot spin valve. Then, in reversal, by experimentally measuring the transport characteristics of the device, one can conclude the spin state of the quantum dot.

In the stationary transport situation under consideration, neither the average charge nor the average spin of the dot changes with time, and the currents through the left and right tunnel junction are equal  $I_L = -I_R \equiv I$ . For simplicity, a symmetric coupling  $\Gamma_L = \Gamma_R = \Gamma/2$ , equal spin polarization  $p_L = p_R = p$ , and a symmetrically applied bias voltage  $V_R = -V_L = V/2$  is chosen in the following discussion.

## 4.1 Gate voltage effect in linear response regime

To study the effect of the gate voltage on the quantum-dot spin via the gate voltage dependence of the exchange field, we analyze the linear-response regime, without external magnetic fields applied. For a small bias voltage  $eV \ll k_B T$ , the system of master equation [Eq. (3.14), Eq. (3.5), and Eq. (3.6)] can be expanded up to linear order in bias voltage  $V$ . With symmetric couplings to the left and right lead, the charge probabilities ( $P_0, P_1, P_d$ ) become independent of  $V$ , thus, the occupation probabilities are given by their equilibrium value

$$P_0 = \frac{f^-(\varepsilon)f^-(\varepsilon+U)}{f^+(\varepsilon) + f^-(\varepsilon+U)}, \quad P_1 = 2 \frac{f^+(\varepsilon)f^-(\varepsilon+U)}{f^+(\varepsilon) + f^-(\varepsilon+U)}, \quad P_d = \frac{f^+(\varepsilon)f^+(\varepsilon+U)}{f^+(\varepsilon) + f^-(\varepsilon+U)}, \quad (4.1)$$

with the Fermi function  $f^\pm(\omega) = f_L^\pm(\omega) = f_R^\pm(\omega)$ . The Bloch equation for the dot spin does not get independent of  $V$ , but reads

$$0 = \frac{d}{dt} \mathbf{S} = p I_{\text{lin}} (\hat{\mathbf{n}}_L - \hat{\mathbf{n}}_R) - \frac{\mathbf{S} - \frac{p^2}{2} \sum_r (\hat{\mathbf{n}}_r \cdot \mathbf{S}) \hat{\mathbf{n}}_r}{\tau_c} - \frac{\mathbf{S}}{\tau_{\text{sf}}} + \mathbf{S} \times (\mathbf{B}_L + \mathbf{B}_R) \quad (4.2)$$

where  $I_{\text{lin}} = V \cdot \partial I / \partial V|_{V=0}$  is the linear current. The linear charge current, which is polarized due to the lead magnetizations generates a dot spin polarization along  $p(\hat{\mathbf{n}}_L - \hat{\mathbf{n}}_R)$ , which points along the  $y$ -axis of the coordinate system defined in Fig. 4.1.

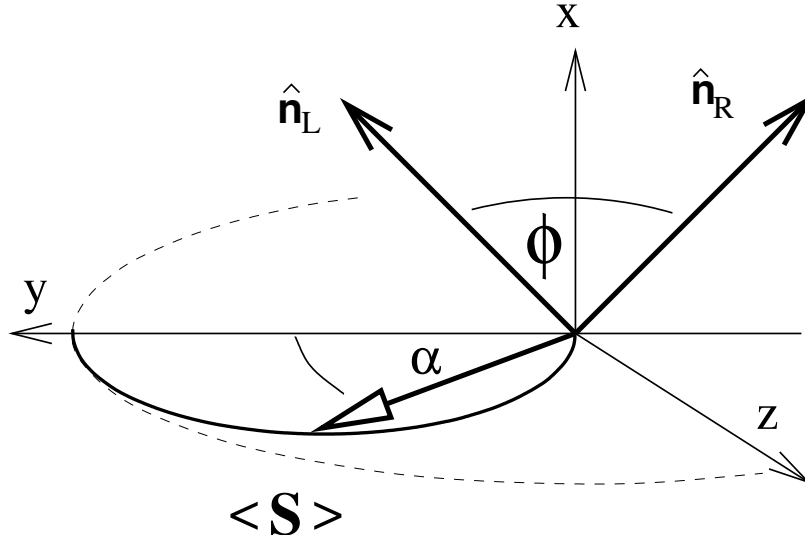


Figure 4.1: Spin dynamics in the linear-response regime. Spin accumulates along the  $y$ -direction. The spin precesses in the exchange field, that is aligned along the  $x$ -direction. The stationary solution of the average spin on the dot is tilted away from the  $y$ -axis by an angle  $\alpha$ , which is plotted in Fig. 4.2(b).

This accumulated spin  $\mathbf{S}$  generates tunnel magnetoresistance, which decreases the current again. In Fig. 4.2(a) the linear conductance is plotted as function of level position  $\varepsilon$ , that can be tuned by the gate voltage. Thereby the conductance shows Coulomb oscillations. With increasing the opening angle of the lead magnetizations, the increasing spin accumulation decreases the conductance.

The damping term(s) in Eq. (4.2) limits the magnitude of spin accumulation. The finite coherence time  $\tau_s$  of the electron spins in the quantum dot is taken into account by an exponential decay of the average spin with time. Two distinct physical processes limit the spin coherence time: Sources of decoherence, *e.g.*, spin-orbit coupling, hyperfine interaction with nuclei in the quantum dot, or higher order tunnel processes such as spin-flip cotunneling destroy the coherence of the dot spin on the time scale  $\tau_{sf}$ . Furthermore, the dwell time of the electrons itself is limited. The time scale for tunneling of an electron to or from the two electrodes is given by  $\tau_c^{-1} = \Gamma/\hbar(1 - f^+(\varepsilon) + f^+(\varepsilon + U))$ . Since neither an empty nor a double occupied dot can bear a net spin, this tunneling time scale is also the upper bound for the coherence time of the spins on the dot. Then the total spin coherence time equals

$$\frac{1}{\tau_s} = \frac{1}{\tau_c} + \frac{1}{\tau_{sf}}. \quad (4.3)$$

The term  $\mathbf{S} \times (\mathbf{B}_L + \mathbf{B}_R)$  yields an intrinsic precession of the dot spin in the exchange field  $\mathbf{B}_L + \mathbf{B}_R \equiv B_0 \cos(\phi/2) \hat{\mathbf{e}}_x$ . In steady state, the average dot spin is rotated by the angle

$$\alpha = -\arctan\left(B_0 \tau_s \cos \frac{\phi}{2}\right) \quad (4.4)$$

out of the plane defined by the lead magnetization directions, as shown in Fig. 4.1. The precession angle  $\alpha$  is plotted in Fig. 4.2(b) as function of the level position  $\varepsilon$ . The level position  $\varepsilon = -U/2$  is special, at this point the exchange field changes its sign, and so does the angle  $\alpha$ . The sign change arises from the fact, that the exchange field has contributions originating from particle like processes, and contributions with opposite sign, generated by hole like processes. Exactly at the level position  $\varepsilon = -U/2$ , these two contributions are equal, but away from this particle-hole symmetric point, either the particle or the hole processes dominate.

The precession in the exchange field also reduces the magnitude of the accumulated spin to

$$|\mathbf{S}| = p I_{\text{lin}} \tau_s \cos \alpha, \quad (4.5)$$

which can be seen in Fig. 4.1(c) as function of the level position  $\varepsilon$ .

As pointed out above, in the linear-response regime the charge occupation probabilities do not depend on the spin polarization of the leads. In particular, they are independent of the relative angle  $\phi$  of the lead magnetizations. This means that the  $\phi$ -dependence of the conductance is determined by the product  $\mathbf{S} \cdot \hat{\mathbf{n}}_L = -\mathbf{S} \cdot \hat{\mathbf{n}}_R$ , as can be seen from Eq. (3.3). It is the relative orientation of the accumulated spin and the drain (or source) magnetization,

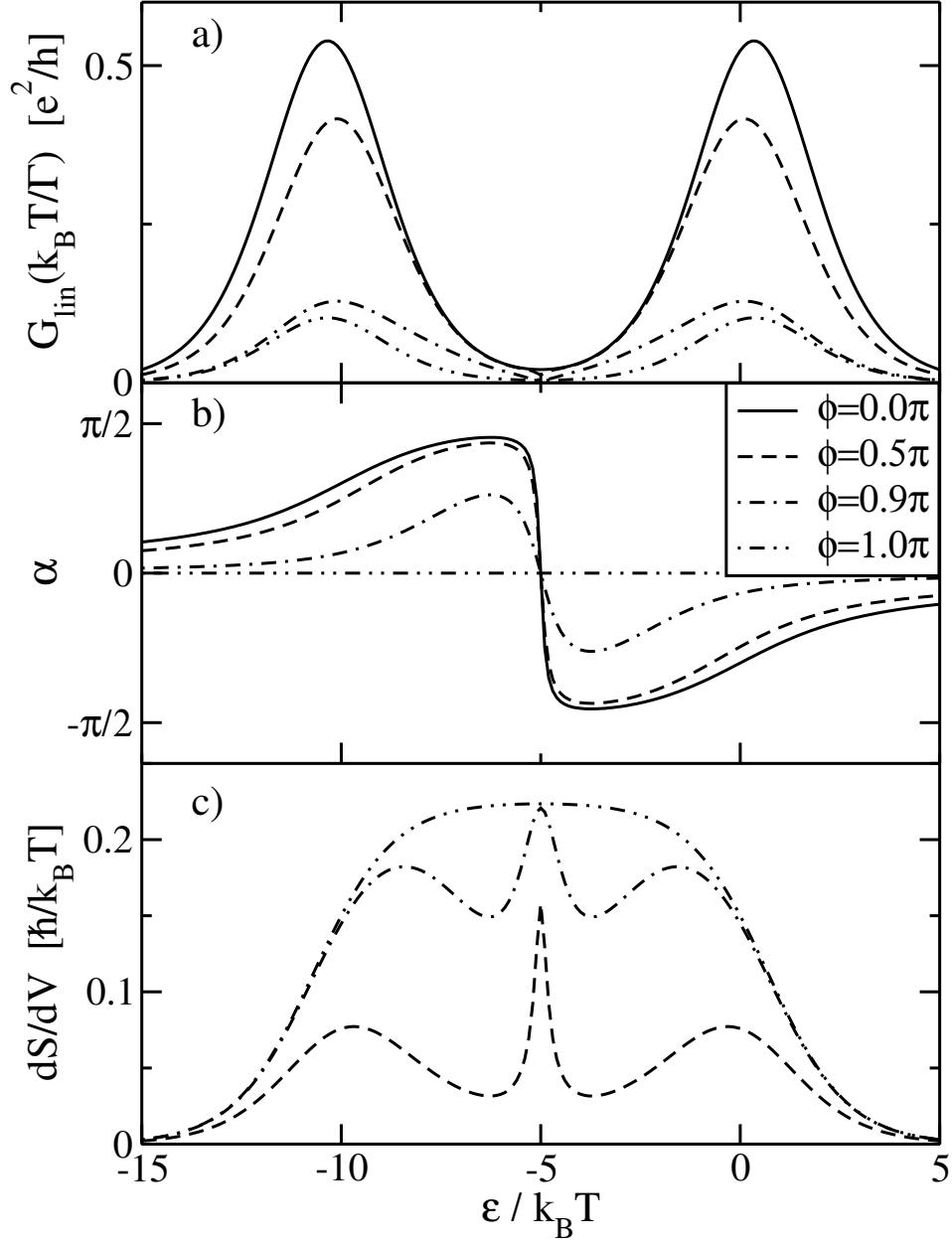


Figure 4.2: (a) Linear conductance normalized by  $\Gamma/k_B T$  as a function of the level position  $\varepsilon$  for different angles  $\phi$ . (b) Angle  $\alpha$  enclosed by the accumulated spin and the  $y$ -axis as defined in Fig. 4.1. (c) Derivation of the magnitude of the accumulated spin on the dot with respect to the source-drain voltage  $V$ . Further parameters are  $p = 0.9$ ,  $\tau_{\text{sf}}^{-1} = 0$  and  $U = 10k_B T$ .



that produces the  $\phi$ -dependence of the current, rather than the product  $\hat{\mathbf{n}}_L \cdot \hat{\mathbf{n}}_R$ , as in the case of a single magnetic tunnel junction. Therefore the  $\phi$ -dependent linear conductance  $G^{\text{lin}} = (\partial I / \partial V)|_{V=0}$  directly reflects the accumulated spin. The effect of the exchange field for the normalized conductance can be seen in the analytic expression

$$\frac{G^{\text{lin}}(\phi)}{G^{\text{lin}}(0)} = 1 - p^2 \frac{\tau_s}{\tau_c} \frac{\sin^2(\phi/2)}{1 + (B_0 \tau_s)^2 \cos^2(\phi/2)}, \quad (4.6)$$

where  $G^{\text{lin}}(0) = e^2 P_1 / \tau_c k_B T$ . The linear conductance is plotted in Fig. 4.3 as function of the opening angle of the lead magnetizations for different values of the level position  $\varepsilon$ .

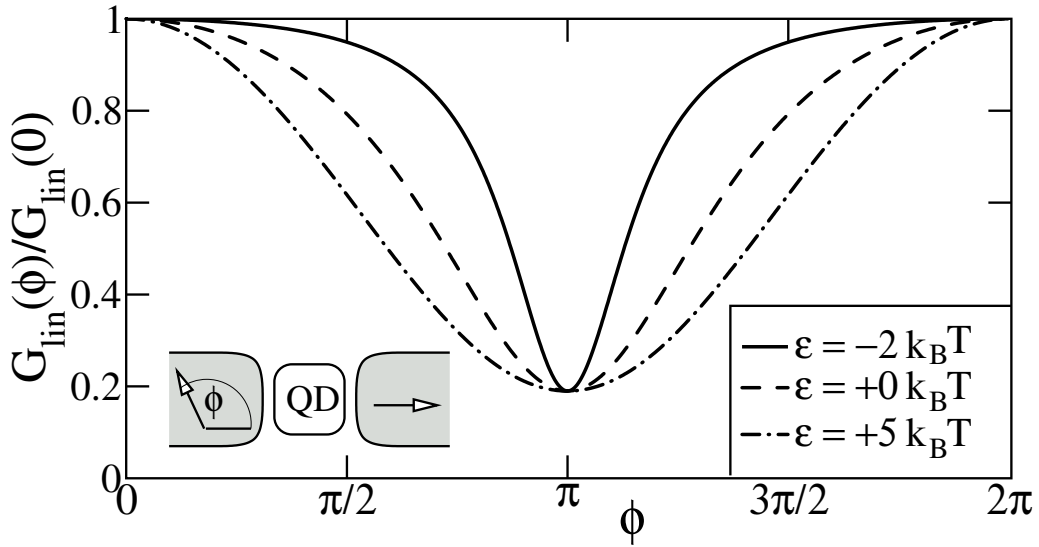


Figure 4.3: Normalized conductance as a function of the angle  $\phi$  enclosed by the lead magnetizations for different level positions and the parameters  $U = 10k_B T$ ,  $\tau_{\text{sf}}^{-1} = 0$  and  $p = 0.9$ .

For  $\varepsilon > 0$ , the quantum dot is predominantly empty, and for  $\varepsilon + U < 0$  doubly occupied with a spin singlet. In this regions, the life time of a singly occupied dot  $\tau_c$  is short, and so is the lifetime of the dot spin. Therefore the rotation angle  $\alpha$  is small and the normalized conductance as a function of the relative angle  $\phi$  enclosed by the lead magnetizations shows a harmonic behavior, see, e.g., the curve for  $\varepsilon = 5k_B T$  in Fig. 4.3.

For  $-U < \varepsilon < 0$  the dot is primarily singly occupied, therefore the spin dwell time is increased and the exchange field becomes important. It causes the above described spin precession, which decreases the angle between  $\mathbf{S}$  and  $\hat{\mathbf{n}}_R$  as well as decrease the magnitude of  $\mathbf{S}$ . Thus, the spin precession makes the spin-valve effect less pronounced, so that the conductance that exceeds the expectations [18] for a single magnetic tunnel junction.

For parallel and antiparallel aligned lead magnetizations,  $\phi = 0$  and  $\phi = \pi$ , the accumulated spin and the exchange field get aligned. In this case, the spin precession stops, even

though the exchange field is still present. The  $\phi$ -dependent conductance is not affected by the exchange field at this alignment, see Fig. 4.3.

## 4.2 Bias voltage effect in non-linear regime

We now turn to the non-linear response regime,  $eV > k_B T$ , in order to discuss the influence of the bias voltage dependence of the exchange field. We assume that there is no external magnetic field, and no spin relaxation. In Fig. 4.4(a) the current  $I$  is shown as a function of the bias voltage  $V$  for an antiparallel configuration of the lead magnetizations and different values of the leads' spin polarization  $p$ .

For non-magnetic leads, the current-voltage characteristic shows the usual Coulomb staircase. At low bias voltage, the dot is empty and transport is blocked. With increasing bias voltage, first single and then double occupancy of the dot is possible, which opens first one and then two transport channels. A finite spin polarization  $p$  causes spin accumulation and, thus, a reduction of transport. A reduction of transport with increasing  $p$  is also seen for non-collinear magnetizations. But there is a qualitative difference as can be seen in Fig. 4.4(b). A very pronounced negative differential conductance evolves out of the middle plateau as  $p$  is increased. To understand the negative differential conductance we first neglect the exchange field and then, in a second step, analyze how the exchange field modifies the picture.

At the intermediate bias voltages ( $\varepsilon \ll eV/2 \ll e + U$ ) the dot can only be empty or singly occupied. Since double occupation is forbidden, the transport through the dot is limited by the electron state with maximal dwell time in the dot. Due to the finite bias voltage, the dot electrons can only leave the dot to the drain (right) lead. Therefore, the electron with the longest dwell time is the one with its spin polarized antiparallel to the drain lead magnetization direction. For this antiparallel spin alignment the tunneling to the drain lead is maximally suppressed, while the tunneling from the source lead is not as much affected. When the tunneling to the drain lead is weak, but strong to the source lead, then the dot is primarily occupied by one electron (charge accumulation). The spin accumulation as function of the charge occupation  $P_1$  given by

$$\mathbf{S} = p \left[ \frac{\Gamma_L}{\Gamma_R} (1 - P_1) \hat{\mathbf{n}}_L - \frac{P_1}{2} \hat{\mathbf{n}}_R \right], \quad (4.7)$$

directly relates an increased probability  $P_1$  to find the dot occupied by one electron to an average dot spin  $\mathbf{S}$ , aligned nearly antiparallel to the drain lead.

The behavior is different from that in the linear-response regime, where the direction of the accumulated spin is along  $\hat{\mathbf{n}}_L - \hat{\mathbf{n}}_R$  rather than  $-\hat{\mathbf{n}}_R$ . This is related to the fact, that in the linear-response regime, the dot electrons can both tunnel to the source (left) and drain (right) lead (where tunneling to the drain is only somewhat more likely than tunneling to the source). The direction of the accumulated spin does, therefore, not only

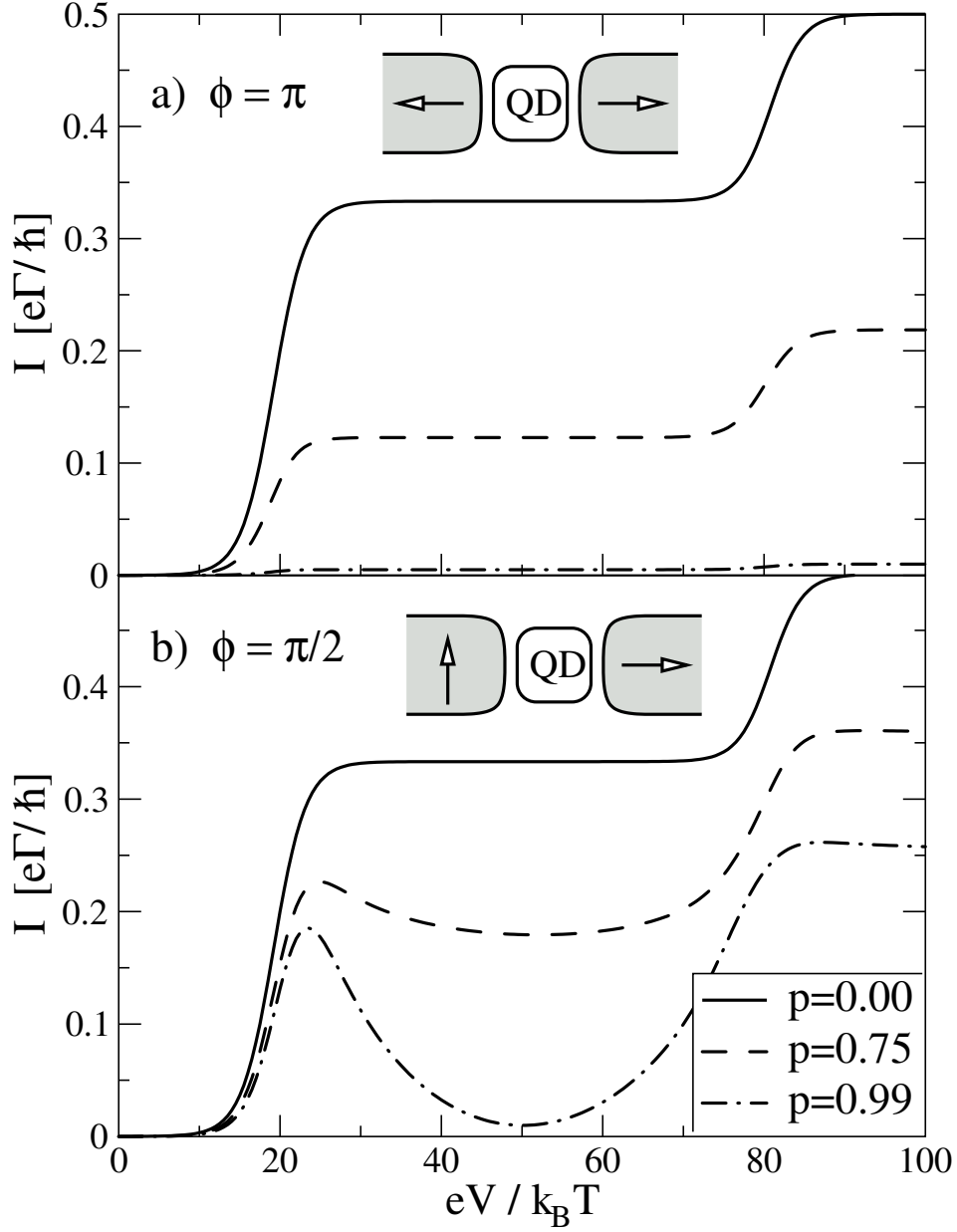


Figure 4.4: Current–voltage characteristics for antiparallel (a) and perpendicular aligned (b) lead magnetizations. Further parameters are  $\Gamma_L = \Gamma_R = \Gamma/2$ ,  $p_L = p_R = p$ ,  $\varepsilon = 10k_B T$ , and  $U = 30k_B T$ .

depend on the magnetization of the drain but also on that of the source electrode. To minimize transport, the accumulated spin will be aligned along  $\hat{\mathbf{n}}_L - \hat{\mathbf{n}}_R$ .

Due to the fact, that double occupation is forbidden,  $P_d \approx 0$ , all electrons entering

the dot through the left barrier must find an empty dot, i.e., the current  $I = (e\Gamma/\hbar)P_0$  explicitly depends only on the probability to find the dot empty. Therefore any additional charge accumulation,  $\sim P_1$ , on the dot reduces the conductance of the device proportional to  $P_0 = 1 - P_1$ . So this mechanism is a type of spin blockade but with a different physical origin compared to the systems described in literature [74–76]. The suppression defines the local minimum of the current in Fig. 4.4(b). At this point of the minimal current, the relevant exchange-field component generated by the coupling to the source (left) lead vanishes, see Fig. 4.6(a). Away from this point, the exchange field component perpendicular to the spin, (originating from the source lead) will induce a precession of this spin about  $\hat{\mathbf{n}}_L$  as illustrated in Fig. 4.5, and effectively diminish the spin blockade.

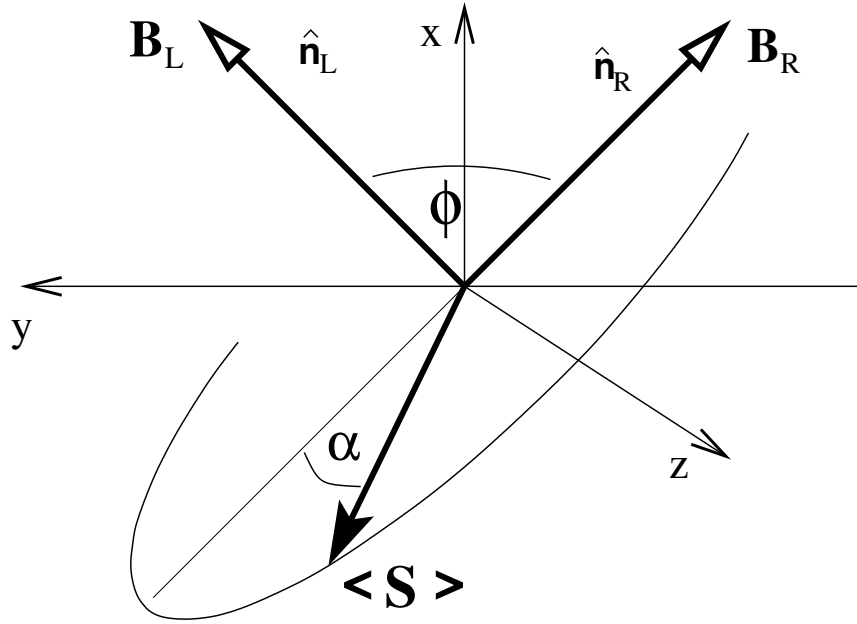


Figure 4.5: For electrons polarized antiparallel to the drain lead, the influence of the effective field generated by the source lead is dominating. By spin precession, the spin blockade is lifted and therefore the conductance recovers.

The particular value of the non-linear conductance is a consequence of the two competing effects. Spin blockade reduces, while spin precession, which reduces the spin blockade, again increases the conductance. Since the strength of the exchange field, which generates precession, varies as a function of bias voltage, see Fig. 4.6(a), this recovery is a non-monotonous function, generating the negative differential conductance.

To illustrate this further, in Fig. 4.6(b) the current is plotted which is obtained when the spin precession contribution is in an artificial way dropped in Eq. (3.14). In the absence of the exchange field, a wide plateau is recovered, whose height is similar to the current, one would expect, if the lead magnetizations were aligned antiparallel. The peak at the

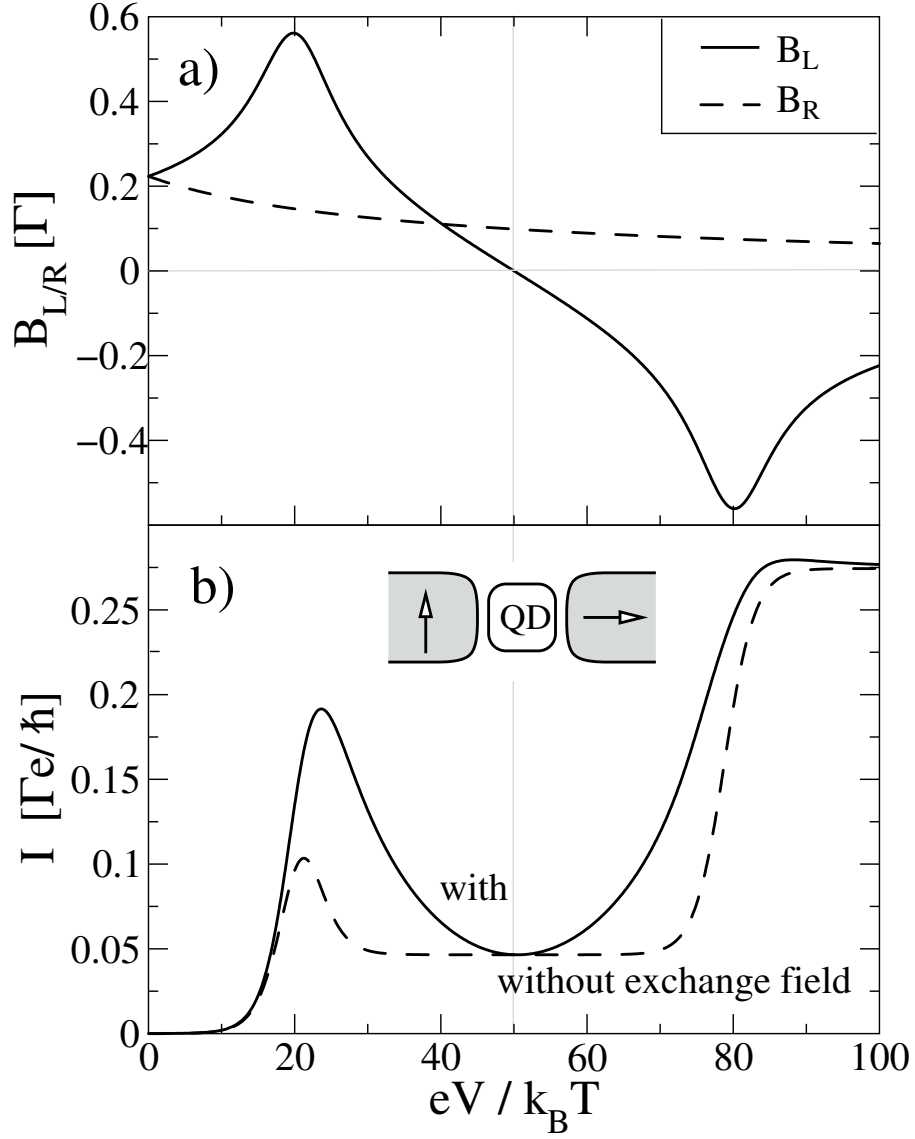


Figure 4.6: Panel (a): The absolute value of the effective exchange field contributions from the left and right lead. Panel (b): the current voltage dependence, with and without the influence of the exchange field. For both plots the parameters  $\phi = \pi/2$ ,  $\Gamma_L = \Gamma_R = \Gamma/2$ ,  $\varepsilon = 10k_B T$ ,  $U = 30k_B T$ , and  $p = 0.95$  were chosen.

left end of the plateau indicates that, once the dot level is close to the Fermi level of the source electrode, the spin blockade is relaxed since the dot electrons then have also the possibility to tunnel back to the source (left) side.

However, this negative differential conductance occurs only at relatively high values of the lead polarization. For symmetric tunnel coupling a spin polarization of  $p \approx 0.77$  is needed, while for a strong asymmetry in the tunnel coupling the required spin polarization is reduced.

The effect of the spin blockade on the  $\phi$ -dependence of the current is depicted in Fig. 4.7. We choose the bias voltage according to  $eV/2 = \varepsilon + U/2$ , such that the influence of the

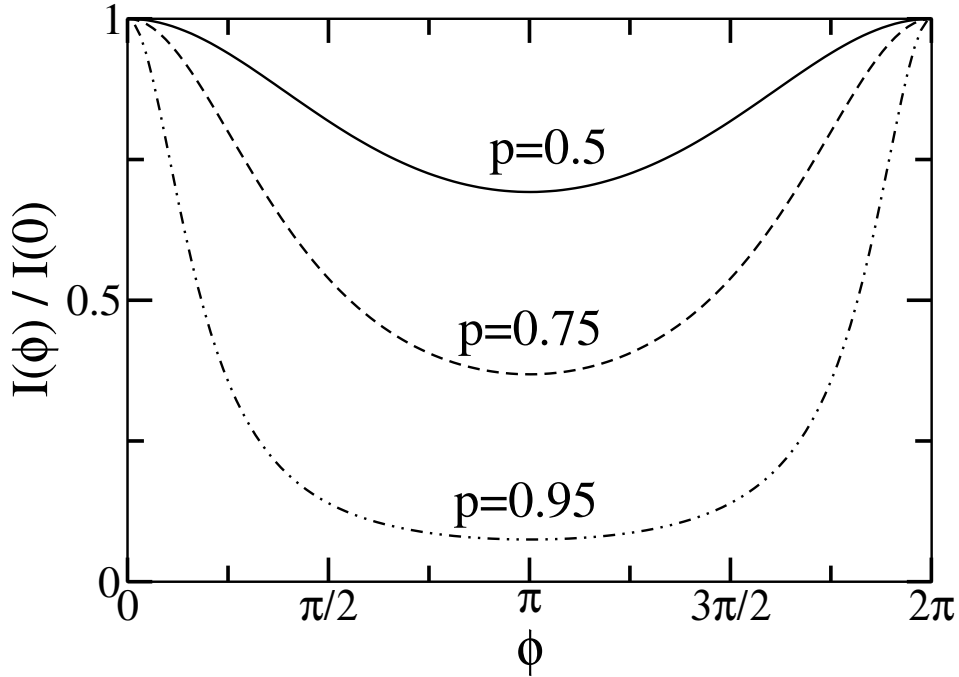


Figure 4.7: Angular dependence of the conductance with an applied voltage of  $V = \varepsilon + U/2$ , i.e., the voltage generating the smallest influence of the exchange field. Further plot parameters are  $\Gamma_L = \Gamma_R = \Gamma/2$ ,  $\varepsilon = 10k_B T$ , and  $U = 30k_B T$ .

exchange field is absent. For  $p = 0.5$  still a  $\sin^2(\phi/2)$  dependence can be recognized. For higher values of the spin polarization the conductance drops faster and stays nearly constant at its minimal value due to spin blockade. This is just the opposite behavior than predicted for the linear-response regime as seen in Fig. 4.3.

If such a high bias voltage is applied, that the dot can also be double occupied, the step like behavior of the current voltage characteristic is recovered, see Fig. 4.4(b). Away from the step, all appearing Fermi functions can be approximated by 0 or 1, and following Eq. (3.3) the current is given by  $I = (e\Gamma/2\hbar) [1 - p\mathbf{S} \cdot (\hat{\mathbf{n}}_L - \hat{\mathbf{n}}_R)]$ . Far away from the resonance, where the exchange field can be neglected, the accumulated spin is  $\mathbf{S} = p(\hat{\mathbf{n}}_L -$

$\hat{\mathbf{n}}_{\text{R}})/4$  from which we get

$$I = \frac{e\Gamma}{2\hbar} \left( 1 - p^2 \sin^2 \frac{\phi}{2} \right). \quad (4.8)$$

At this high bias voltage, transport through a quantum-dot spin valve resembles just the tunnel magnetoresistance characteristic of a single tunnel junction, where charging effects are of no importance.

We close this Section with the remark that while we plotted only results for the case  $\varepsilon > 0$ , in the opposite case  $\varepsilon < 0$  the current–voltage characteristics is qualitatively the same.

### 4.3 External magnetic fields and the Hanle effect

In the previous Sections were studied quantum-dot spin dynamics that is evoked by the exchange field. But one can also make use of an externally applied magnetic field  $\mathbf{B}_{\text{ext}}$  to manipulate the dot spin and with it the conductance of the quantum-dot spin valve. It turns out that this manipulation scheme offers a way to measure the spin coherence time  $T_2$  in an all electrical way. To emphasize this point, in this Section, an intrinsic spin relaxation on the dot is explicitly allowed. Then, the charge life time  $\tau_c^{-1} = \tau_{c,L}^{-1} + \tau_{c,R}^{-1}$  and the spin life time on the dot  $\tau_s^{-1} = \tau_c^{-1} + \tau_{\text{sf}}^{-1}$  separate.

While also spin-orbit coupling can cause spin relaxation on the quantum dot itself [77, 78], it is assumed, that due to the confinement of the electrons on the quantum dot the hyperfine interaction to the nuclear spins becomes dominant. Typical spin coherence times are of the order of ns [79–82].

An external applied field causes the Hanle effect, i.e., the decrease of spin accumulation in the quantum dot due to precession about a static magnetic field. Indeed, this was the effect used by originally Johnson and Silsbee [24] and others [43] to prove the existance of non-equilibrium spin accumulation. Optical realizations of such Hanle experiments [83] always involve an ensemble averaging over different dot realizations, such that the outcome of the measurement is  $T_2^*$  rather than  $T_2$ . By measuring the Hanle signal via the conductance through a quantum dot attached to ferromagnetic leads, this ensemble averaging is avoided.

For simplicity in this Section we assume again symmetric couplings  $\Gamma_L = \Gamma_R$ , equal degree of lead polarizations  $p_L = p_R = p$  and consider the linear-response regime only. There is a variety of possible relative orientations of the external field and the lead magnetizations to each other. In the following, two specific cases are discussed in detail, which are convenient to extract useful information about the spin decoherence time in one case, and to prove the existence of the exchange field in the other case.

### 4.3.1 Antiparallel aligned lead magnetizations

We first focus on two ferromagnetic leads with magnetization directions anti-parallel to each other, see Fig. 4.8, and an arbitrary aligned external field. The configuration has the advantage that the exchange field contributions from the two leads cancel, and the spin dynamics is only governed by the external field  $\mathbf{B}_{\text{ext}}$ . The linear conductance, then, is

$$\frac{G}{G_0} = 1 - p^2 \frac{\tau_s}{\tau_c} \frac{1 + \left(\frac{\hat{\mathbf{n}}_L - \hat{\mathbf{n}}_R}{2} \mathbf{B}_{\text{ext}} \tau_s\right)^2}{1 + (\mathbf{B}_{\text{ext}} \tau_s)^2}, \quad (4.9)$$

where  $G_0 = e^2 P_1 / \tau_c k_B T$  is the asymptotic value of the conductance for a large applied magnetic field,  $|\mathbf{B}_{\text{ext}}| \rightarrow \infty$ , for which the spin accumulation is completely destroyed. The asymptotic conductance is proportional to the single occupation probability  $P_1$ .

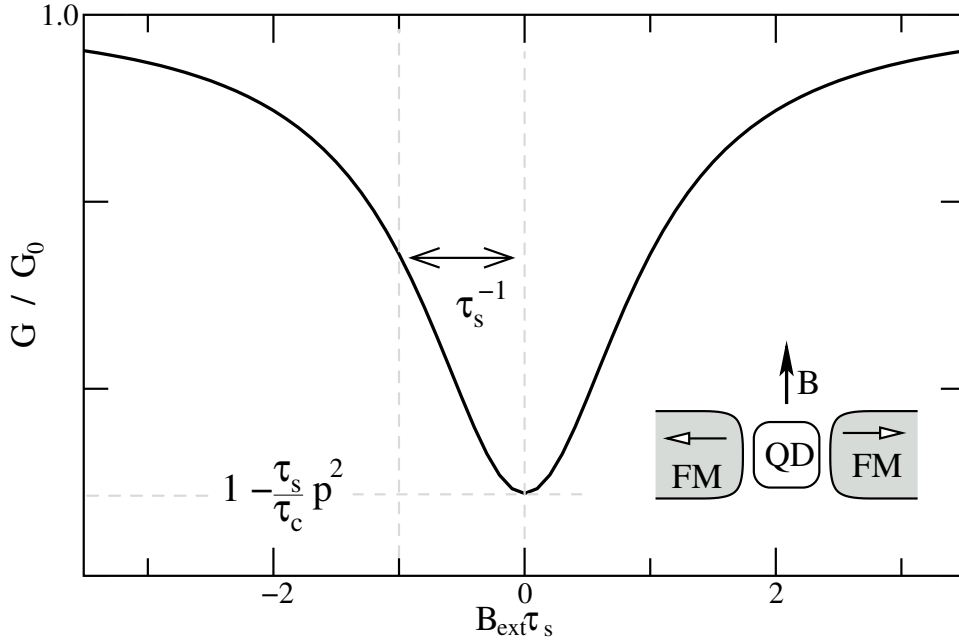


Figure 4.8: Differential conductance for ferromagnetic leads with anti-parallel magnetizations as a function of the magnetic field  $|\mathbf{B}_{\text{ext}}|$  applied perpendicular to the lead magnetizations. The half line width of the Hanle resonance directly determines the spin-decoherence time  $\tau_s$ .

If we assume the field to be aligned perpendicular to the lead magnetizations (see Fig. 4.8), the conductance depends Lorentzian on the external magnetic field, which is familiar from the optical Hanle effect. The depth of the dip is given by  $p^2 \tau_s / \tau_c$  while the width of the dip in Fig. 4.8 provides a direct access to the spin lifetime  $\tau_s$ . Of course, the conversion of applied magnetic field to frequency requires the knowledge of the Lande  $g$ -factor, which must be determined separately like in Ref. [48].



In a recent experiment Zhang *et. al.* [44] realized a similar kind of setup: a whole layer of aluminum dots were embedded in a tunnel junction between two Co electrodes, see Fig. 4.9, and a magnetic field was applied perpendicular to the lead magnetizations. In contrast to the setup with a single quantum dot, this experiment may be influenced by the multi-domain structure of the leads, by weak spots in the tunnel barrier, and by the ensemble averaging over different grains [44, 84].

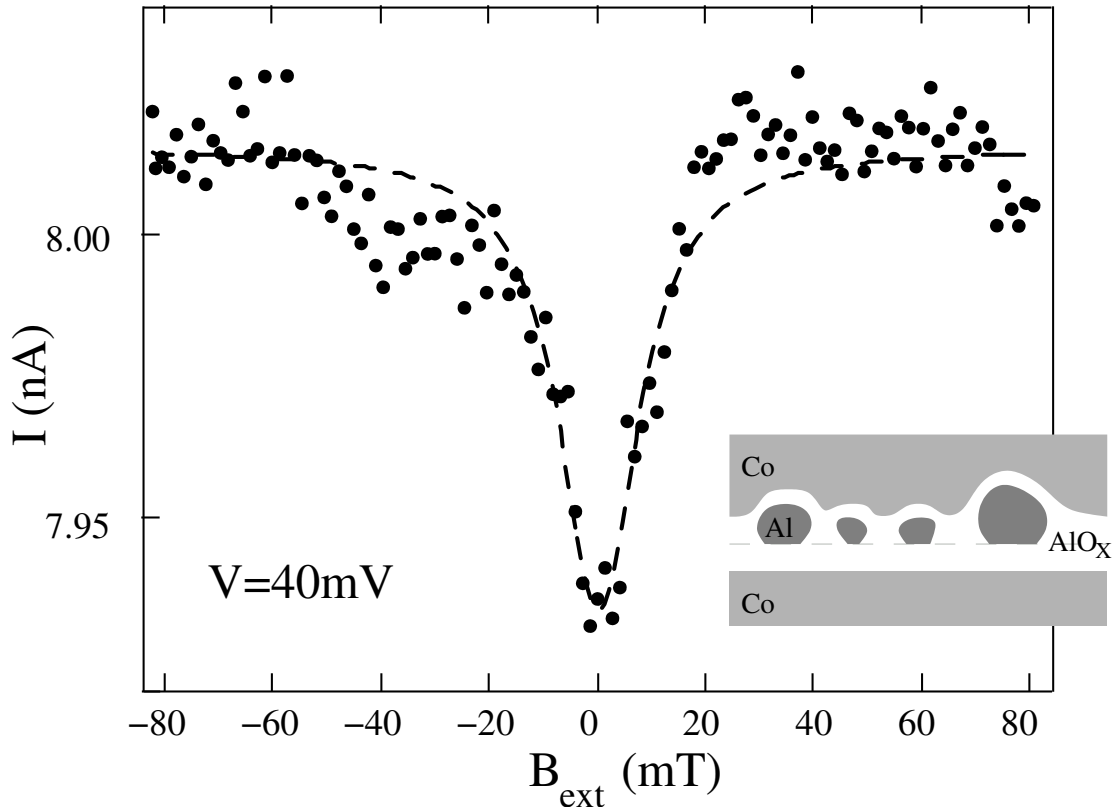


Figure 4.9: Measurement of the current versus applied magnetic field by Zhang *et. al.* [44]. The tunneling device consists of a  $\text{AlO}_x$  tunnel barrier between two Co leads. Inside the tunnel barrier metallic Al grains are embedded, serving as quantum dots.

Nevertheless, at first glance, the measured dependence of the conductance on the applied magnetic field in Fig. 4.9 seems to show the anticipated Hanle effect. However, this interpretation of the measurement has a serious drawback: the inverse linewidth falls significantly below the expected spin coherence time of the grains. Even so, this line broadening could be explained by collinear fringing fields of the order of 10 mT, alternative measurements on single grain structures indicate [84], that the fringing field strength is usually on the order of 100 mT, i.e., an order of magnitude larger. Therefore, the interpretation of the measurement as Hanle effect may not be the only possible one [84], and further experiments on individual nanoparticles are necessary to prove coherent precession of the

dot spins.

### 4.3.2 Magnetic field applied along $\hat{\mathbf{n}}_L + \hat{\mathbf{n}}_R$

Finally, we discuss the case of a non-collinear configuration of the lead magnetizations with a magnetic field applied along the direction  $\hat{\mathbf{n}}_L + \hat{\mathbf{n}}_R$  as shown in Fig. 4.10. In this case, both, the exchange field and the external magnetic field are pointing along the same direction  $\hat{\mathbf{n}}_L + \hat{\mathbf{n}}_R$ , and their magnitudes are just added. The linear conductance is, then,

$$\frac{G}{G_0} = 1 - p^2 \frac{\tau_s}{\tau_c} \frac{\sin^2 \frac{\phi}{2}}{1 + (\mathbf{B}_{\text{ext}} + \mathbf{B}_L + \mathbf{B}_R)^2 \tau_s^2}, \quad (4.10)$$

where  $\phi$  is the angle enclosed by  $\hat{\mathbf{n}}_L$  and  $\hat{\mathbf{n}}_R$ . The conductance versus applied magnetic field is plotted in Fig. 4.10(a). The conductance reaches its minimal value when the sum of external and exchange field vanishes. Therefore, the exchange field shifts the minimums position relative to  $|\mathbf{B}_{\text{ext}}| = 0$ .

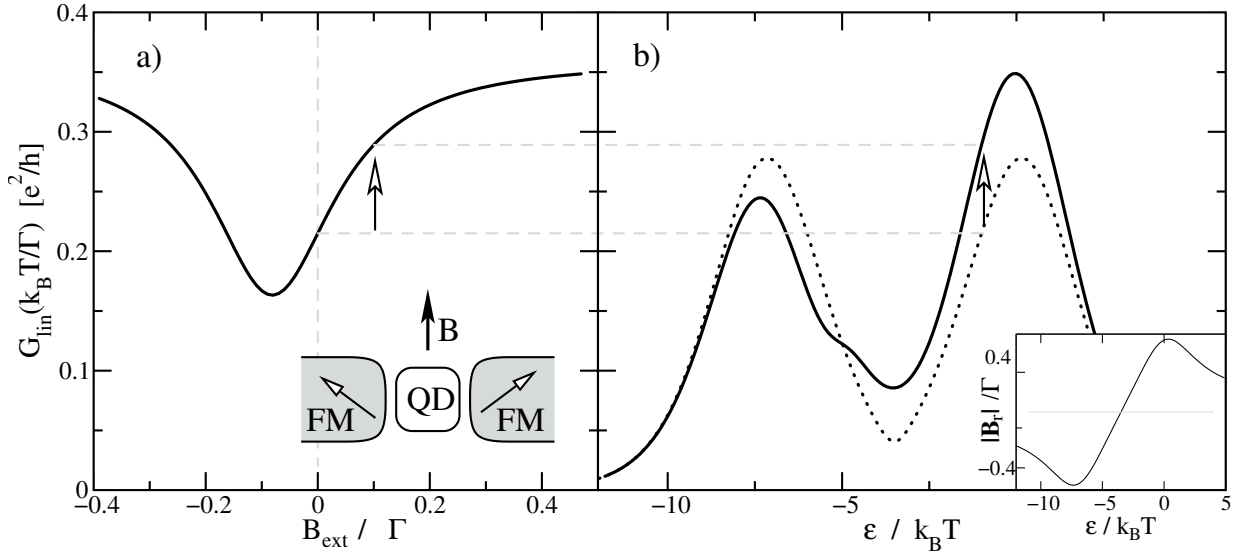


Figure 4.10: Linear conductance of the dot for an applied external magnetic field  $\mathbf{B}_{\text{ext}}$  along  $\hat{\mathbf{n}}_L + \hat{\mathbf{n}}_R$ . a) Linear conductance as a function of the applied field for  $\varepsilon = 0$ . b) Linear conductance as a function of level position  $\varepsilon$  without external field (dotted) and for the applied field  $|\mathbf{B}_{\text{ext}}| = 0.1\Gamma/\hbar$  (solid). Further parameters are  $\phi = 3\pi/4$ ,  $p = 0.8$ ,  $U = 7k_B T$ , and  $\tau_{\text{sf}} = 0$ . The vertical lines relate the conductance increase of the dot at  $\varepsilon = 0$  for a magnetic field  $|\mathbf{B}_{\text{ext}}| = 0.1\Gamma/\hbar$ .

In real experiments, depending on the particular sample geometry, one can expect a magnetic stray field, which is not considered to be part of the experimentally applied magnetic field  $\mathbf{B}_{\text{ext}}$ . This stray field also shifts the conductance minimum. However,

the analyzed setup of external field and magnetization directions allows for a stringent experimental verification of spin precession due to the exchange field. To separate the exchange field from the influence of a possible stray field, the gate voltage dependence of the exchange interaction can be used. The exchange interaction as function of the dot gate voltage is plotted in the inset of Fig. 4.10(b). While the stray field does not depend on gate voltage, the exchange field does. In the flat band limit it even changes sign as a function of gate voltage. By plotting the conductance as function of the gate voltage in Fig. 4.10(b), the typical Coulomb blockade oscillations can be observed. Each time, the energy level of the empty or singly occupied dot becomes resonant with the lead Fermi energy, the conductance bears a resonance. The interplay of exchange and external field leads to an increase of conductance for one resonance peak, but to a decrease for the other resonance.

## 4.4 Chapter summary

We discussed the possibility to generate, manipulate, and probe single spins in single level quantum dots coupled to ferromagnetic leads. Any manipulation of the accumulated spin, e.g. by the external magnetic field or by the intrinsic exchange field, is detectable in the electric current through the device.

A spin polarization of the quantum-dot electron is achieved by spin injection from the leads. The spin current through a tunnel barrier bears a contribution that is associated with the spin polarization of the charge currents from or to ferromagnets. Further, a conceptional different contribution arises, describing transfer of angular momentum perpendicular to the lead magnetization and the dot polarization. This contribution can be expressed in terms of the exchange field. The occurrence of the exchange field is a consequence of many-body correlations that are one of the intriguing features of nanostructures with large Coulomb interaction.

In order to manipulate the quantum-dot spin we suggest to apply an external magnetic field, or, more interestingly, make use of the gate and bias voltage dependence of the exchange field. In particular, the spin precession modifies the dependence of the linear conductance on the opening angle of the lead magnetizations. The strength of this modification is tunable by the gate voltage. In nonlinear response, the bias voltage dependence of the exchange field can give rise to a negative differential conductance. By applying a tunable external magnetic field, one can realize an all electrical Hanle experiment, which determines the dot-spin lifetime of a single dot and is furthermore capable to verify the existence of the intrinsic spin precession caused by the exchange field.



# Chapter 5

## Time Resolved Spin Dynamics via Frequency Dependent Current Noise

In the previous Chapters, we discussed in detail, how the time-averaged dot spin affects the time-averaged current. However, a way to resolve the time-dependent dynamics of the dot spin is provided by the power spectrum of the current noise. Spin precession due to an external magnetic and/or the exchange field affects the Fano factor of the system in two ways. First, the tendency towards spin-selective bunching of the transmitted electrons is suppressed, which gives rise to a reduction of the low-frequency noise. Second, the noise spectrum displays a resonance at the Larmor frequency, whose lineshape depends on the relative angle of the lead magnetizations.

### 5.1 Introduction

That current noise reveals additional informations about mesoscopic conductors, which are not contained in the average current was already pointed out before [85, 86]. For example current noise through quantum dots reveals the strongly correlated character of charge transport, giving rise to phenomena such as positive cross correlations [28] and sub- or superpoissonian Fano factors [87, 88]. This is one motivation for the extensive theoretical [89–94] and experimental [95–99] study of zero- and finite-frequency current noise through quantum dots.

The property, which will be utilized in this Chapter is, that the finite-frequency noise provides also a direct access to the internal dynamics of mesoscopic systems such as coherent oscillations in double-dot structures [100–103], quantum-shuttle resonances [104], transport through a dot with a precessing magnetic moment [60], the dissipative dynamics of a qubit [105], or back action of a detector on the system [106–108]. In the case of a quantum-dot spin valve, the current-current correlation function will show a signature at the frequency that is associated with the precession of the quantum-dot spin due to the

sum of exchange and external magnetic field.

The origin of the signal in the current noise can be understood by looking at the tunneling-out current to the drain (right) lead as a function of the time after the quantum-dot electron had tunneled in from the source (left) lead. The spin of the incoming electron, defined by the source-lead magnetization direction, precesses about the sum of exchange and external magnetic field as long as the electron stays in the dot. Since the tunneling-out rate, influenced by tunnel magnetoresistance, depends on the relative orientation of the quantum-dot spin to the drain-lead magnetization direction, there is a periodic oscillation of the tunneling-out probability. The oscillation period is defined by the inverse precession frequency. Depending on the relative orientation of the source- and drain-lead magnetization directions, the tunneling-out rate is either increased or decreased after one full rotation of the quantum-dot spin. As a consequence, the signature in the power spectrum of the current noise at the Larmor frequency gradually changes from a peak to a dip as a function of angle between source- and drain-lead magnetization.

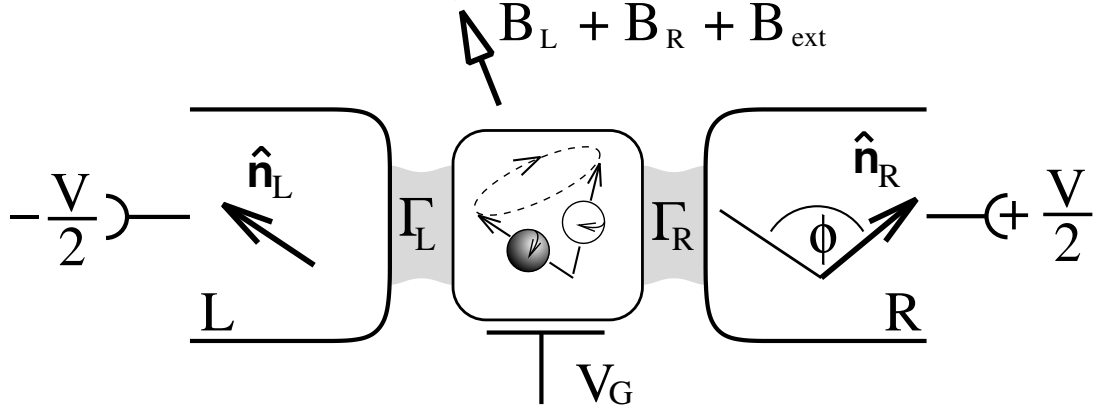


Figure 5.1: A quantum dot contacted by ferromagnetic leads with non-collinear magnetizations. Electrons polarized along the source (left) lead enter the dot. During their stay on the dot, the electrons precess in the many-body exchange field  $\mathbf{B}_L + \mathbf{B}_R$  and an external magnetic field  $\mathbf{B}_{\text{ext}}$ . Due to magnetoresistance effects this precession modulates the tunnel-out probability to the drain (right) lead, giving rise to a resonance signal in the current power spectrum.

Also the low (zero) frequency part of the current-noise power spectrum is affected by the internal dynamics of the quantum-dot spin. By coupling a quantum dot to spin-polarized electrodes, the dwell time of the electrons in the dot becomes spin dependent. It is known [28, 109] that this spin dependence of the dwell times yields a bunching of the transferred electrons. This bunching leads to an increase of the shot noise. A precession of the quantum-dot spin weakens the tendency towards bunching, leading to a reduction of the low-frequency noise.

In order to illustrate the ideas formulated above, we present a systematic study of the frequency-dependent current noise in the following. A previously-developed diagrammatic

real-time technique [65] is extended to evaluate frequency-dependent current noise in Section 5.2. Similar approaches for metallic (non-magnetic) single-electron transistors were presented in Refs. [106,110]. The results for the quantum-dot spin valve are then discussed in Section 5.3.

## 5.2 Diagrammatic Technique

The same mathematical model for the quantum-dot spin valve is considered as introduced in Chapter 2. The quantum dot consists of a single electronic state at energy  $\varepsilon$ , and double occupancy of the dot costs the charging energy  $U \gg k_B T$ . The ferromagnetic leads ( $r = L/R$ ) are reservoirs of non-interacting fermions, which bear a spin polarization  $p_r$  along the direction of magnetization  $\hat{\mathbf{n}}_r$ . The dot is tunnel coupled to the leads by the coupling strength  $\Gamma_r = \sum_{\alpha=\pm} 2\pi |t_r/\sqrt{2}|^2 \xi_\alpha$ , which for simplicity, is assumed to be energy independent.

In the following three subsections, the derivation for the stationary density matrix, the  $dc$ -current and the finite-frequency current-current correlation function is formulated. Afterwards, in Section 5.2.4, the obtained formulas are specified for the limit of weak dot-lead coupling, i.e., for a systematic lowest-order perturbation expansion in the tunnel coupling strength  $\Gamma = \Gamma_L + \Gamma_R$ . It is worth to mention, that as long as the specific rates are not introduced, the derivation of the density matrix, the current and the current-current correlation function would also be applicable for any tunnel-coupled quantum-dot problems, not only a quantum-dot spin valve.

### 5.2.1 Quantum-dot density matrix

The dynamics of the quantum-dot spin valve is determined by the time evolution of the total density matrix. Since the leads are modeled by non-interacting fermions, which always stay in equilibrium, their degrees of freedom can be integrated out. The quantum-statistical average of the charge and spin on the quantum dot at time  $t$  is then encoded only in the reduced dot density matrix  $\boldsymbol{\rho}(t)$ , as introduced in Chapter 2. Its time evolution is governed by the propagator  $\boldsymbol{\Pi}(t, t_0)$ ,

$$\boldsymbol{\rho}(t) = \boldsymbol{\Pi}(t, t_0) \cdot \boldsymbol{\rho}(t_0). \quad (5.1)$$

Since  $\boldsymbol{\rho}$  is a matrix, the propagator  $\boldsymbol{\Pi}$  must be a tensor of rank four. A diagrammatic representation of this equation is depicted in Fig. 5.2. The upper (lower) horizontal line represents the propagation of the individual dot states forward (backward) in real time, i.e., along a Keldysh time contour  $t_K$ . The rigid mathematical derivation of this approach can be found in Ref. [65], and citations therein.

In order to find the stationary density matrix for a system, which is described by a time-independent Hamiltonian, one can consider the limit  $t_0 \rightarrow -\infty$ . There is some

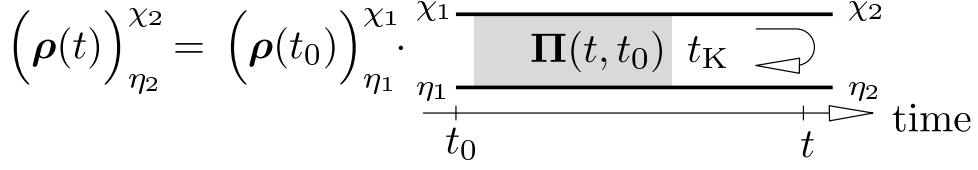


Figure 5.2: The density matrix evolves in time with the propagator  $\mathbf{\Pi}$ , which is a tensor of rank four.

characteristic time after which the system loses the information about its initial density matrix  $\rho_{\text{ini}} = \lim_{t_0 \rightarrow -\infty} \rho(t_0)$ . Therefore, without loss of generality we can choose  $(\rho_{\text{ini}})_{\eta_1}^{\chi_1} = \delta_{\chi_1, \chi_0} \delta_{\eta_1, \chi_0}$  with an arbitrarily-picked state  $\chi_0$ , to get for the stationary non-equilibrium density matrix

$$(\rho_{\text{st}})_{\eta_2}^{\chi_2} = \lim_{t_0 \rightarrow -\infty} \Pi(t - t_0)_{\eta_2 \chi_0}^{\chi_2 \chi_0}, \quad (5.2)$$

independent of  $\chi_0$ . Here, for time-translation invariant systems, the propagator  $\mathbf{\Pi}(t, t_0)$  depends only on the difference of the time arguments  $(t - t_0)$ . For the following, it is convenient to express the propagator in frequency representation  $\mathbf{\Pi}(\omega) = \hbar^{-1} \int_{-\infty}^0 dt \mathbf{\Pi}(-t) \exp[i(\omega - i0^+)t]$ . It can be constructed by the Dyson equation

$$\begin{aligned} \mathbf{\Pi}(\omega) &= \mathbf{\Pi}_0(\omega) + \mathbf{\Pi}_0(\omega) \mathbf{W}(\omega) \mathbf{\Pi}(\omega) \\ &= [\mathbf{\Pi}_0^{-1}(\omega) - \mathbf{W}(\omega)]^{-1}. \end{aligned} \quad (5.3)$$

The full propagator  $\mathbf{\Pi}(\omega)$  depends on the free propagator  $\mathbf{\Pi}_0(\omega)$  and the irreducible self-energies  $\mathbf{W}(\omega)$ , which describes the influence of tunneling events between the dot and the leads. The Dyson equation is diagrammatically represented in Fig. 5.3. The frequency argument of the Laplace transformation appears in this diagrammatic language as additional horizontal bosonic line transporting energy  $\hbar\omega$ .

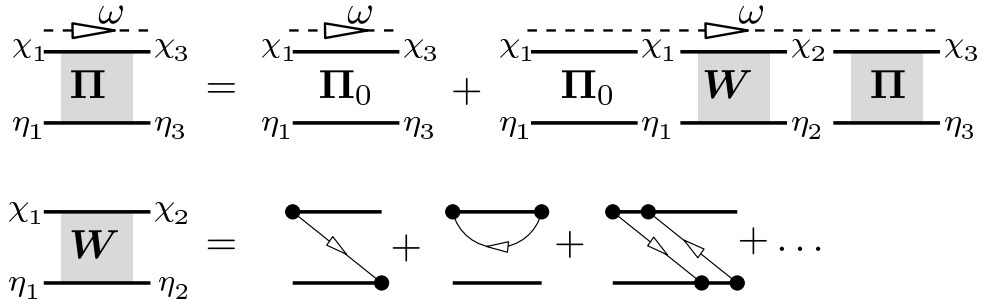


Figure 5.3: Diagrammatical representation of the Dyson equation for the propagator. The self-energy  $\mathbf{W}$  sums up all irreducible tunnel diagrams. With  $\mathbf{W}(\omega)$ , we label the self-energy, together with the parallel running frequency line  $\omega$ .



The free propagator (without tunneling) is given by

$$\Pi_0(\omega)_{\eta_2\eta_1}^{\chi_2\chi_1} = \frac{i\delta_{\eta_1\eta_2}\delta_{\chi_1\chi_2}}{\varepsilon_{\eta_1} - \varepsilon_{\chi_1} - \hbar\omega + i0^+}, \quad (5.4)$$

where  $\varepsilon_\chi$  ( $\varepsilon_\eta$ ) is the energy of the dot state  $\chi$  ( $\eta$ ) = {0,  $\uparrow$ ,  $\downarrow$ , d}. Tunneling between the dot and the leads introduce the irreducible self-energies  $\mathbf{W}(\omega)$ . The self-energies  $\mathbf{W}(\omega)$  can be calculated in a perturbation expansion in the tunnel Hamiltonian. Each tunnel Hamiltonian generates one vertex (filled circle), on the Keldysh time contour  $t_K$ , see Fig. 5.3. Since the leads are in equilibrium, their fermionic degrees of freedom can be integrated out. Thereby two tunnel Hamiltonians each get contracted, symbolized by a line. Each line is associated with one tunnel event, transferring one particle and a frequency/energy from one vertex to the other. Therefore the lines have a defined direction and bear one order of the coupling constant  $\Gamma = \Gamma_L + \Gamma_R$ . The self-energy  $\mathbf{W}(\omega)$  is defined as the sum of all irreducible tunnel diagrams (diagrams, which can not be cut at any real time (cut vertically), without cutting one tunneling line).

In Section 5.2.4, the calculation will then be restricted to the lowest-order expansion in  $\Gamma$ , where only diagrams with one tunnel line in  $\mathbf{W}(\omega)$  are included. A detailed description of how to calculate these lowest-order self-energies for the quantum-dot spin valve problem can be found in Appendix B.

To solve for the stationary density matrix  $\rho_{st}$ , one can rewrite the Dyson Eq. (5.3) as  $(\Pi_0(\omega)^{-1} - \mathbf{W}(\omega))\Pi(\omega) = \mathbf{1}$ , multiply both sides of the equation with  $\omega$ , use the final value theorem  $\lim_{\omega \rightarrow 0}(i\hbar\omega + 0^+)\Pi(\omega) = \lim_{t \rightarrow \infty} \Pi(t)$ , similar as for Laplace transformations, and employ Eq. (5.2), to get

$$\mathbf{0} = \left[ \Pi_0^{-1}(\omega = 0) - \mathbf{W}(\omega = 0) \right] \rho_{st} \quad (5.5)$$

together with the normalization condition  $\text{Tr}[\rho_{st}] = 1$ . For the individual density matrix elements  $P_\eta^\chi$ , the equation becomes

$$0 = -i(\varepsilon_\chi - \varepsilon_\eta)(\rho_{st})_\eta^\chi + \sum_{\chi_1, \eta_1} W_{\eta\eta_1}^{\chi\chi_1}(\rho_{st})_{\eta_1}^{\chi_1}. \quad (5.6)$$

The structure of Eq. (5.5) motivates the interpretation of the equation as a master equation in Liouville space, with the self-energy  $\mathbf{W}(\omega = 0)$  as generalized transition rates. However, the self-energy does not only describe real particle transfer between leads and dot, but it also accounts for tunnel-induced renormalization effects. In Chapter 4, it was shown, that these level renormalization affect even the lowest-order contribution to the conductance. Therefore, a neglect of these renormalizations would break the consistency of the lowest-order expansion in the tunnel coupling strength [26, 101, 111]. Recently, the frequency-dependent current noise of a quantum-dot spin valve structure was discussed in Ref. [112], in the limit of infinite bias voltage, where these level renormalizations can be neglected. One of the main advantages of the approach presented here is that a rigid systematic computation of the generalized transition rates is possible, which includes all renormalization effects. Therefore this approach is valid for arbitrary bias voltages.

The current through barrier  $r = \text{L, R}$  is defined as the change of charge  $en_r = e \sum_{k\sigma} a_{rk\sigma}^\dagger a_{rk\sigma}$  in lead  $r$  due to tunneling, described by the operator

We define the operator for the current through the dot as  $\hat{I} = (\hat{I}_L - \hat{I}_R)/2$ . Each term of the resulting current operator does contain a product of a lead and a dot operator. By integrating out the lead degrees of freedom, the current vertex (open circle) gets connected to a tunnel vertex by a contraction line as depicted in Fig. 5.4. Thereby the connected tunnel vertex can be either on the upper or lower time contour line.

Figure 5.4: Diagrammatic representation of the current. By integrating out the lead degrees of freedom, the current vertex (open circle) gets contracted to one of the tunnel vertices in the self-energy  $\mathbf{W}(\omega = 0)$ .

To present a systematic way to calculate the current, one can utilize the close similarity of the tunnel Hamiltonian and the current operator in Eq. (5.7). Both differ only by the prefactor  $e/\hbar$  and possibly by additional minus signs.

Thielmann *et al.* [92] introduced the object  $W_{\eta_1\eta}^{IXIX}$  as the sums of all possible realizations of replacing one tunnel vertex (filled circle) by a current vertex (open circle) in the self-energy  $W_{\eta_1\eta}^{XIX}$ , compare Fig. 5.5. In technical terms, this means that each diagram is multiplied by a prefactor, determined by the position of the current vertex inside the diagram. If the current vertex is on the upper (lower) Keldysh time branch, and describes a particle tunneling into the right (left) lead or out of the left (right) lead, multiply the diagram by  $+1/2$ , otherwise by  $-1/2$ . For clarity, the factor  $e/\hbar$  is kept separately. A more detailed explanation of the technical procedure of the replacement as well as the rules to construct and calculate the self-energies can be found in Ref. [92]. The average of one current operator, which equals the  $dc$ -current flowing through the system is then given by

The trace selects the diagonal matrix elements, which regards that the Keldysh line must be closed at the end of the diagram, see Fig. 5.5, requiring that the dot state of the upper and lower time branch match.

To see that the diagrams in Fig. 5.4 and Fig. 5.5 are equal, one must consider that all diagrams where the rightmost vertex is a tunnel vertex will cancel each other when



as an additional bosonic energy line (dashed) running from  $t$  to 0, i.e., between the two current vertices [110]. This line must not be confused with a tunnel line, since it only transfers energy  $\hbar\omega$ , and no particle. By introducing the self-energy  $\mathbf{W}$  all diagrams of the current-current correlation function can be grouped in two different classes [92, 110] as shown in Fig. 5.6. Either both current vertices are incorporated in the same irreducible block diagram, or into two different ones that are separated by the propagator  $\mathbf{\Pi}(\omega)$ .

$$\begin{aligned}
 & \left( \langle \hat{I}(t) \hat{I}(0) \rangle + \langle \hat{I}(0) \hat{I}(t) \rangle \right) e^{-i\omega t} = \\
 & = \rho_{\text{st}} \cdot \text{[Diagram 1]} + \rho_{\text{st}} \cdot \text{[Diagram 2]} + \\
 & \quad + \text{diagrams with one or both vertices on the lower line}
 \end{aligned}$$

Figure 5.6: Regrouping of the noise expansion by introducing the irreducible self-energy  $\mathbf{W}$ , and the propagator  $\mathbf{\Pi}(\omega)$ .

The order of the current operator on the Keldysh contour is determined by its ordering in the correlator. The current operator at time 0 lies on the upper branch for  $\langle \hat{I}(t) \hat{I}(0) \rangle$  and on the lower branch for  $\langle \hat{I}(0) \hat{I}(t) \rangle$ , compare Appendix A. Since in Eq. (5.9) the noise was defined symmetrized with respect to the operator ordering, just every combination of current vertex replacements in the  $\mathbf{W}$ 's are allowed. This includes also diagrams where one or both vertices are located on the lower time contour (these types of diagrams are not explicitly drawn in Fig. 5.6).

By including the current vertices and the frequency line in the self-energies, three variants of the self-energy  $\mathbf{W}$  are generated. The objects  $\mathbf{W}_{>}^I(\omega)$  and  $\mathbf{W}_{<}^I(\omega)$  are the sum of all irreducible diagrams, where one tunnel vertex is replaced by a current vertex in any topological different way. The subindex  $>$  ( $<$ ) indicates, that the frequency line connected to the current vertex leaves or enters the diagram to the right (left) side. In the zero-frequency limit, the two objects become equal  $\mathbf{W}_{>}^I(\omega = 0) = \mathbf{W}_{<}^I(\omega = 0) \equiv \mathbf{W}^I$ .

The third object  $\mathbf{W}^{II}(\omega)$  sums irreducible diagrams with two tunnel vertices replaced each by a current vertex in any topological different way. The current vertices are connected by the frequency line  $\omega$ . The diagrammatical picture of the objects  $\mathbf{W}(\omega)$ ,  $\mathbf{W}^{II}(\omega)$ ,  $\mathbf{W}_{>}^I(\omega)$ , and  $\mathbf{W}_{<}^I(\omega)$  are shown in Fig. 5.7.

With these definitions the diagrams for the frequency-dependent noise in Fig. 5.6 can be directly translated into the formula

$$\begin{aligned}
 S(\omega) = & \frac{e^2}{2\hbar} \text{Tr}[\mathbf{W}^{II}(\omega) \rho_{\text{st}} + \mathbf{W}_{<}^I(\omega) \mathbf{\Pi}(\omega) \mathbf{W}_{>}^I(\omega) \rho_{\text{st}}] \\
 & - 2\pi\delta(\omega) \langle \hat{I} \rangle^2 + (\omega \rightarrow -\omega).
 \end{aligned} \tag{5.10}$$

$$\begin{aligned}
\mathbf{W}(\omega) &= \text{Diagram 1} \\
\mathbf{W}_{>}^I(\omega) &= \text{Diagram 2} + \text{Diagram 3} \\
\mathbf{W}_{<}^I(\omega) &= \text{Diagram 4} + \text{Diagram 5} \\
\mathbf{W}^{II}(\omega) &= \text{Diagram 6} + \text{Diagram 7} \\
&+ \text{Diagram 8} + \text{Diagram 9}
\end{aligned}$$

Figure 5.7: Different variations of the self-energy  $\mathbf{W}$ . For  $\omega \rightarrow -\omega$ , the direction of the frequency line gets reversed.

The first line in Eq. (5.10) diverges as  $\omega \rightarrow 0$ . While the  $\mathbf{W}$ 's are regular for  $\omega \rightarrow 0$ , the propagator  $\mathbf{\Pi}(\omega)$  goes as  $i/(-\hbar\omega + i0^+)$  times  $\mathbf{\Pi}(t \rightarrow \infty)$ , which is related to  $\rho_{\text{st}}$  via Eq. (5.2). In the limit  $\omega \rightarrow 0$  the propagator therefore yields both a delta function  $\delta(\omega)$  and a  $1/\omega$  divergence. For the full expression of the noise, these divergences are canceled by the delta-function term in the second line of Eq. (5.10) and by the terms with  $\omega \rightarrow -\omega$ , respectively. As a consequence,  $S(\omega)$  remains regular also in the limit  $\omega \rightarrow 0$ .

#### 5.2.4 Low-frequency noise in the sequential-tunnel limit

The Equation (5.10) is the general expression for the frequency-dependent current noise. In the rest of the Chapter, we consider only the limit of weak dot-lead tunnel coupling,  $\Gamma \ll k_B T$ . Therefore only diagrams with at most one tunnel line are included in the  $\mathbf{W}$ 's. However, this procedure is not a consistent expansion scheme for the noise  $S(\omega)$  itself. By expanding the  $\mathbf{W}$ 's up to linear order in  $\Gamma$ , the result of Eq. (5.10) is the consistent noise linear in  $\Gamma$  plus some higher-order contributions proportional to  $\Gamma^2$ . Since co-tunnel processes also give rise to quadratic contributions, these terms must be discarded as long

as the quadratic cotunnel contributions of  $\mathbf{W}$  are neglected. If one is interested in the noise up to second order in  $\Gamma$ , then these higher-order terms generated by lower-order  $\mathbf{W}$ 's are, of course, an essential part of the result [117].

The interesting frequency parameter regime is - if one neglect external magnetic fields at this point - if the frequency is at most of the same order of the tunnel coupling  $\Gamma$ . In this parameter regime, the frequency-dependent current noise shows signatures of the internal charge and spin dynamics of the quantum dot. By limiting the frequency range to  $\hbar\omega \lesssim \Gamma$ , the frequency dependence of the  $\mathbf{W}$ 's can be neglected. Each correction of the  $\mathbf{W}$ 's would scale at least with  $\omega\Gamma \approx \Gamma^2$ , making them as important as the neglected co-tunnel processes.

The neglect of the terms in  $\mathbf{W}$  which are at least linear in frequency has two main advantages. First, it considerably simplifies the calculation of the  $\mathbf{W}$ 's. Second, it automatically removes the quadratic parts of the noise, so Eq. (5.10) gives a result consistent in linear order in  $\Gamma$ . In this low-frequency limit, the noise can then be written as

$$S(\omega) = \frac{e^2}{\hbar} \text{Tr}[\mathbf{W}^{II} \rho_{\text{st}} + \mathbf{W}^I [\Pi_0^{-1}(\omega) - \mathbf{W}]^{-1} \mathbf{W}^I \rho_{\text{st}}] - 2\pi\delta(\omega) \langle \hat{I} \rangle^2 + (\omega \rightarrow -\omega) \quad (5.11)$$

where  $\mathbf{W}^I \equiv \mathbf{W}_{>}^I(\omega = 0) = \mathbf{W}_{<}^I(\omega = 0)$ ,  $\mathbf{W} \equiv \mathbf{W}(\omega = 0)$ , and  $\mathbf{W}^{II} \equiv \mathbf{W}^{II}(\omega = 0)$ . This means, that the bosonic frequency lines  $\omega$  in the diagrams as shown in Fig. 5.7 can be neglected. The only remaining frequency-dependent part is the free propagator  $\Pi_0(\omega)$ .

This formalism, of course, reproduces the noise spectrum of a single-level quantum dot connected to normal leads as known from literature [85]. If the dot levels are away from the Fermi edges of the leads, such that one can approximate the Fermi functions by one or zero only, the Fano factor shows a Lorentzian dependence on the noise frequency  $\omega$

$$F(\omega) \equiv \frac{S(\omega)}{2eI} = \frac{1}{2} \left[ 1 + \frac{(2\Gamma_L - \Gamma_R)^2}{(2\Gamma_L + \Gamma_R)^2 + (\hbar\omega)^2} \right] \quad (5.12)$$

for a bias voltage allowing only an empty or singly occupied dot, and

$$F(\omega) = \frac{1}{2} \left[ 1 + \frac{(\Gamma_L - \Gamma_R)^2}{(\Gamma_L + \Gamma_R)^2 + (\hbar\omega)^2} \right] \quad (5.13)$$

for higher bias voltages, when double occupation is also allowed.

### 5.2.5 Technical summary

The technical scheme for calculating the zero- and low-frequency current noise is the following: First, the objects  $\mathbf{W}$ ,  $\mathbf{W}^I$ , and  $\mathbf{W}^{II}$  must be calculated in the  $\omega = 0$  limit, using the diagrammatic approach, see Appendix B.

In the next step, the reduced density matrix  $\rho_{\text{st}}$  can be calculated. For technical reasons it is convenient to express the density matrix as introduced in Eq. (2.5) as a vector:  $\rho_{\text{st}} = (P_0^0, P_\uparrow^\uparrow, P_\downarrow^\downarrow, P_d^d, P_\downarrow^\uparrow, P_\uparrow^\downarrow)^T$ . Then the fourth-order tensors  $\mathbf{W}$ 's and  $\mathbf{\Pi}(\omega)$  are only  $6 \times 6$  matrices, see Appendix B, and standard computer implemented matrix operations can be used. It is worth pointing out that in the vector notation, the trace for example in Eq. (5.11) is then *not* the sum of all elements of the resulting vector as assumed by Ref. [101], but only the sum of the first four entries. These elements correspond to the diagonal entries of the final density matrix. In the notation of Ref. [92], this can be achieved by the vector  $e^T = (1, 1, 1, 1, 0, 0)$ .

The stationary density matrix follows from the master Eq. (5.5)  $0 = -i(\varepsilon_\chi - \varepsilon_\eta)(\rho_{\text{st}})_\eta^\chi + \sum_{\chi_1, \eta_1} W_{\eta\eta_1}^{\chi\chi_1}(\rho_{\text{st}})_{\eta_1}^{\chi_1}$  under the constraint of probability normalization  $e^T \cdot \rho_{\text{st}} = 1$ . The average *dc*-current through the system is given by  $I = e/(2\hbar)e^T \cdot \mathbf{W}^I \cdot \rho_{\text{st}}$ . In the low-frequency limit the frequency-dependent propagator  $\mathbf{\Pi}(\omega)$  can be constructed from the frequency-dependent free propagator  $\mathbf{\Pi}_0(\omega)$  and the frequency-*independent* self-energy  $\mathbf{W}(\omega = 0)$ . The low-frequency noise is then given by the matrix multiplication  $S(\omega) = e^2/(2\hbar)e^T \cdot (\mathbf{W}^{II} + \mathbf{W}^I \mathbf{\Pi}(\omega) \mathbf{W}^I) \cdot \rho_{\text{st}} + (\omega \rightarrow -\omega)$ , where the  $i0^+$  in the denominator of the propagator is already dropped, since the term arising from the  $i0^+$  contribution cancels the delta function in Eq. (5.10).

### 5.3 Results

In this Section, the results for zero- and finite-frequency current noise in a quantum dot connected to ferromagnetic leads with non-collinear magnetizations are discussed. The relative energies of a single-level dot is sketched in Fig. 5.8.

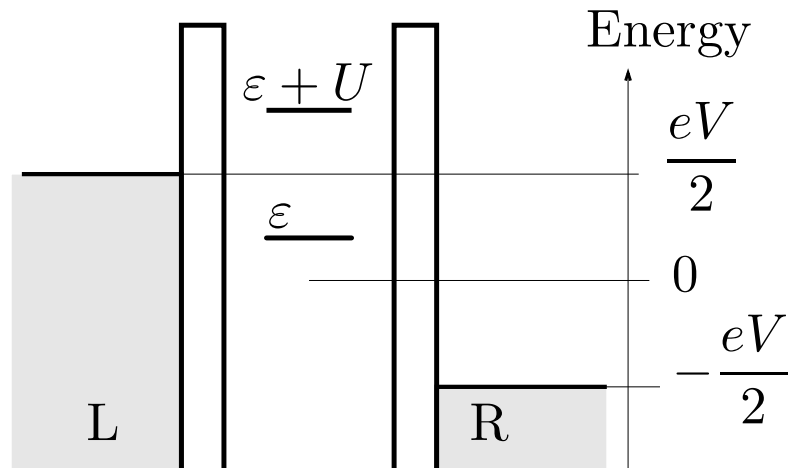


Figure 5.8: Sketch of different energies involved. Since we assume equal tunnel-interface capacities, the voltage drop on the left and right side is symmetric.

By assuming  $k_B T \gg \Gamma$ , and that the single-particle state is above the equilibrium Fermi energy of the leads, higher-order tunnel processes [38, 88, 115, 117] can be neglected.

### 5.3.1 Zero-frequency noise

In Fig. 5.9, we plot the results for  $F(\omega \rightarrow 0) = S(\omega \rightarrow 0)/(2eI)$ , i.e., the zero-frequency Fano factor for the quantum dot contacted by ferromagnetic leads. In Fig. 5.9(a), the leads are aligned *parallel*. For  $eV/2 < \varepsilon$ , when the dot level is above the lead Fermi energies, the dot is predominantly empty, and interaction effects are negligible leading to a Fano factor of unity. In the voltage window  $\varepsilon < eV/2 < \varepsilon + U$ , when the dot can only be empty or singly occupied, one can observe super-Poissonian noise due to dynamical spin blockade [28, 88, 94, 109] for sufficiently high lead polarization. The minority spins have a much longer dwell time inside the dot than the majority spins. In this way, they effectively chop the current leading to bunches of majority spins. While the current in this regime  $I = 2\Gamma_L\Gamma_R/(2\Gamma_L + \Gamma_R)$  does not depend on the polarization  $p$  of the leads, the Fano factor

$$F(0) = \frac{4\frac{1+p^2}{1-p^2}\Gamma_L^2 + \Gamma_R^2}{(2\Gamma_L + \Gamma_R)^2} \quad (5.14)$$

even diverges for  $p \rightarrow 1$ . If the voltage exceeds the value necessary to occupy the dot with two electrons ( $eV/2 > \varepsilon + U$ ), the noise is no longer sensitive to the lead polarizations.

Also in the case of *anti-parallel* aligned leads, the Fano factor rises in the voltage regime  $\varepsilon < eV/2 < \varepsilon + U$  as seen in Fig. 5.9(b). The dot is primarily occupied with an electron with majority spin of the source lead, i.e., minority spin for the drain lead, since this spin has the longest dwell time. If the electron tunnels to the drain lead, it gets predominantly replaced by a majority spin of the source lead. For a high enough lead polarization, only one spin component becomes important. Further this spin component is strongly coupled to the source lead and weakly coupled to the drain lead, therefore the Fano factor approaches unity.

If the leads are *non-collinearly* aligned, for example if an angle  $\phi = \pi/2$  is enclosed as shown in Fig. 5.9(c), a qualitatively different behavior can be observed. Now, the typical Coulomb plateaus are modulated. This shape arises, since the dot spin starts to precess around the lead magnetizations. The tunnel coupling between the ferromagnetic lead  $r = L/R$  and the dot induces the exchange field contribution

$$\mathbf{B}_r = p \frac{\Gamma_r \hat{\mathbf{n}}_r}{\pi \hbar} \int' d\omega \left( \frac{f_r(\omega)}{\hbar\omega - \varepsilon - U} + \frac{1 - f_r(\omega)}{\hbar\omega - \varepsilon} \right), \quad (5.15)$$

as discussed in Chapter 4. This exchange interaction causes an intrinsic spin precession of the dot spin around the lead magnetizations. This exchange field automatically appears in a rigid calculation of the generalized transition rates  $\mathbf{W}$ .

The intrinsic spin precession due to the exchange field counteracts the dynamical spin blockade. The exchange coupling to one lead is maximal, if its Fermi energy coincides



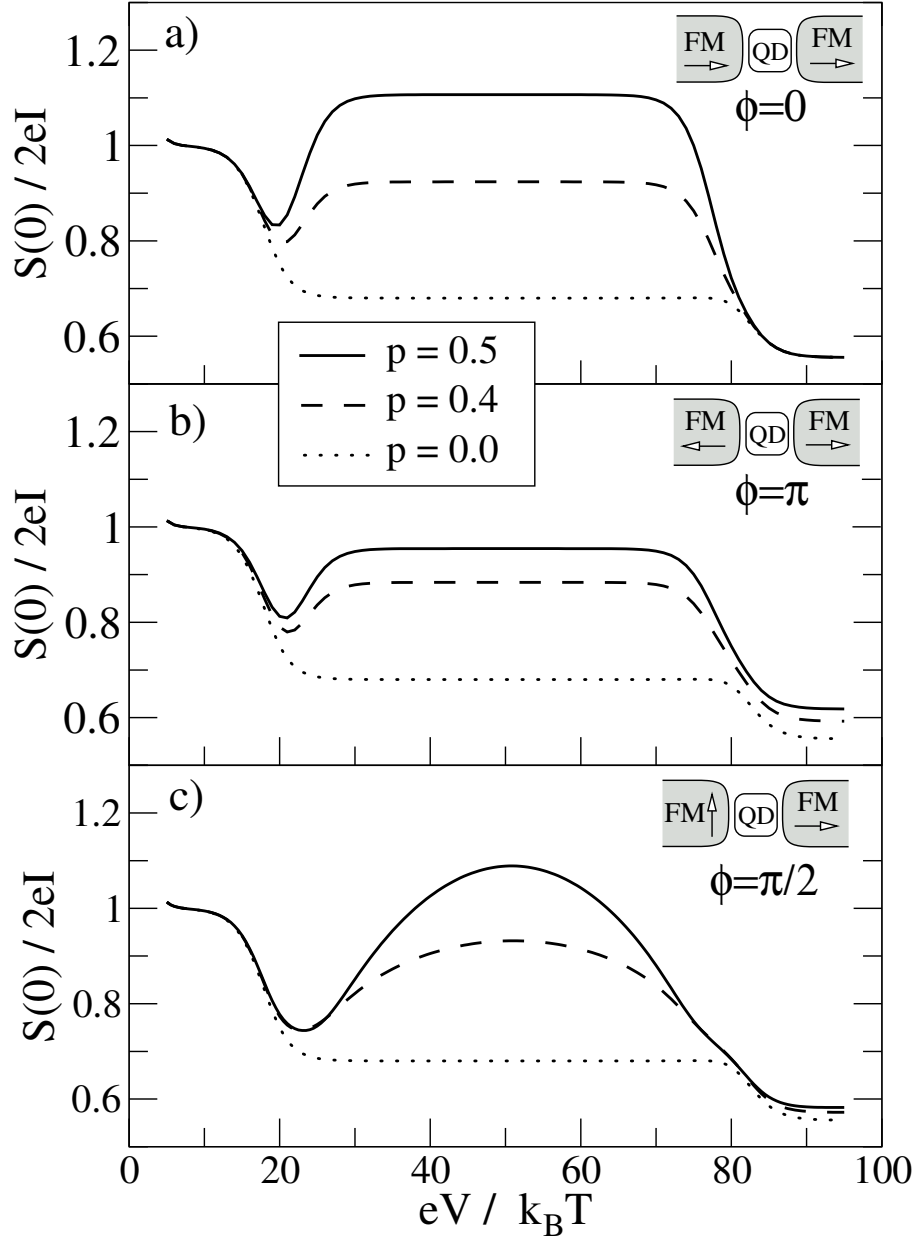


Figure 5.9: Zero-frequency current noise through a quantum-dot spin valve. In panel (a), the lead magnetizations are aligned parallel, in panel (b) anti-parallel, and in panel (c) the lead magnetizations enclose an angle of  $\pi/2$ . The different lines correspond to different values of the lead polarization  $p$ . Other parameters are  $\varepsilon = 10k_B T$ ,  $U = 30k_B T$ , and  $\Gamma_L = 2\Gamma_R$ .

with the dot energy levels. The coupling to the source lead is maximal at the voltages  $eV/2 = \varepsilon$  and  $eV/2 = \varepsilon + U$  and changes its sign in between. Therefore the reduction of the Fano factor is non-monotonic, and so is the variation of the Coulomb plateaus. It is worth pointing out that to observe this spin precession mechanism in the conductance of the device, a relatively high spin polarization of the leads is required. But the noise is much more sensitive to this exchange effect than the conductance, so that a polarization as expected for Fe, Co, or Ni [56] is well sufficient.

The current, the zero-frequency current-current correlation, and the Fano factor are plotted in Fig. 5.10 as function of the angle  $\phi$  between the two lead magnetization vectors. The gray lines are for bias voltage  $eV = 50k_B T$ , where the exchange field influence is weak, the black lines are for the bias voltage  $eV = 30k_B T$ , where the exchange interaction is more pronounced. Since both voltages are within the voltage window allowing only single occupation of the dot, compare Fig. 5.9, the tunnel rates do not change significantly within this voltage range. Only the exchange field does vary with bias voltage. On one hand the precession of the dot spin in the exchange field leads to an increase of the current (compare Chapter 4) in Fig. 5.10(a). On the other hand, the precession suppresses bunching, which decreases the noise, see Fig. 5.10(b). Therefore the spin precession decreases the Fano factor in Fig. 5.10(c).

For  $\phi = 0$  and  $\phi = \pi$  the accumulated spin is collinearly aligned with the exchange field, therefore no spin precession takes place, and the black and gray lines merge.

### 5.3.2 Finite-frequency noise and weak magnetic fields

The  $dc$ -conductance of the quantum-dot spin valve is a direct measure of the time-averaged spin in the dot. On the other side, the power spectrum of the current noise can also measure the time-dependent dynamics of the individual electron spins in the dot. The spin precesses in the exchange field as well as an external magnetic field. This gives rise to a resonance signal in the frequency-dependent noise at the Larmor frequency of the total field.

By including an external magnetic field in the noise calculation, one has to distinguish two different parameter regimes: either the Zeeman splitting  $\Delta \equiv g\mu_B B_{\text{ext}}$  is of the same order of magnitude as the level broadening  $\Delta \approx \Gamma_L, \Gamma_R$ , or it significantly exceeds the tunnel coupling  $\Delta \gg \Gamma_L, \Gamma_R$ . This section focuses on the first case, while the latter case is treated in Section 5.3.3.

By choosing the spin-quantization axis of the dot subsystem parallel to the external magnetic field, the magnetic field only induces a Zeeman splitting of the single-particle level  $\varepsilon$  in  $\varepsilon_{\uparrow} = \varepsilon + \Delta/2$  and  $\varepsilon_{\downarrow} = \varepsilon - \Delta/2$ . Since  $\Delta \approx \Gamma_L, \Gamma_R$ , the  $\mathbf{W}$ 's can also be expanded in  $\Delta$  and only the zeroth-order terms needs to be kept, since each correction of the self-energies would be proportional to  $\Delta \cdot \Gamma \approx \Gamma^2$ . The Zeeman splitting must only be

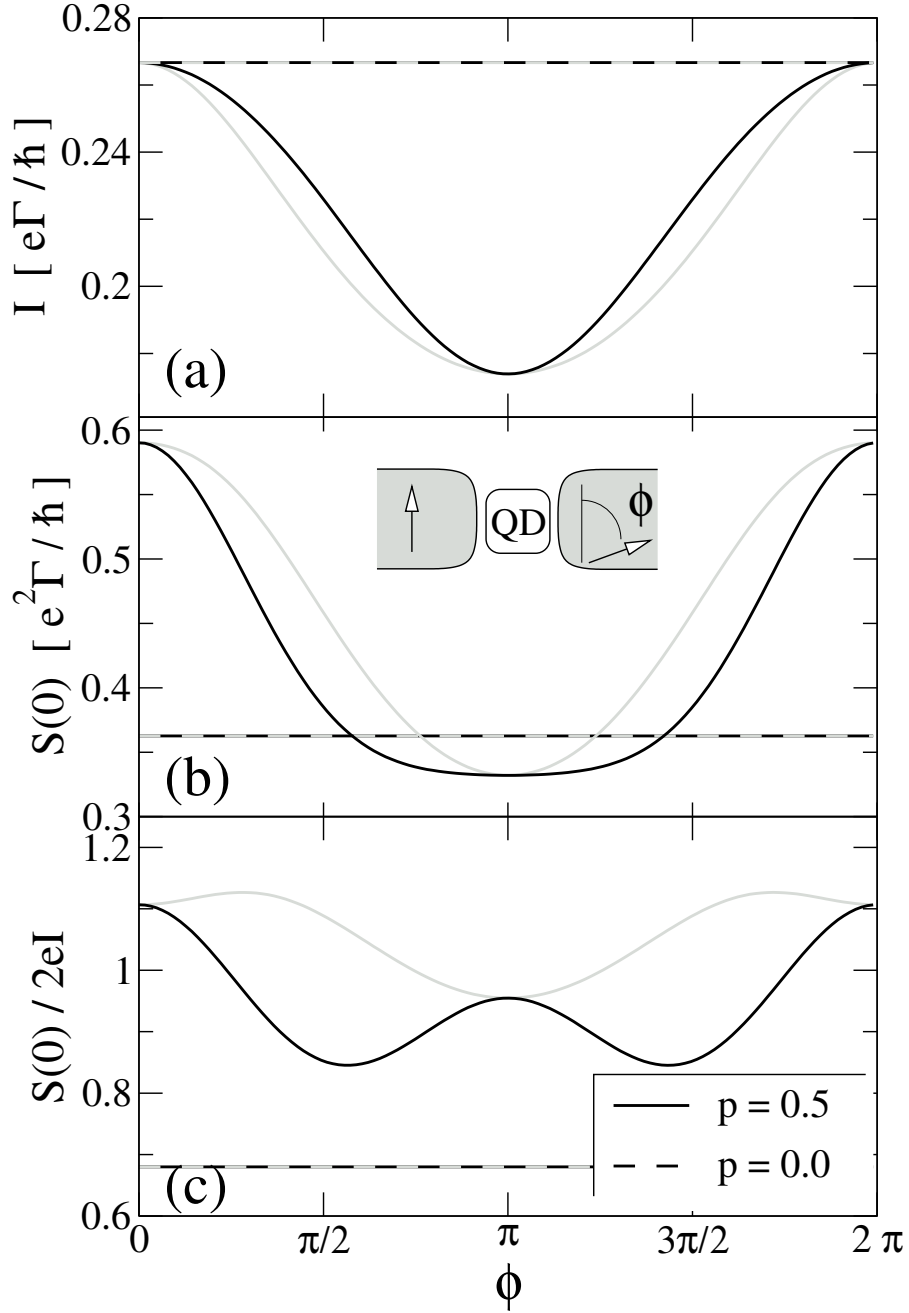


Figure 5.10: Current (a), current noise (b), and Fano factor (c) of a quantum-dot spin valve as a function of the angle  $\phi$ , enclosed by the lead magnetizations. The gray lines are for a bias voltage  $eV = 50k_B T$ , where the exchange field influence is weak, while the black curves are for  $eV = 30k_B T$ , where the exchange field is more pronounced. Further parameters are  $\varepsilon = 10k_B T$ ,  $U = 30k_B T$ , and  $\Gamma_L = 2\Gamma_R$ .

considered for the free propagator. With Eq. (5.4), the propagator is then given by

$$\mathbf{\Pi}_0(\omega) = \begin{pmatrix} \frac{i}{\hbar\omega+i0^+} & 0 & 0 & 0 & 0 & 0 \\ 0 & \frac{i}{\hbar\omega+i0^+} & 0 & 0 & 0 & 0 \\ 0 & 0 & \frac{i}{\hbar\omega+i0^+} & 0 & 0 & 0 \\ 0 & 0 & 0 & \frac{i}{\hbar\omega+i0^+} & 0 & 0 \\ 0 & 0 & 0 & 0 & \frac{i}{\hbar\omega+\Delta+i0^+} & 0 \\ 0 & 0 & 0 & 0 & 0 & \frac{i}{\hbar\omega-\Delta+i0^+} \end{pmatrix}, \quad (5.16)$$

where the matrix notation as introduced in Section 5.2.5 is used. The two last rows of this matrix govern the time evolution of  $\rho_{\uparrow}^{\downarrow}$  and  $\rho_{\downarrow}^{\uparrow}$ , representing the spin components transverse to the quantization axis, i.e., transverse to the applied magnetic field. The change of the denominator by the Zeeman energy  $\Delta$  describes just the precession movement of the transverse spin component. Since the free propagator  $\mathbf{\Pi}_0(\omega)$  is a function of  $\Delta$ , the Zeeman energy modifies the full propagator  $\mathbf{\Pi}(\omega)$  as well as the (zeroth-order) stationary density matrix  $\boldsymbol{\rho}_{\text{st}}$ , via the master Eq. (5.5).

The numerical results are plotted in Fig. 5.11 – Fig. 5.13. In Fig. 5.11 the magnetizations of the leads are aligned parallel, and a magnetic field is applied perpendicular to the lead magnetizations. With parallel-aligned leads and equal polarizations in both leads, no average spin accumulates on the dot, and therefore the current-voltage characteristic as shown in the inset of Fig. 5.11, shows neither magnetoresistance nor the Hanle effect (compare Chapter 4) if a transverse magnetic field is applied. In contrast to the conductance, which depends on the average dot spin only, the frequency-dependent noise is sensitive to the time-dependent dynamics of the spin on the dot. Therefore, the field-induced spin precession is visible in the noise power spectrum. For  $B = 0$  the Fano factor shows a Lorentzian dependence of the noise frequency. Thereby the Fano factor exceeds unity due to the bunching effect, as discussed in Section 5.3.1. With increasing magnetic field, spin precession lifts the dynamical spin blockade inside the dot, and the Fano factor decreases at  $\omega \approx 0$ .

Furthermore the precession of the electron spins inside the quantum dot gives rise to a resonance line approximatively at the Larmor frequency of the applied magnetic field. Due to tunnel-magnetoresistance effects, the precession of the dot spin modulates the effective tunnel rates, which modify the current-current correlation function at the frequency of the precession. Therefore the field-induced spin precession is visible as resonance line in the current noise power spectrum.

The appearing resonance line can be characterized by linewidth, line form, and position. The linewidth of the resonance is given by the damping due to tunnel events and is of order  $\Gamma$ . The line shape depends on the relative alignment of the lead magnetizations and the applied magnetic field. It can resemble an absorption or dispersion line shape, but especially in the low-frequency regime  $\omega < \Gamma$ , the Lorentzian background related to the zero frequency noise contributions, and the rather complicated spin dynamics lead to a strong deformation of the line. In Fig. 5.12, the noise resonance is plotted for different

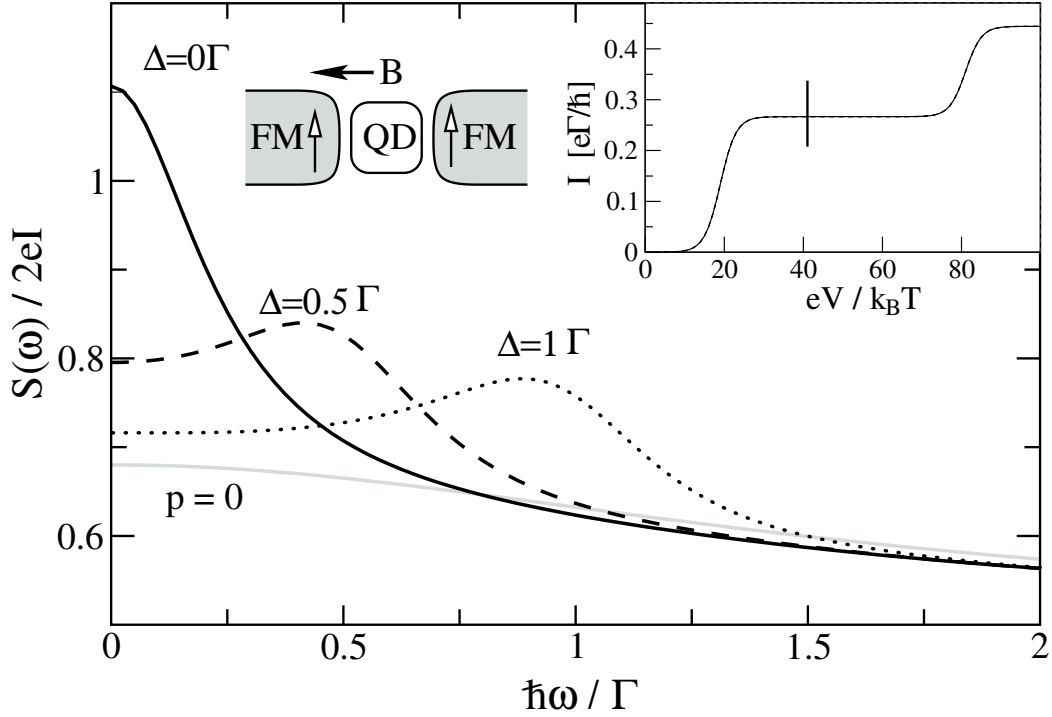


Figure 5.11: Frequency-dependent Fano factor of a quantum dot connected to parallel aligned leads with perpendicular applied external magnetic field. The parameters are  $p = 0.5$ ,  $\varepsilon = 10k_B T$ ,  $U = 30k_B T$ ,  $eV = 40k_B T$ , and  $\Gamma_L = 2\Gamma_R$ . The inset shows the current bias-voltage characteristic, which does not depend on the applied magnetic field.

opening angles of the lead magnetizations, while the magnetic field is applied perpendicular to both magnetizations. In this situation, the diversity of possible line shapes is especially pronounced. We will revisit the mechanism leading to the different line shapes in Sec. 5.3.3. In the limit of strong magnetic fields, and therefore at high frequencies, the discussion gets much more transparent.

Due to the deformation of the line shape at low frequencies ( $\omega < \Gamma$ ), the absolute position of the resonance line is hard to detect, compare Fig. 5.12. But beside this technical aspect, there exist also a physical mechanism for a deviation of the resonance line position from the Larmor frequency, one would expect by considering the applied magnetic field only: the exchange interaction between ferromagnetic leads and dot spin. The spin inside the dot precesses in the total field containing the external magnetic field and the exchange field, see Eq. (5.15). Depending on the relative orientation of lead magnetizations and applied magnetic field, the exchange field can increase or decrease the total field strength.

To emphasize the influence of the exchange field on the resonance position, we plot the finite frequency noise in Fig. 5.13 for different bias voltages. Thereby the lead magnetizations enclose an angle  $\phi = \pi/2$ , and an external magnetic field is applied parallel to

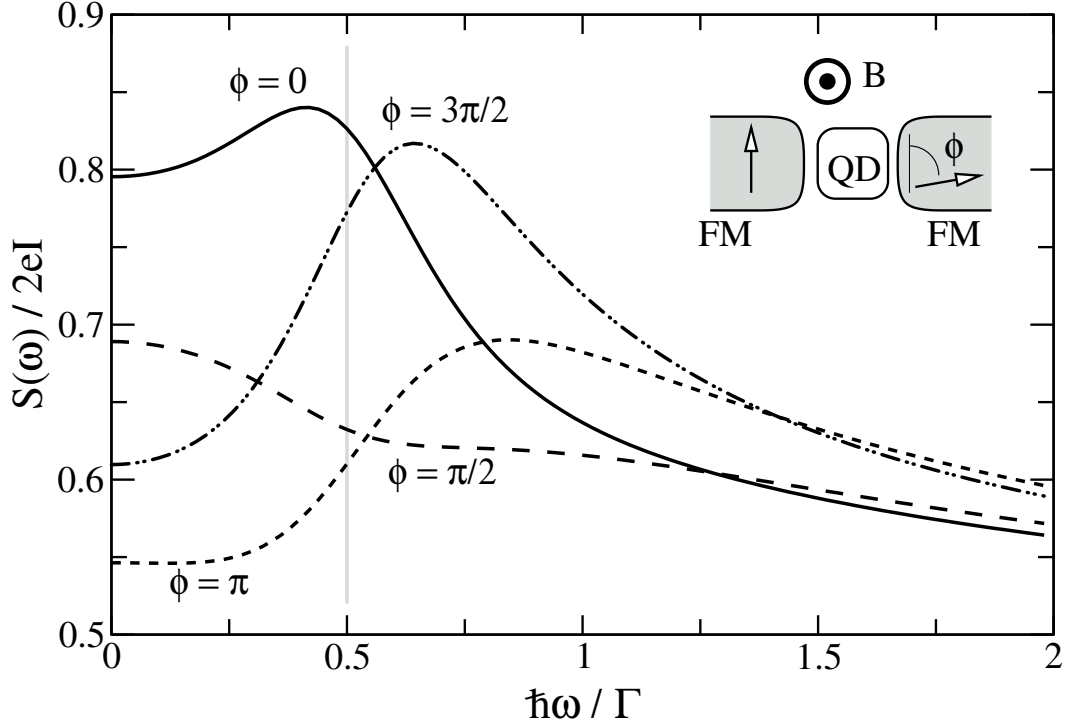


Figure 5.12: Fano factor of a quantum-dot spin valve as a function of the noise frequency. An external magnetic field  $g\mu_B B_{\text{ext}} = \Delta = \Gamma/2$  is applied perpendicularly to both lead magnetizations. The lead magnetizations enclose the angle  $\phi = 0$  (solid),  $\phi = \pi/2$  (dashed),  $\phi = \pi$  (dotted), and  $\phi = 3\pi/2$  (dot-dot-dashed). The vertical gray line marks the Larmor frequency given by the external magnetic field only. Other system parameters are as in Fig. 5.11.

the source lead magnetization. The different considered bias voltages belong to the same current plateau, as indicated in the inset of Fig. 5.13. This means that the transition rates do not change significantly within this voltage window. Still the resonance position shifts with bias voltage, since the exchange field and, therefore, the total field depends on bias voltage.

In the lead and field configuration discussed in Fig. 5.13, the exchange field is more effective in shifting the resonance, compared to the previous plots, since the contribution from the source lead directly adds a contribution parallel to  $\mathbf{B}_{\text{ext}}$ . In Fig. 5.11 and Fig. 5.12, the exchange field contributions are always aligned perpendicular to the external field, which weakens the influence of the exchange interaction.

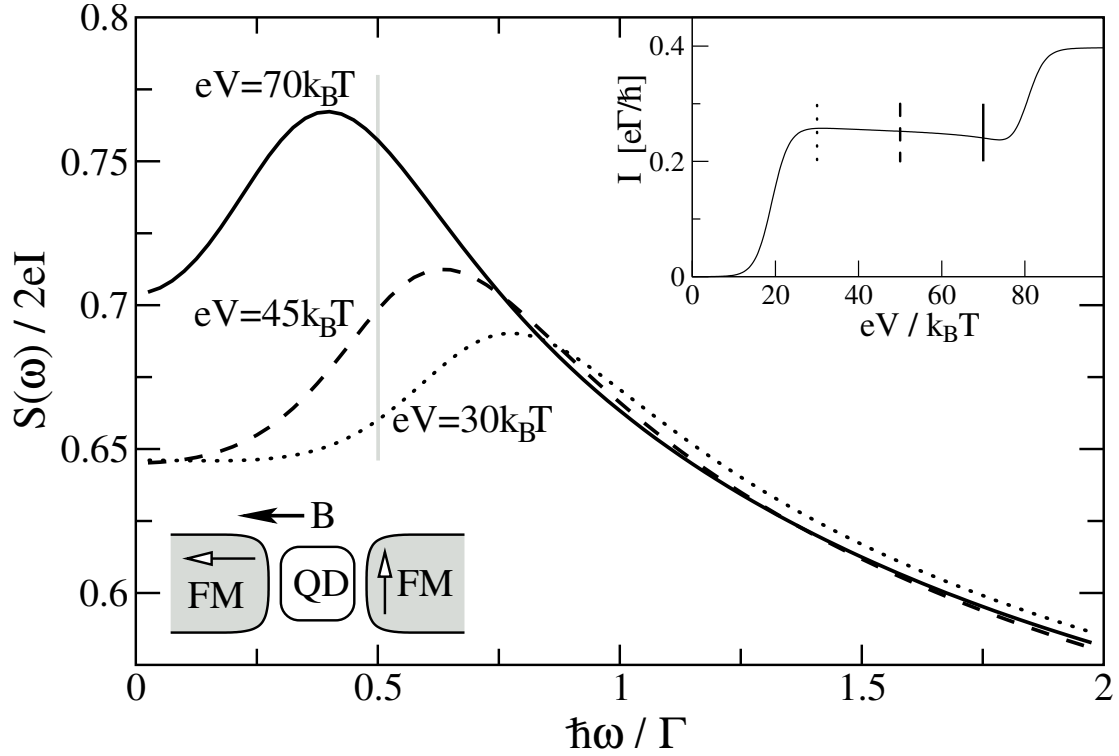


Figure 5.13: Frequency-dependent Fano factor, when the lead magnetizations enclose an angle  $\phi = \pi/2$  and an external magnetic field  $g\mu_B B_{\text{ext}} = 1/2\Gamma$  is applied parallel to the source lead magnetization. The vertical gray line again marks the Larmor frequency given by the external magnetic field only. For the three different bias voltages,  $eV = 30k_B T$  (dotted),  $eV = 45k_B T$  (dashed) and  $eV = 70k_B T$  (solid), the strength of the exchange field varies, and so does the position of the resonance peak. Other system parameters are as in Fig. 5.11.

### 5.3.3 Limit of strong magnetic fields

The current-current correlation function  $S(\omega)$  is a measure of the average over two current measurements with a relative time difference of multiples of  $1/\omega$ . On the other side, the time between two tunnel events is given by the inverse of the tunnel coupling strength  $\Gamma$ . Therefore, the condition  $\omega \ll \Gamma$  and  $\omega \gg \Gamma$  define physical different parameter regimes. If  $\omega \ll \Gamma$ , which defines the zero-frequency regime, on average several tunnel events place between the two current measurements. Therefore, the noise will reflect mainly the behavior of average properties, which for example causes to bunching. In the other regime, when  $\omega \gg \Gamma$ , the noise will mostly reflect the correlation between two sequencing tunnel events.

To illustrate this point, we discuss in this Section the case of an applied magnetic field, where the Zeeman energy  $\Delta \equiv g\mu_B B_{\text{ext}} \gg \Gamma_L, \Gamma_R$  exceeds the tunnel coupling strength. Then, the interesting signal in the noise spectrum will be at the frequency  $\omega \approx \Delta \gg$

$\Gamma$ . As a simplification, we still consider the  $\mathbf{W}$ 's as independent of  $\Delta$  as well as of  $\hbar\omega$ . This assumption is justified, as long as the distance between the quantum-dot states and lead Fermi surfaces well exceeds temperature  $k_B T$ , the Zeeman splitting  $\Delta$ , and the noise frequency  $\hbar\omega$ .

For a clear analytic expression, the stationary density matrix is expanded in zeroth order in  $\Gamma/\Delta$ , and only the noise frequency range  $\omega = \Delta \pm \Gamma$  is consider. In this regime the first five diagonal entries of the free propagator in Eq. (5.16) can be treated as zeroth order in  $\Gamma$ , i.e., their contribution drops out for the lowest-order noise, and only the last entry  $1/(\omega - \Delta) \approx 1/\Gamma$  is kept. This considerably simplifies the calculation, since all bunching effects and the exchange field components perpendicular to the external field can be neglected.

Let us consider a single-level quantum dot with such an applied voltage, that we can approximate the Fermi functions by  $f_L(\varepsilon) = 1$  and  $f_L(\varepsilon + U) = f_R(\varepsilon) = f_R(\varepsilon + U) = 0$ . This applied bias voltage allows only an empty or singly-occupied dot. For an external applied magnetic field perpendicular to both lead magnetizations  $\mathbf{B}_{\text{ext}} \perp \hat{\mathbf{n}}_L, \hat{\mathbf{n}}_R$  the Fano factor

$$F(\omega) = \frac{1}{2} + \frac{p^2}{4} \frac{\Gamma_R^2 \cos \phi + \Gamma_R(\hbar\omega - \Delta) \sin \phi}{\Gamma_R^2 + (\hbar\omega - \Delta)^2} \quad (5.17)$$

shows a resonance signal at the Larmor frequency  $\hbar\omega = \Delta$ . Depending on the angle  $\phi$ , enclosed by the two lead magnetization directions, the resonance line has the character of an absorption or dispersion line, see Fig. 5.14.

By shifting the gate voltage such that  $f_L(\varepsilon) = f_L(\varepsilon + U) = f_R(\varepsilon) = 1$  and  $f_R(\varepsilon + U) = 0$ , the dot will always be at least occupied by one electron. Then the noise shows the same resonance, only  $\Gamma_R$  and  $\phi$  must be replaced by  $\Gamma_L$  and  $-\phi$ .

If the leads are aligned parallel, the electron will leave the dot primary directly after the tunnel-in event, or after one revolution. In this case, the decay is modulated with a cosine function. If the leads are aligned perpendicular to each other, then the electron must be rotated by the angle  $\pi/2$  (or  $3\pi/2$ ) before the maximum probability for the tunneling-out event is reached. The decay is then modulated by a (minus) sine function. This phase shift determines the lineform of the noise resonance.

The origin of the resonance is the correlation in time between the tunnel-in event, and the tunnel-out event:  $\langle I_L(0)I_R(t) \rangle$ . We can understand the appearance of the resonance, within the following (simplified) picture. Consider that at  $t = 0$  an electron tunnels from the source (left) lead into the dot. Thereby the spin of the incoming electron is polarized along the source lead magnetization.

Due to the finite applied bias voltage, the electron can only decay to the drain (right) lead. The rate of this decay depends via tunnel magnetoresistance on the alignment of the electron spin and the drain lead magnetization. The tunnel-out event is more likely, if the spin is aligned parallel to the lead magnetization than if it is aligned anti-parallel. In the



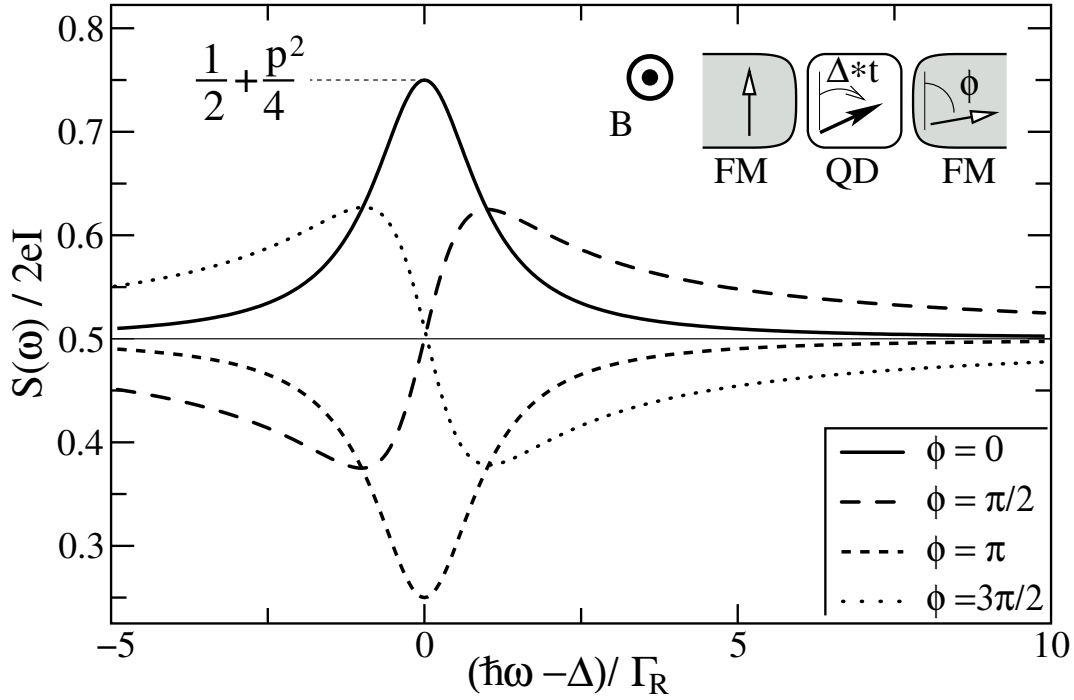


Figure 5.14: Fano factor as a function of noise frequency, for different angles  $\phi$ . The applied voltage does allow only a single occupation of the dot. Other system parameters are as in Fig. 5.13.

applied magnetic field the spin precesses with the Larmor frequency  $\Delta$ . This precession leads to the oscillating modulation  $[1 + p \cos(\Delta t / \hbar - \phi)]$  of the tunnel rate. The phase  $\phi$  of this modulation equals the relative angle of the lead magnetizations.

We guess, that the probability  $P(t)$  to find the electron still on the dot after a tunnel-in event took place at  $t = 0$  is given by the differential equation

$$\frac{dP(t)}{dt} = -\frac{\Gamma_R}{\hbar} [1 + p \cos(\frac{\Delta}{\hbar}t - \phi)] P(t), \quad (5.18)$$

with the boundary condition  $P(t = 0) = 1$ . By solving this linear differential equation, the probability as function of time equals

$$P(t) = A \cdot \exp(-\frac{\Gamma_R}{\hbar}t) \cdot \exp[-\frac{\Gamma_R}{\Delta}p \sin(\frac{\Delta}{\hbar}t - \phi)], \quad (5.19)$$

with the normalization constant  $A = \exp[-\Gamma_R \sin(\phi)/\Delta]$ . The current  $I_R(t)$  through the drain interface is proportional to the time derivative of the occupation probability, see Eq. (5.18). If we expand the gained expression in zeroth order in  $\Gamma_R/\Delta$ , we get

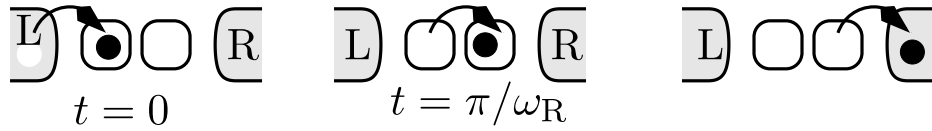
$$I_R(t) \propto -\frac{\Gamma_R}{\hbar} [1 + p \cos(\frac{\Delta}{\hbar}t - \phi)] \exp(-\frac{\Gamma_R}{\hbar}t). \quad (5.20)$$

The current-current correlation function in Eq. (5.17) is then just trivially related to the Fourier transformation of this time-dependent current. This is quite remarkable as Eq. (5.17) is the result of a rigid calculation, while Eq. (5.18) is the outcome of phenomenological considerations.

At this point, we can understand the approximation of high field/frequency. In Eq. (5.19) we derived the decay of the occupation probability. Due to the oscillating part of the tunnel rate, the decay is rather complicated. But since the time scale of the decay ( $\propto \Gamma_R$ ) is slow compared to the oscillation frequency, we can average the decay rate over an oscillation period, which is equivalent to neglecting the terms proportional to  $\Gamma_R/\Delta$ . Within this approximation, the decay of the occupation probability in time is then just exponential. In the low-frequency range  $\Delta \approx \Gamma_R$ , as discussed in Sec. 5.3.2, the non-trivial decay yields a more complicated resonance line in the current-current correlation function.

The phase dependence of the noise resonance as shown in Fig. 5.14 is also predicted for a double-dot system [100, 101, 105]. Let us consider two dots connected in series, see Fig. 5.15A), and an electron from the left (source) electrode enters the left dot. Since this is not an eigenstate of the isolated double-dot system, the electron coherently oscillates between the two dots with the frequency  $\omega_R$ . After the time  $t = \pi/\omega_R$ , the electron is in the right dot and can tunnel to the drain lead. This corresponds to the  $\phi = \pi$  case resulting in a dip in the noise. The realization of the  $\phi = 0$  case would be a double dot where the left (source) and right (drain) lead is contacted to the same dot, see Fig. 5.15B). Here the electron must stay a multiple of  $2\pi/\omega_R$  inside the double dot to tunnel to the drain lead, giving a peak in the frequency noise spectrum. Other values of  $\phi$  have no double-dot system analog.

A.)  $\phi = \pi$



B.)  $\phi = 0$

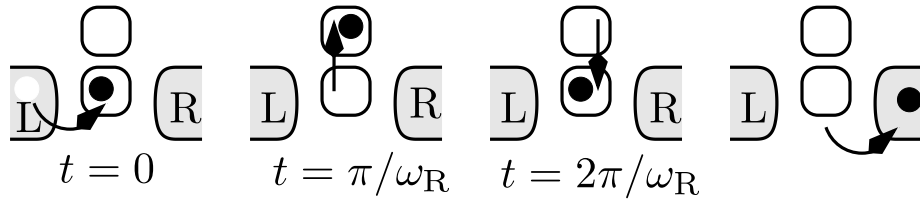


Figure 5.15: The double-dot analog for the decay phase shift  $\phi = 0$  and  $\phi = \pi$  of the electrons.

### 5.3.4 Influence of spin relaxation

The density matrix approach offers a way to phenomenologically include spin relaxation by supplementing the matrix  $\mathbf{W}$  by

$$\mathbf{W}' = \mathbf{W} + \hbar \begin{pmatrix} 0 & 0 & 0 & 0 & 0 & 0 \\ 0 & -\frac{1}{2T_1} & +\frac{1}{2T_1} & 0 & 0 & 0 \\ 0 & +\frac{1}{2T_1} & -\frac{1}{2T_1} & 0 & 0 & 0 \\ 0 & 0 & 0 & 0 & 0 & 0 \\ 0 & 0 & 0 & 0 & -\frac{1}{T_2} & 0 \\ 0 & 0 & 0 & 0 & 0 & -\frac{1}{T_2} \end{pmatrix}. \quad (5.21)$$

The entries in the lower right corner of Eq. (5.21) describe the exponential decay of the transverse spin components on the time scale  $T_2$ , and the block in the upper left corner describes an equilibration of the occupation probability for spin up and down. If one defines the average spin vector on the quantum dot by  $\mathbf{S} = (P_{\downarrow}^{\uparrow} + P_{\uparrow}^{\downarrow}, iP_{\downarrow}^{\uparrow} - iP_{\uparrow}^{\downarrow}, P_{\uparrow}^{\uparrow} - P_{\downarrow}^{\downarrow})/2$  the master Eq. (5.5) becomes the Bloch equation as calculated in Chapter 3. The new term in Eq. (5.21) introduces an additional exponential decay term in this Bloch equation. In the limit of weak Zeeman splitting as discussed throughout the paper,  $T_1$  and  $T_2$  become equal, and  $\mathbf{W}'$  includes an isotropic exponential damping of the spin on the dot. Thereby the master equation describing the change of the probability  $\partial_t(P_{\uparrow}^{\uparrow} + P_{\downarrow}^{\downarrow})$  for single occupation is not affected by this relaxation term.

The modified rate matrix  $\mathbf{W}'$  enters the noise calculation via the calculation of the stationary density matrix and via the propagator  $\mathbf{\Pi}(\omega)$ . The numerical solution for the case of parallel aligned lead magnetizations is plotted in Fig. 5.16.

With increasing the spin decoherence, the spin-related effects decrease, which is the expected behavior for spin decoherence. To completely suppress the spin-related effects the spin lifetime must significantly exceed the inverse tunnel coupling, i.e., the spin-related effects are not very fragile against spin decoherence.

Several articles [26, 101, 118] try to model spin relaxation by the Hamiltonian  $H_{\text{rel}} = Rc_{\uparrow}^{\dagger}c_{\downarrow} + R^{\star}c_{\downarrow}^{\dagger}c_{\uparrow}$ , which is from the physical point of view dissatisfying, since it does not describe incoherent relaxation processes but coherent precession in a transverse magnetic field [119]. This ansatz predicts a completely different behavior of the frequency-dependent current noise. Instead of a suppression of all spin-related effects with increasing the parameter  $R$ , as expected for spin relaxation, an external field generates a resonance line. With increasing the field strength, this line just shifts to higher and higher frequencies, but does not vanish.

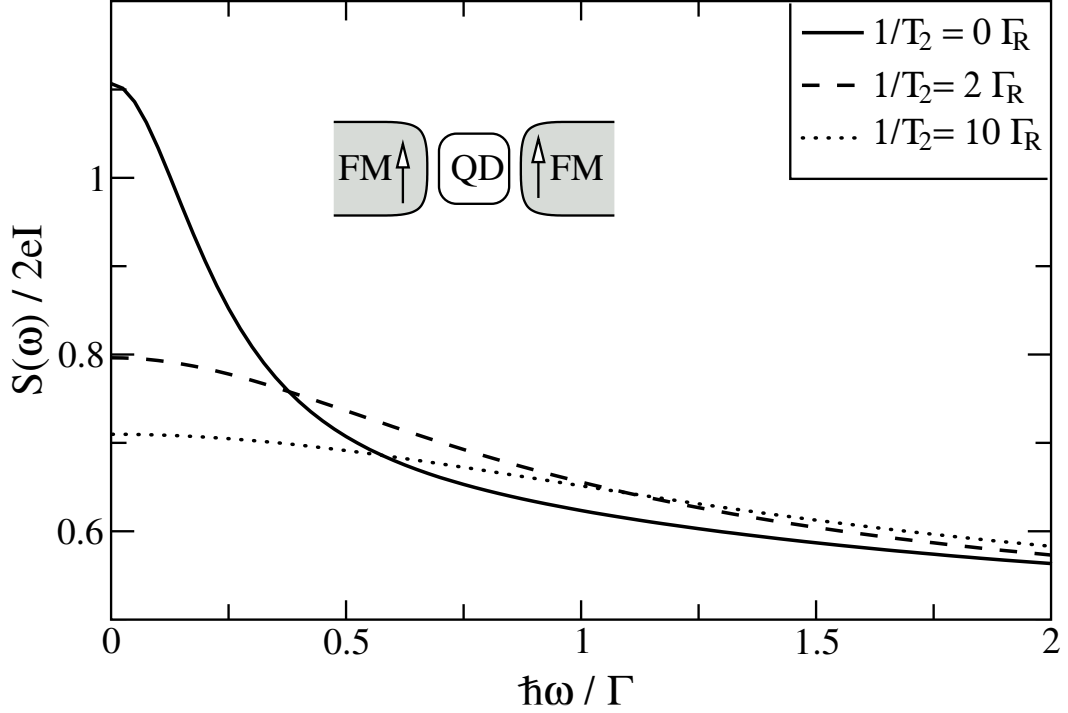


Figure 5.16: Frequency dependence of the Fano factor if the leads are aligned parallel. With increasing spin relaxation, the spin blockade and therefore the bunching effect is reduced. Other system parameters are as in Fig. 5.11.

## 5.4 Chapter summary

By contacting a quantum dot to ferromagnetic leads, the transport characteristic through the device crucially depends on the quantum-dot spin. In the previous Chapters, we examined the influence of the time-averaged dot spin on the *dc*-conductance. In this Chapter the influence of the time-dependent dot-spin precession on the current-current correlation function was discussed. The spin precession of the dot electron spins is caused by the tunnel-induced exchange field and an applied external magnetic field.

In the zero-frequency limit, the spin precession lifts the dynamical spin blockade, and therefore reduces the zero-frequency noise. At the Larmor frequency, corresponding to the sum of exchange and applied fields, the single-spin precession generates a resonance in the frequency-dependent current-current correlation function. Responsible for the resonance is the tunnel-out process of a dot electron to the drain lead. Due to magnetoresistance, the tunnel probability depends on the relative angle of dot spin and drain magnetization. Therefore, the spin precession leads to an oscillation of the tunnel probability, visible in the current-current correlation function. The shape of the resonance in the current-current correlation can either have an absorption or dispersion lineshape, depending on the relative angle between the lead magnetizations.

Finally, a properly inclusion of spin decoherence was shown, and discussed why modeling spin relaxation by an external field transverse to the spin quantization axis, as done sometimes in the literature, is unsatisfying.



## Chapter 6

# Correspondence of a Quantum-Dot Spin Valve to a Double Quantum Dot

Two quantum dots contacted in series seem to be qualitatively different from a quantum-dot spin valve as discussed in the previous Chapters. But since a serial double dot is just another realization of a generic two-level system, such as spin, there exist a close technical as well as physical correspondence between these two systems. Therefore, the predictions made for the quantum-dot spin valve, especially the appearance of an exchange field, can also be tested on double dots. This Chapter contains results acquired in a joined work together with B. Wunsch from the University of Hamburg.

### 6.1 Introduction

A serial double-dot system consists of two individual quantum dots labeled by left (L) and right (R), which are tunnel coupled by the rate  $\Delta$ . Each dot is contacted by a separate lead labeled left (source) and right (drain), see Fig. 6.1.

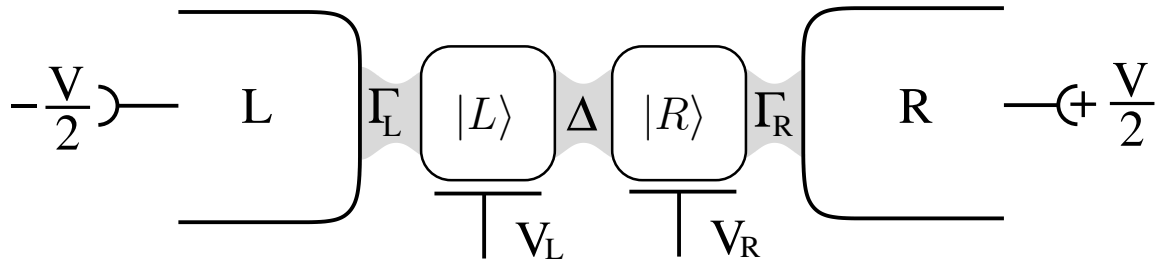


Figure 6.1: Sketch of a double quantum dot in serial bias geometry.

Contacting a quantum dot to ferromagnetic leads, is still an experimentally challenging task, thus the experimental confirmation of the spin dynamics discussed so far will not be trivial. Therefore it would be interesting to test our ideas in double quantum-dot structures, since highly elaborate experimental techniques are available to control and characterize these devices [120–122].

Double quantum-dot systems are so well developed, since they are candidates for realizing charge [123] or spin qubits [124], but also since double dots are ideal systems to investigate various quantum mechanical effects such as molecular binding [125, 126] or coherent dynamics [127] between the constituent dots. Furthermore, many informations about the system can be technically easily deduced from the electric conductance of the device [128]. Recent experiments using double quantum dots include the measurements of quantum mechanical level repulsion due to inter-dot coupling [129] as well as due to external magnetic fields [130], the detection of molecular states in a double-dot dimer [131], and the observation of coherent time evolution of the dot states [127].

## 6.2 Mapping of the double dot on a spin valve

The double-dot problem can be reduced to the spin-valve system with an external applied magnetic field by introducing a pseudo/isospin vector  $\mathbf{I}$ , as often used in the quantum information community [123, 124]. The up/down state of the pseudo spin is given by one electron sitting in the left/right dot of the double well potential.

The topology of the double-dot system can be described by introducing an isospin polarization of the leads. The left lead can be assigned a polarized along the isospin up direction  $\hat{\mathbf{n}}_L = (0, 0, 1)$ , and the right side analog  $\hat{\mathbf{n}}_R = (0, 0, -1)$ . Then, an electron from the left lead will tunnel only in the isospin up state, i.e., to the left dot, and electrons from right lead only to the isospin down state = right dot. In this language, an applied bias voltage yields an isospin accumulation parallel to the  $z$ -axis.

Transport through serial double dots, as depicted in Fig. 6.1 inherently visualizes the basic quantum mechanical concept of coherent superposition of charge states [132]. Due to the inter-dot tunnel amplitude  $\Delta$ , the states  $|L\rangle$  and  $|R\rangle$  localized in the left and right dot, are no energy eigenstates of the double-dot dimer. This yields a coherent oscillation of the electron between the left and the right dot [133–137] as it was shown in recent experiments [123, 127]. In the isospin picture, this coherent time evolution is generated by a magnetic field  $\mathbf{B}_\perp$  applied transverse to the lead (iso-)magnetization directions. Thereby the strength of the perpendicular field equals the inter-dot tunnel amplitude  $\Delta$ .

The atomic-like energy level of the left and right dot is given by  $E_{L/R}$ . An energy level mismatch  $\varepsilon = E_L - E_R$  of the dot levels suppress the coherent oscillation of the electrons in the double-well potential. A more careful analysis shows, that this effect is analogous to a magnetic field  $\mathbf{B}_\parallel$  applied collinear to the lead (iso)magnetizations in a quantum-dot spin valve. In Chapters 3, we predicted, that an exchange field arises due to



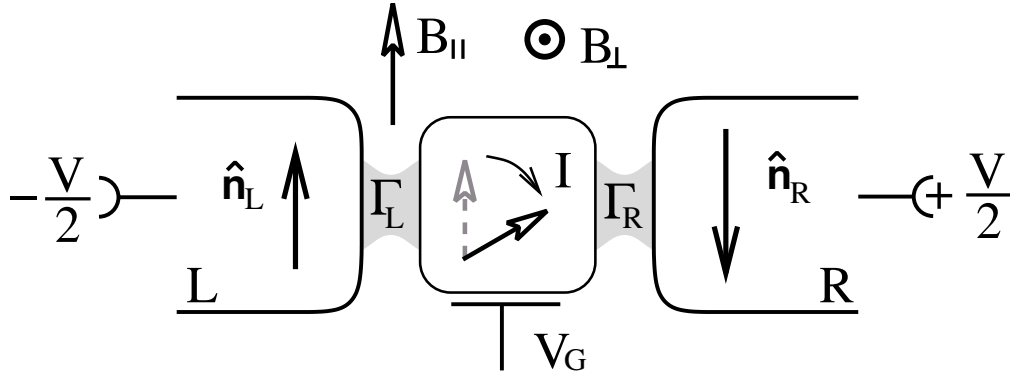


Figure 6.2: Sketch of a double quantum dot in the representation of a spin valve. The isospin state up/down labels the left or right double-dot state. The isospin  $\mathbf{I}$  precesses in the perpendicular magnetic-like field component  $\mathbf{B}_{\perp}$ , describing the coherent oscillations between the left/right dot state, generated by the inter-dot coupling. The detuning of the energy levels in the left and right dot suppresses this oscillation as a magnetic field component  $\mathbf{B}_{||}$  would suppress the spin precession of  $\mathbf{I}$ .

the tunnel coupling to the ferromagnetic leads. This field is collinear aligned to the lead magnetization, therefore it should be just added to the field  $\mathbf{B}_{||}$ . Back in the double-dot picture, this means, that the tunnel coupling of one lead to one dot shifts the energy level of this one dot. Since the left and right dot levels are tunnel coupled to different reservoirs, and the level renormalization is a function of the level energy, the lead chemical potential, and the tunnel coupling, the energy shift of the left and right dot levels is, in general, different, leading to a modification of the level separation energy  $\varepsilon = E_L - E_R$ .

This renormalization of energy levels can be observed in the transport properties of a serial dot system because the conductance through the double dot is very sensitive to the difference of the energy levels. The current passing through the structure as function of the level mismatch shows a resonance at  $\varepsilon = 0$ . The width of the resonance is given by the tunnel couplings [138], which can be much smaller than the temperature. This sharpness of the resonance makes the conductance a valuable experimental tool, for example to measure the shell structure of quantum dots [139].

It is well known [65, 140] that the tunnel coupling to reservoirs renormalizes energy levels. But in single-dot geometries such an energy renormalization is only accessible in transport of higher order in the tunnel coupling strength. In the conductance of a serial double dots, this renormalization effect becomes visible already in the limit of weak dot-lead coupling, described by transport to first order (sequential tunneling) in the tunnel coupling strength  $\Gamma = \Gamma_L + \Gamma_R$ .

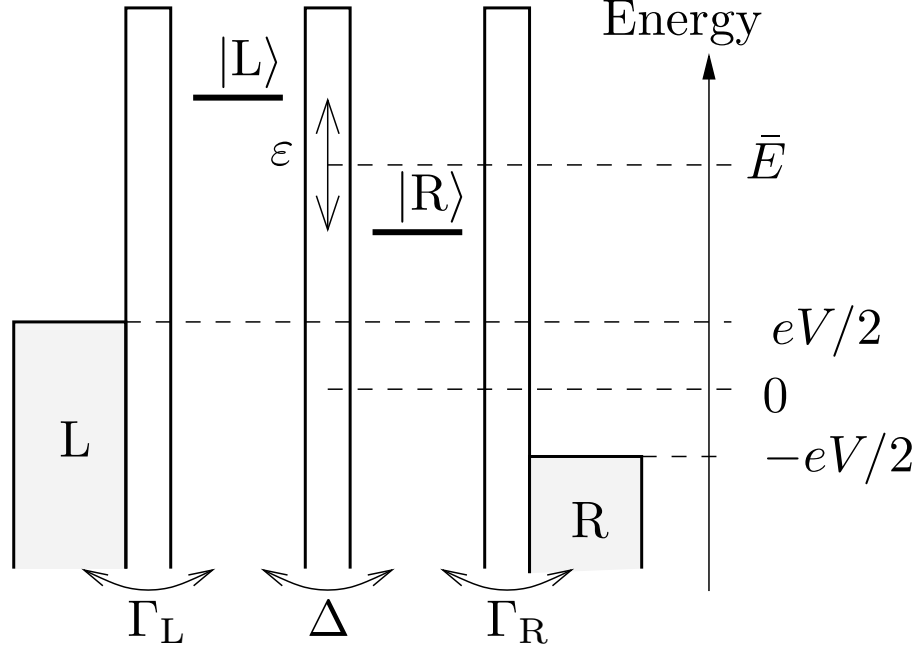


Figure 6.3: Schematic energy profile for a double dot coupled in series to two reservoirs. Each reservoir is coupled to the dot of the corresponding side by the coupling strength  $\Gamma_r$ . The inter-dot coupling is determined by  $\Delta$ . The energies of the two dot states are characterized by the mean energy  $\bar{E}$  and their relative distance  $\varepsilon$ .

### 6.3 Model Hamiltonian

We model the double quantum dot contacted in series by the Hamiltonian [134–137, 141]

$$H = \sum_{r=L,R} H_r + H_{\text{Dots}} + H_T. \quad (6.1)$$

The first part of the Hamiltonian describes the electric contacts on the left (L) and right (R) side. These contacts are large reservoirs of non-interacting electrons modeled by the Hamiltonian  $H_r = \sum_{k,\sigma} \varepsilon_{rk} c_{rk\sigma}^\dagger c_{rk\sigma}$ . Here  $c_{rk\sigma}, c_{rk\sigma}^\dagger$  denote the annihilation and creation operators for electrons in the reservoir  $r \in \{L, R\}$  with spin  $\sigma$ . The reservoirs are assumed to be in equilibrium, that they can be characterized by the Fermi distribution functions  $f_{L/R}(\omega)$ . An applied bias voltage  $V$  is modeled by different chemical potentials in the left and right contact  $f_{L/R}(\omega) = f(\omega \pm eV/2)$ , see Fig. 6.3.

The second part of the Hamiltonian,  $H_{\text{Dots}}$ , describes two dots, containing one electronic level each. We further allow a finite Coulomb interaction between electrons within one dot,

and between the two dots,

$$H_{\text{Dots}} = \sum_{r=L,R} E_r n_r + U n_L n_R + U' (n_{L\uparrow} n_{L\downarrow} + n_{R\uparrow} n_{R\downarrow}). \quad (6.2)$$

Here,  $n_{i\sigma} = d_{i\sigma}^\dagger d_{i\sigma}$  and  $n_i = \sum_{\sigma} d_{i\sigma}^\dagger d_{i\sigma}$  are the occupation-number operators for dot  $i \in \{L, R\}$  with spin  $\sigma$ , where  $d_{i\sigma}, d_{i\sigma}^\dagger$  being the annihilation and creation operators of an electron on dot  $i$  with spin  $\sigma$ . Each dot consists of a single electronic level at the energy  $E_{L/R}$  measured relative to the equilibrium chemical potential of the leads. We parameterize the levels by their average energy  $\bar{E} = (E_L + E_R)/2$  and their difference  $\varepsilon = E_L - E_R$ , so that  $E_{L/R} = \bar{E} \pm \varepsilon/2$ . Double occupation of one individual dot is associated with the intra-dot charging energy  $U'$ . Simultaneous occupation of both dots with one electron each costs the inter-dot charging energy  $U$  with  $U' \gg U$ . States with three or more electrons in the double dot are not considered in the following. The remaining eigenstates of  $H_{\text{Dots}}$ , then, are: both dots empty  $|0\rangle$ , one electron with spin  $\sigma$  in the left  $|L\sigma\rangle$  or right dot  $|R\sigma\rangle$ , and one electron in each dot  $|L\sigma R\sigma'\rangle$ . We assume that the intra-dot charging energy always exceeds the lead Fermi energies. Therefore the states with two electrons in the same dot  $|L\sigma L\bar{\sigma}\rangle$  and  $|R\sigma R\bar{\sigma}\rangle$  will have a vanishing occupation probability. However, these states will appear as intermediate (virtual) states in our calculation, providing a natural high-energy cut-off.

The third part  $H_T = H_\Delta + H_\Gamma$  of the Hamiltonian Eq. (6.1) describes both, tunneling between the two dots,  $H_\Delta$ , as well as tunneling between dots and leads,  $H_\Gamma$ ,

$$H_\Delta = -\frac{\Delta}{2} \sum_{\sigma} \left( d_{L\sigma}^\dagger d_{R\sigma} + d_{R\sigma}^\dagger d_{L\sigma} \right) \quad (6.3)$$

$$H_\Gamma = \sum_{k\sigma} t_{Lk} c_{Lk\sigma}^\dagger d_{L\sigma} + t_{Rk} c_{Rk\sigma}^\dagger d_{R\sigma} + \text{h.c.} \quad (6.4)$$

Due to the serial geometry, an electron from the right (left) reservoir can only tunnel to the right (left) dot. The tunnel coupling of reservoir  $r$  to the corresponding dot is characterized by the coupling strength  $\Gamma_r(\omega) = 2\pi \sum_k |t_{rk}|^2 \delta(\varepsilon_{rk} - \omega)$ . Thereby the coupling strength  $\Gamma$  is defined as an energy, which means, that the average tunnel rate is given by  $\Gamma/\hbar$ . We consider only spin conserving tunneling processes, and assume flat bands in the reservoirs, which yield energy independent couplings  $\Gamma_r$ . Furthermore, the inter-dot tunnel coupling amplitude  $\Delta$  is chosen to be a positive, real parameter, which can be always achieved by a proper gauge transformation.

## 6.4 Kinetic equations

In the following Section the stationary reduced density matrix  $\rho_{\text{st}}$  for the double-dot system and the  $dc$ -current through the system is calculated. The reduced density matrix of the double dot is obtained from the density matrix of the whole system by integrating out the

reservoir degrees of freedom. The Liouville equation for the stationary reduced density matrix then has the structure

$$0 = i\hbar \frac{d}{dt} \rho_{\text{st}} = [H_{\text{Dots}}, \rho_{\text{st}}] + [H_{\Delta}, \rho_{\text{st}}] + i\mathbf{W} \rho_{\text{st}}. \quad (6.5)$$

The first two commutators represent the internal dynamics on the double dot, which depends on the level separation  $\varepsilon$  and the inter-dot coupling  $\Delta$ . The third part of Eq. (6.5) accounts for the tunnel coupling between double dot and external reservoirs. The fourth order tensor  $\mathbf{W}$  contains real and imaginary parts, associated with particle transfer processes (tunnel rates) and with tunnel induced energy renormalization of the dot levels, respectively. The latter has been neglected in previous works [135–137].

In Appendix C.1, the same diagrammatic technique is deployed to determine  $\mathbf{W}$  for the double-dot problem, as used in Appendix B to calculate the generalized rates for the quantum-dot spin valve. The difference between the two problems are the different possible quantum-dot states, and the different allowed transitions between them. Beside the real-time diagrammatic approach [65, 142] also alternative techniques are available such as Bloch-Redfield theory [143, 144].

In the following the limit of weak tunnel coupling between double dot and leads is discussed. Therefore,  $\mathbf{W}$  needs only to be calculated to up to lowest order in the tunnel-coupling strength  $\Gamma = \Gamma_L + \Gamma_R$ , which defines the so-called sequential-tunneling approximation. This approximation implies that all tunneling events are independent from each other. That assumption is correct, as long as co-tunnel events can be neglected, i.e., away from Coulomb blockade regions, and as long as  $k_B T \gg \Gamma$ . Latter restriction arises from the fact, that correlations generated in the bath during a tunnel process decay on the time scale  $\hbar/k_B T$  [145], (this reflects the extension in time of the tunneling line in Fig. C.1 and Fig. C.3), while the average time between consecutive tunneling events is given by the inverse of the coupling strength  $\hbar/\Gamma$ .

The energy eigenstates of the double-dot subsystem  $H_{\text{Dots}} + H_{\Delta}$  are the bonding and anti-bonding states with energies  $E_{b/a} = \bar{E} \mp \Delta_{ab}$  where  $\Delta_{ab} = \sqrt{\Delta^2 + \varepsilon^2}$  denotes their energy splitting. This identifies  $\Delta_{ab}$  as frequency of the charge oscillations [123, 127], and  $\Delta$  as minimum distance between the bonding and anti-bonding eigenstates as function of the left and right energy level [129]. If the splitting exceeds the intrinsic broadening of the levels,  $\Delta_{ab} \gg \Gamma$ , then the internal oscillations are fast, and transport through the double-dot system takes place through two separate incoherent levels. In this case, off-diagonal matrix elements of the stationary density matrix vanish, which can be seen from the expansion of the Liouville equation in zeroth order in  $\Gamma$  which gives  $0 = i\hbar \frac{d}{dt} P_b^a = \Delta_{ab} P_b^a + O(\Gamma)$ . Here  $P_{\chi_2}^{\chi_1}$  denotes the matrix element  $P_{\chi_2}^{\chi_1} = \langle \chi_1 | \rho_{\text{st}} | \chi_2 \rangle$  of the reduced density matrix.

The more interesting transport regime is in the opposite limit,  $\Delta_{ab} \lesssim \Gamma$ , where the external coupling strongly modifies the internal dynamics, which is captured by the off-diagonal elements of the reduced density matrix [136, 137]. Combined with the validity

condition for sequential tunneling  $\Gamma \ll k_B T$  this implies  $\Delta_{ab} \ll k_B T$ . This implies, that the internal oscillations are slow compared to the decay time scale of the tunnel-induced correlations. As a consequence, instead of the bonding and antibonding states, the localized states  $|L\sigma\rangle$  and  $|R\sigma\rangle$  can be used as eigenstates of the double dot in the calculation of  $\mathbf{W}$ . This choice of basis states facilitates the interpretation of the double-dot dynamics significantly. Technically, the condition  $\Delta_{ab} \lesssim \Gamma \ll k_B T$  means that for a consistent theory, we do not only expand  $\mathbf{W}$  in Eq. (6.5) to first order in  $\Gamma$ , but also *have to* expand it to zeroth order in  $\Delta_{ab}$ . This is accomplished by replacing the energies  $E_{L/R}$  arising in the calculation of  $\mathbf{W}$  by the mean level energy  $\bar{E} = (E_L + E_R)/2$ . (Therefore our formulas only contain the Fermi functions at the average single particle level  $f_r(\bar{E})$ , while energies of the order of the inter-dot tunneling or the level separation are smeared out by temperature). It is worth to point out, that by using the localized states as basis of  $\mathbf{W}$ , one is automatically limited to the regime  $\Delta, \varepsilon \ll k_B T$  [133, 135–137].

The technical details of how to calculate  $\mathbf{W}$  are described in Appendix C.1. The master Eq. (6.5) then must be solved under the constraint of probability normalization  $\text{Tr}[\boldsymbol{\rho}_{\text{st}}] = 1$ . The explicit system of master equations is given in Appendix C.2. The stationary current  $I$  is given by the time derivative of the expectation value of the total number of electrons in either the left or the right lead. For the lowest-order expansion used in the present context, the current can alternatively be written in the form [137]

$$I = -e \frac{i}{\hbar} \langle [H_\Delta, n_L] \rangle = -\frac{e}{\hbar} \Delta \text{Im} \left( \sum_{\sigma} P_{R\sigma}^{L\sigma} \right), \quad (6.6)$$

where  $\text{Im}$  denotes the imaginary part. As interesting side note, by introducing the pseudo spin Bloch vector  $\mathbf{I} = (P_R^L + P_L^R, iP_R^L - iP_L^R, P_L^L - P_R^R)^T/2$ , the current is just proportional to the  $I_y$  component, i.e., the spin component transversal to the lead isospin magnetization directions.

## 6.5 Discussion

The stationary current takes the functional form

$$I = \frac{e}{\hbar} \Delta^2 \frac{A}{B^2 + \varepsilon_{\text{ren}}^2}. \quad (6.7)$$

The numerical factors  $A$  and  $B$  depend only on the tunnel coupling constants  $\Gamma_L$ ,  $\Gamma_R$ , and  $\Delta$  as well as on the Fermi distribution functions  $f_{L/R}(\bar{E})$  and  $f_{L/R}(\bar{E} + U)$  of the left and right lead, but not on the level energy difference  $\varepsilon$ .

The Eq. (6.7) shows the well-known [137, 138] Lorentzian dependence of the current on the energy separation  $\varepsilon_{\text{ren}}$  between left and right dot level. However the energy separation

$$\varepsilon_{\text{ren}} = \varepsilon + \Delta E_L - \Delta E_R \quad (6.8)$$

is affected by the renormalization of the bare localized levels. This is the central statement in this Chapter. The tunnel-induced shift  $\Delta E_r$  of the energy level in dot  $r$  is given by

$$\Delta E_r = \phi_r(\bar{E}) - 2\phi_r(\bar{E} + U) + \phi_r(\bar{E} + U') \quad (6.9)$$

with

$$\phi_r(\omega) = \frac{\Gamma_r}{2\pi} \text{Re} \Psi \left( \frac{1}{2} + i\beta \frac{\omega - \mu_r}{2\pi} \right). \quad (6.10)$$

Here,  $\text{Re}$  denotes the real part,  $\Psi$  is the digamma function, and  $\mu_{L/R} = \pm eV/2$  labels the leads' chemical potentials. It is worth to point out that this energy renormalization is not due to a capacitive but rather due to the tunnel coupling to the reservoirs. Furthermore, it vanishes in the noninteracting case  $U = U' = 0$ . The intra-dot charging energy  $U'$  (which is usually treated as infinite to avoid double occupancy of one dot) serves as a natural cut off for the energy renormalization in Eq. (6.9). This is the reason why the corresponding charge states are allowed as intermediate states  $\chi_5$  in Fig. C.2, while the probability to measure these states equals zero.

To compare the result obtained for the stationary current with previous theoretical works, we approximate the Fermi functions by  $f_L(\bar{E}) = 1$  and  $f_L(\bar{E} + U) = f_R(\bar{E}) = f_R(\bar{E} + U) = 0$ . This approximation simplifies the current in the limit, that the double dot can only be occupied by up to a single electron, to

$$I = \frac{e}{\hbar} \frac{\Gamma_R \Delta^2}{\Delta^2 \left( 2 + \frac{\Gamma_R}{2\Gamma_L} \right) + 4(\varepsilon_{\text{ren}})^2 + \Gamma_R^2},$$

Neglecting renormalization effects (setting  $\varepsilon_{\text{ren}} = \varepsilon$ ), this equation reproduces for example Eq. (4.19) in the paper by Gurvitz [136]. Choosing the voltages such that the dot structure can also be doubly occupied,  $f_L(\bar{E} + U) = f_L(\bar{E}) = 1$  and  $0 = f_R(\bar{E}) = f_R(\bar{E} + U)$  one obtains Eq. (4.18) of Ref. [136].

Several publications assume, that if the lead Fermi energies are far away from the electronic states of the dots, then the principal value integrals (Eq. C.10), leading to the renormalization, can be neglected. However the energy shifts are relevant on an energy scale given by the charging energy  $U$ , as shown in Fig. 6.4a). Therefore the assumption, that one can neglect renormalization effects and still exclude states with more than one electron occupying the double dot is not justified.

### 6.5.1 Current-voltage characteristics

The energy shift of the localized levels is proportional to the tunnel coupling strength and depends on the dot-level positions relative to the respective lead Fermi energy. The renormalized level separation as function of the bias voltage is plotted in Fig. 6.4a). The level separation  $\varepsilon_{\text{ren}}$  reaches a (local) extremum each time, when the Fermi energy of a

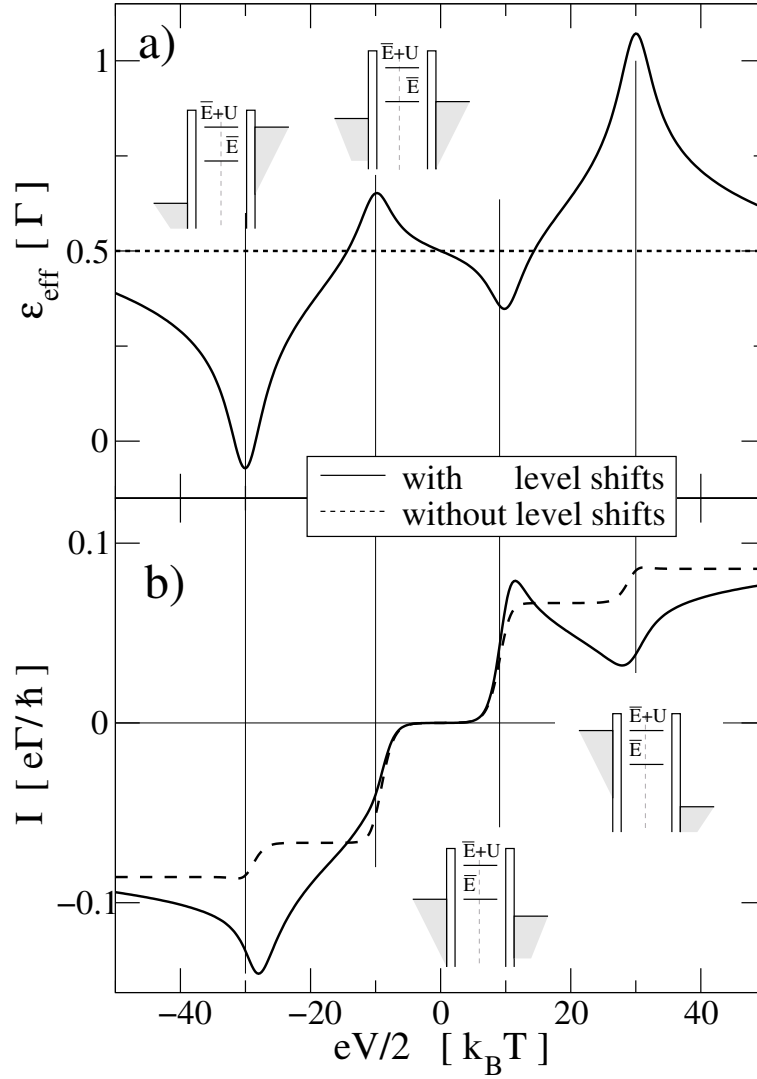


Figure 6.4: Upper Part: Renormalized level separation  $\varepsilon_{\text{ren}}$  (solid line) between the electronic levels in the left and right dot as function of the transport voltage  $V$ . The spacing  $\varepsilon_{\text{ren}}$  is extremal, when the chemical potential of a lead aligns with the energy needed for either single ( $\bar{E}$ ) or double occupation ( $\bar{E} + U$ ). Lower part: Current-voltage characteristics for bare (dashed line) and renormalized level spacing (solid line). Renormalization of energy levels causes an asymmetric current-voltage characteristic. The current increases (decreases) whenever the level spacing is reduced (increased) with respect to the bare value. Plot parameters are:  $\varepsilon = \Delta = \Gamma_R = \Gamma_L = \Gamma/2$ ,  $\bar{E} = 10k_B T$ ,  $U = 20k_B T$ , and  $U' = 100k_B T$ .

lead becomes resonant with the energy needed for single ( $\mu_r = \bar{E}$ ) or double occupation ( $\mu_r = \bar{E} + U$ ).

The Fig. 6.4b) shows the current as function of the transport voltage taking the level shift into account (solid line). By neglecting the level shifts (dashed line), the current shows a typical Coulomb staircase. The steps occur when a lead chemical potential aligns with the electronic levels in the double dot. Since the bare energy level separation  $\varepsilon$  as well as the inter-dot tunneling  $\Delta$  shall be of the order of or smaller  $\Gamma \geq \{\Delta, \varepsilon\}$  and we consider  $\Gamma < k_B T$ , the different single particle states are not resolved as individual steps in the  $I - V$  staircase. Within this approximation the results are independent of the ration  $\Gamma/k_B T$ , however it assumes that  $k_B T > \Gamma$ .

The tunnel induced renormalization introduces additional features in the staircase (solid line in Fig. 6.4b). Whenever the magnitude of the renormalized level spacing grows (drops) the current decreases (increases). This causes especially a suppression or an enhancement of the current around the steps of the  $I - V$  characteristic, leading to regions of negative differential conductance. The width of these feature is of the order of the charging energy and can exceed temperature and coupling strength significantly.

Neglecting renormalization effects and assuming symmetric coupling to the reservoirs ( $\Gamma_L = \Gamma_R$ ), the current through the double dot is an odd function of the transport voltage (see dashed line in Fig. 6.4b). This is no longer the case when renormalization is taken into account (see solid line in Fig. 6.4b). The reason for this asymmetry is that even though the change of asymmetry,  $\Delta E_L - \Delta E_R$ , caused by level renormalization is antisymmetric with respect to the bias voltage, this is not true for the total asymmetry  $\varepsilon_{ren} = \varepsilon + \Delta E_L - \Delta E_R$  due to the non-vanishing bare splitting  $\varepsilon$  (see Fig. 6.4a). A comparable asymmetry in transport through two coupled dots was recently observed by Ishibashi *et al.* [146] and theoretically described by Fransson *et al.* [140].

## 6.5.2 Stability diagrams

Unfortunately, a negative differential conductance feature can not be uniquely linked to the predicted renormalization effects. Due to interface capacities the level positions in the left and right dot are always affected by the transport voltage in real experiments [138, 147]. To exclude the effect of interface capacities, we propose a different experiment: measuring the current  $I(E_L, E_R)$  at a constant transport voltage as function of the left and right dot gate voltage  $V_L \propto E_L$  and  $V_R \propto E_R$ .

Let us first neglect renormalization effects, and consider a realistic multi-level dot with low bias voltage applied. By applying a larger gate voltage to the left dot, successively more electrons will occupy the left dot, analog the right dot. There are regions marked by  $(N, M)$  in Fig. 6.5, where the left dot is occupied by  $N$ , and the right dot by  $M$  electrons. If the two dots would be completely independent, these regions with fixed charge numbers would form a rectangular checkerboard pattern. But the charge interaction between the



two dots separates the  $(N, M)$  and the  $(N + 1, M + 1)$  states. Therefore the regions of stable charge occupations are six-sided and form a so called honeycomb pattern.

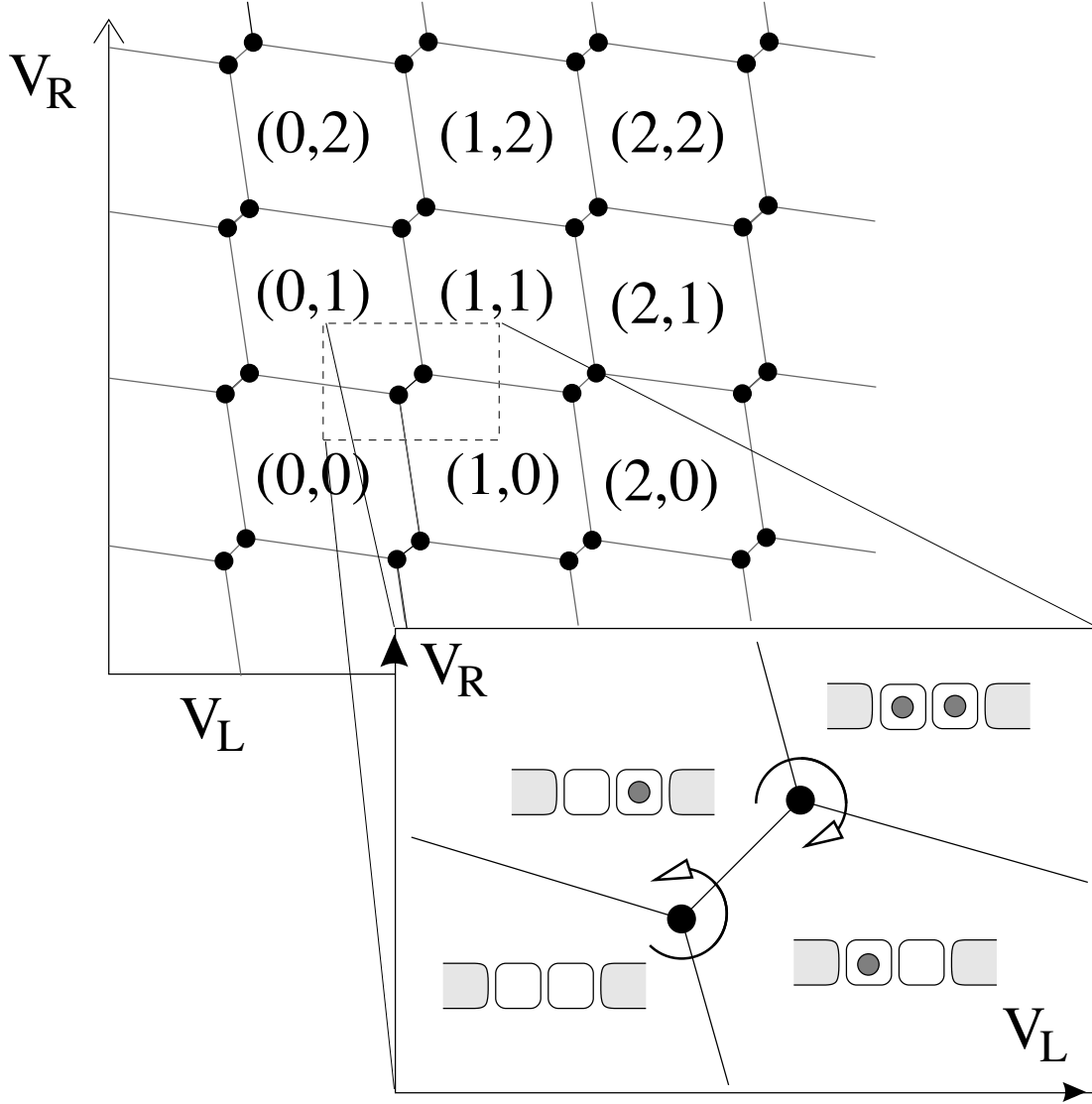


Figure 6.5: A honeycomb pattern marking the regions of fixed charge occupation numbers of the two dots in the gate voltage parameter space. Only at the intersection point of the regions of three charge states, current can cross the structure.

Transport through the double dot is only possible at gate voltages, where three different charge states are simultaneously energetically allowed, i.e., at the black points, see inset of Fig. 6.5. At the lower left point in the inset, the double dot can be empty, then an electron from the left lead can enter the left dot, can tunnel to the right dot and exit the structure. At the upper right point, the double dot must always stay occupied by at least

one electron. However, if the right dot is occupied, an electron can enter the left dot. Then the right dot electron can tunnel out, and afterwards the left dot electron can tunnel to the right dot. At finite source drain voltages these conducting points enlarge along the direction  $E_L \approx E_R$  to lines, see Fig. 6.6.

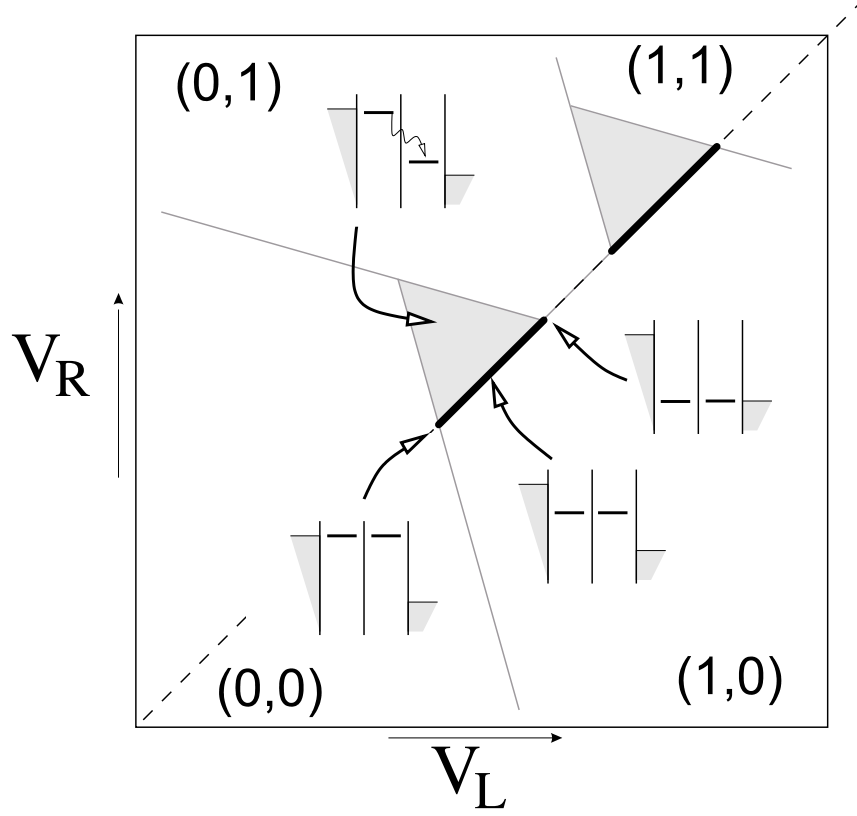


Figure 6.6: For a finite source drain voltage, the current allowing regions form stripes.

If we neglect level renormalization, elastic sequential tunneling from the left to the right dot is only possible if  $E_L = E_R$ . Furthermore electron transport from the left to the right reservoir takes only place if the dot level for single ( $\bar{E}$ ) or double occupation ( $\bar{E} + U$ ) is located in the bias voltage window. Therefore the current resonance forms two stripes in the regions  $-eV/2 < \bar{E} < eV/2$  and  $-U - eV/2 < \bar{E} < -U + eV/2$ . Away from the current stripes the occupation number of the left and right dot ( $N_L, N_R$ ) is fixed, and no current can cross the structure. For a detailed discussion on stability diagrams for transport through double dots we refer to the review of van der Wiel *et al.* [120].

Now we consider our full numerical result, and include the level renormalization. The resulting stability diagram is plotted in Fig. 6.7a).

We again can recognize the two current stripes. In the absence of renormalization effects, the current stripes would exactly coincide with the condition  $E_L = E_R$ . By plotting the current as function of the mean level position  $\bar{E} = (E_L + E_R)/2$  and the relative energy

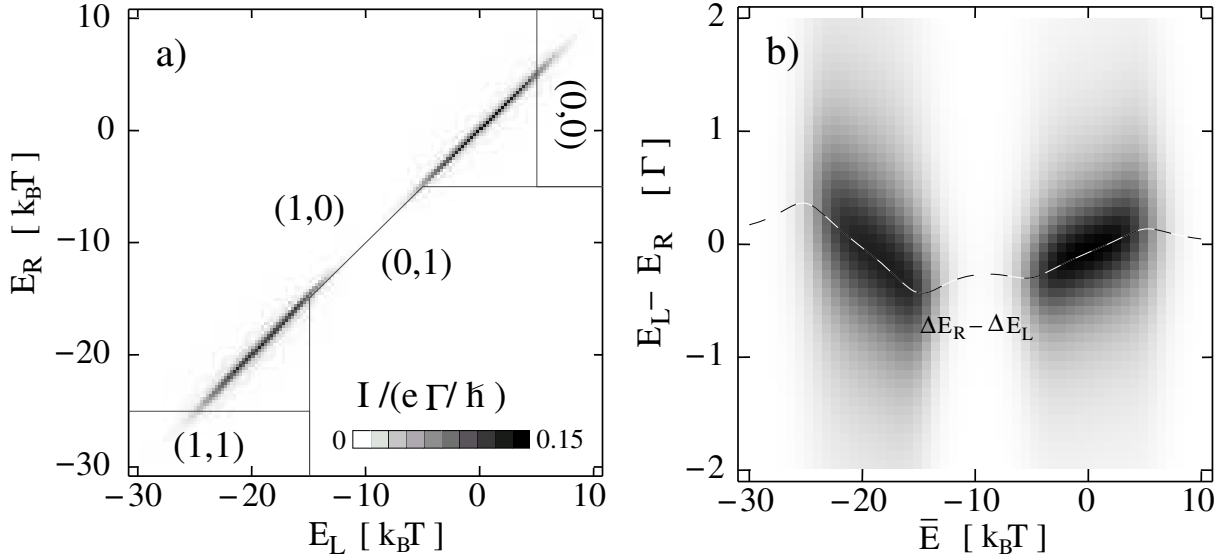


Figure 6.7: Left panel: Stability diagram  $I(E_L, E_R)$  of the current through the double dot in the nonlinear transport regime. Well inside the areas, separated by the black line, the occupation of the individual dots is fixed to the written values  $(N_L, N_R)$ . Elastic sequential current can cross the structure for  $E_L \approx E_R$  and either  $-eV/2 < \bar{E} < eV/2$  or  $-eV/2 < \bar{E} + U < eV/2$  resulting in two current stripes. Right panel: Gray scale plot of the current as function of the average single particle energy  $\bar{E}$  and the bare level separation  $\varepsilon = E_L - E_R$ . The different renormalization of left and right level shifts the current maxima by  $\Delta E_R - \Delta E_L$  (dashed black-white line) where  $\varepsilon_{\text{ren}} = 0$ . This causes a tilting of the current stripes relative to each other. Relevant plot parameters are  $k_B T = 2\Gamma$ ,  $\Gamma_L = \Gamma_R = \Delta = \Gamma/2$ ,  $V = 10k_B T$ ,  $U' = 100k_B T$ , and inter-dot charging energy  $U = 20k_B T$ .

difference  $\varepsilon = E_L - E_R$ , as done in Fig. 6.7b), one would therefore expect a straight horizontal line. Instead, the maximum of the current follows the renormalization shift, where the condition  $\varepsilon_{\text{ren}} = 0$  is fulfilled. The shift of the resonance is of order  $\Gamma$  as shown in Eq. (6.9) and can be small on the scale of bias voltage or temperature. However, the width of the current maxima in the stability diagram in Fig. 6.7 is not determined by temperature but rather by the dominant coupling strength  $\max(\Gamma, \Delta)$  [138]. Therefore the resonance width is sharp enough to be able to measure the renormalization of energy levels if  $\Gamma \gtrsim \Delta$  as used in Fig. 6.7.

In the nonlinear transport regime  $\Delta E_r$  depends on  $\bar{E}$  and therefore the current stripes in Fig. 6.7 are bent and tilted against each other. This dependence can be used as a stringent experimental prove of the renormalization of energy levels. Due to internal cross capacities, always appearing in real experiments, the gate voltage of one dot is a linear function of the gate voltage of the other dot. Therefore the stability diagram  $I(V_L, V_R)$  as plotted in Fig. 6.7a) would experience a linear shear transformation. However straight

(parallel) lines stay straight (parallel). Thus, cross capacities can not mimic the bending due to renormalization effects.

In real experiments in addition to the resonant current stripes explained here, further features can arise due to inelastic processes, co-tunneling, or due to excited levels within the bias voltage window [120]. These effects mainly lead to features within the triangles above the current strips in Fig. 6.6 and are expected not to interfere with our presented results.

## 6.6 Chapter summary

If a quantum dot is connected to a reservoir, the tunnel coupling causes an energy renormalization of the electronic dot states. In the quantum-dot spin valve, the spin-dependent renormalization leads to an exchange interaction causing intrinsic spin precession on the dot. In the serial double-dot device, the renormalization changes the energetic distance between the left dot energy level and the right dot level. This affects the conductance of such a double-dot structure already in the sequential tunnel regime, due to its high sensitivity on the relative detuning of energy levels. Therefore we propose to use a double-dot system as detector for these energy renormalization effects.

The renormalization affects the current-voltage characteristics, leading to regions of prominent negative differential conductances in voltage windows of the order of the charging energy. However, to exclude cross-capacity effects, it would be experimentally more usefull to measure the conductance as function of the two gate voltages for left and right dot at a fixed finite bias voltage. In the resulting stability diagram of the double dot, the current stripes are then tilted against each other and do not lie on a straight line, as it is the case when energy renormalization is neglected. The tilting of the current stripes is resolvable even in the sequential tunneling regime  $\Gamma > k_B T$ , as long as the inter-dot tunneling,  $\Delta$  is of the same order or smaller than the external coupling  $\Gamma \geq \Delta$ .

# Chapter 7

## Faraday-Rotation Fluctuation Spectroscopy

In the previous Chapters, we have discussed in detail the influence of the coherent spin dynamics on the transport characteristic of a quantum dot contacted by ferromagnetic leads. Beside transport also other experimental techniques are available to examine the spin dynamics in quantum dots like optical measurement methods.

### 7.1 Introduction

Mainly two optical measurement schemes for the spin dynamics in nanostructures are in use: the Hanle setup [148,149] and the time-resolved Faraday (or Kerr) rotation experiment [150,151]. The former rely on decrease of photoluminescence polarization due to an external magnetic field, the latter on the dependence of the phase velocity of polarized light on the spin orientation in the sample. The Hanle setup measures the spin of excited electrons, the Faraday setup does not require such excitation. That an optical measurement of the spin degree of freedom is possible at all is a consequence of spin-orbit coupling.

The main quantities, these experiments access, is the Landé  $g$ -factor and the spin-coherence time of electrons inside quantum dots. It is expected, that quantum dots exhibit very long spin-coherence times [81]. In locally confined systems, longitudinal spin relaxation times  $T_1$  up to microseconds were measured [153,154], but the size of the (transversal) spin-coherence time  $T_2$  is still under investigation. These long spin-coherence times makes spins in nanostructures promising candidates for quantum bits [155]. The anticipation of an application in quantum information processing is one main motivation for the intensive research on spin decoherence in semiconductors, and semiconductor nanostructures.

While time-resolved Faraday rotation as well as the Hanle measurement have proven to be a very precise experimental tool, capable to address spin decoherence times down to

a few ps, they have one main disadvantage. A measurement involves always an ensemble averaging over all illuminated spins. Due to local variations in the  $g$ -factor as well as due to hyperfine interaction, the individual spins in the sample will precess with slightly different frequencies, which gives rise to inhomogeneous line broadening. Therefore, the outcome of such a measurement is  $T_2^*$  instead of the bare spin-coherence time  $T_2$ .

In the following Chapter, a new optical experiment is discussed, which relies on the Faraday effect, but does not require time-resolution, which considerably simplifies the experimental setup: the Faraday-rotation fluctuation spectroscopy. Furthermore, we propose a modification of the already realized setup, to eliminate certain sources of inhomogeneous line broadening.

## 7.2 Experimental setup

A Faraday-rotation fluctuation experiment consists of the following components: a laser, an electromagnet, a polarization beam splitter, a balanced receiver, and a spectrum analyzer. The linearly polarized laser is transmitted through the sample, perpendicular to the magnetic field, see Fig. 7.1. After being transmitted through the sample, the laser light is split into two components by a polarizing beam splitter, which is rotated by  $45^\circ$  with respect to the initial laser polarization plane. The two components are recorded by photo diodes. A balanced receiver converts the difference of the output of the photo diodes into voltage, which is recorded by a spectrum analyzer.

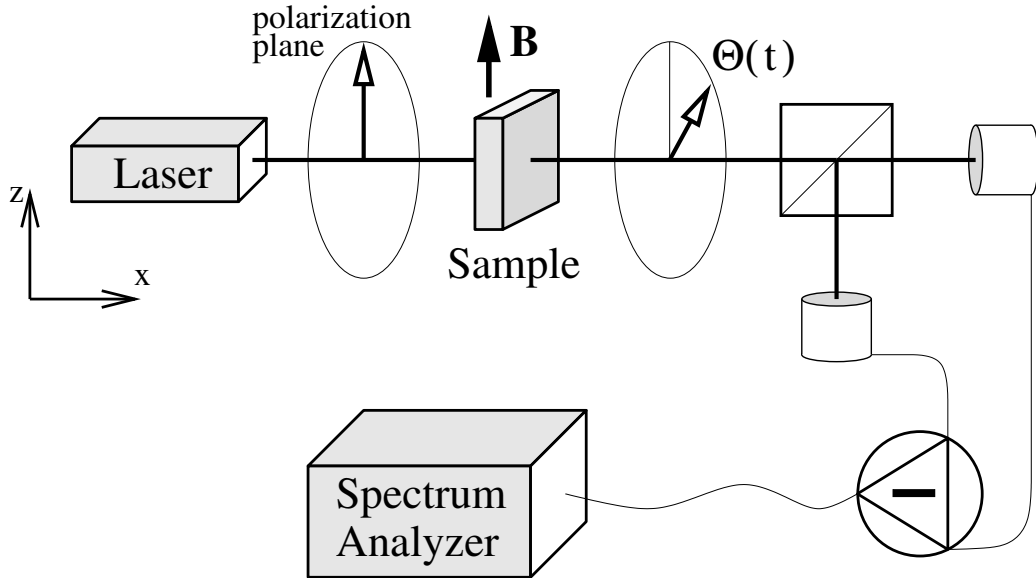


Figure 7.1: A linear polarized laser is sent through the probe. Due to the interaction with the electron spins, the polarization plane rotates, which gets recorded.

The laser photon energy is tuned slightly below the excitation energy of the spin states, to minimize absorption and maximize the Faraday rotation of the polarization plane. Since there is no average magnetization along the propagation direction of the laser light, the time averaged Faraday-rotation angle of the light is zero, and so is the average voltage recorded by the spectrum analyzer. However, while the average Faraday rotation and therefore the average voltage vanish, the fluctuations do not. The recorded voltage fluctuations are a direct measure of the Faraday-rotation fluctuations, which reflect the transverse spin-spin correlation function of the spins in the sample.

### 7.2.1 The experiment of Crooker *et al.*

The first measurement of this kind was reported by Crooker *et al.* [156]. They use a rubidium vapor cell as sample, with a vapor density of  $10^9$  atoms/mm<sup>3</sup>. The Ru valence-electrons are in the  $2S_{1/2}$  ground state. In the power spectrum of the recorded voltage noise, Crooker *et al.* observed Lorentzian resonance lines originating from the precession of spin fluctuations in the applied magnetic field, see Fig. 7.2. The position in frequency of the Lorentzian resonance equals the precession frequency of the electrons, and the line width corresponds to the transverse spin coherence time of 100ms. Here the measured time is rather the dwell time of the gas atoms in the laser spot than the true spin decoherence time which is on the order of a second for Ru. Two different lines were observed, which belong to the isotopes <sup>85</sup>Rb and <sup>87</sup>Rb. Due to hyperfine interaction, the different nuclear spins of <sup>85</sup>Rb ( $I = 5/2$ ) and <sup>87</sup>Rb ( $I = 3/2$ ) change the effective Landé  $g$ -factor of the electrons, and therefore their precession frequencies.

### 7.2.2 The experiment of Oestreich *et al.*

In contrast to the group of Crooker *et al.*, Oestreich *et al.* [157] used a solid-state sample: a 370  $\mu\text{m}$  thick GaAs wafer, which was  $n$ -doped with  $1.8 \cdot 10^{16}$  cm<sup>-3</sup> silicon. Also in this experiment the power spectrum of the Faraday-rotation fluctuations shows a Lorentzian resonance peak at the Larmor frequency of the electrons, see Fig. 7.3. Compared to the Rb gas, the electrons in the solid-state environment have a much shorter spin-coherence time of only 50 ns, and therefore the measured resonance line has a much larger line width.

## 7.3 Theoretical description

The experiments by Crooker *et al.* [156] and Oestreich *et al.* [157] can conveniently be described within a density-matrix formulation, as used in the previous Chapters of this dissertation. Since Faraday-rotation measures the spin component collinear with the laser propagation direction, the fluctuation of the Faraday rotation is a direct measure of the

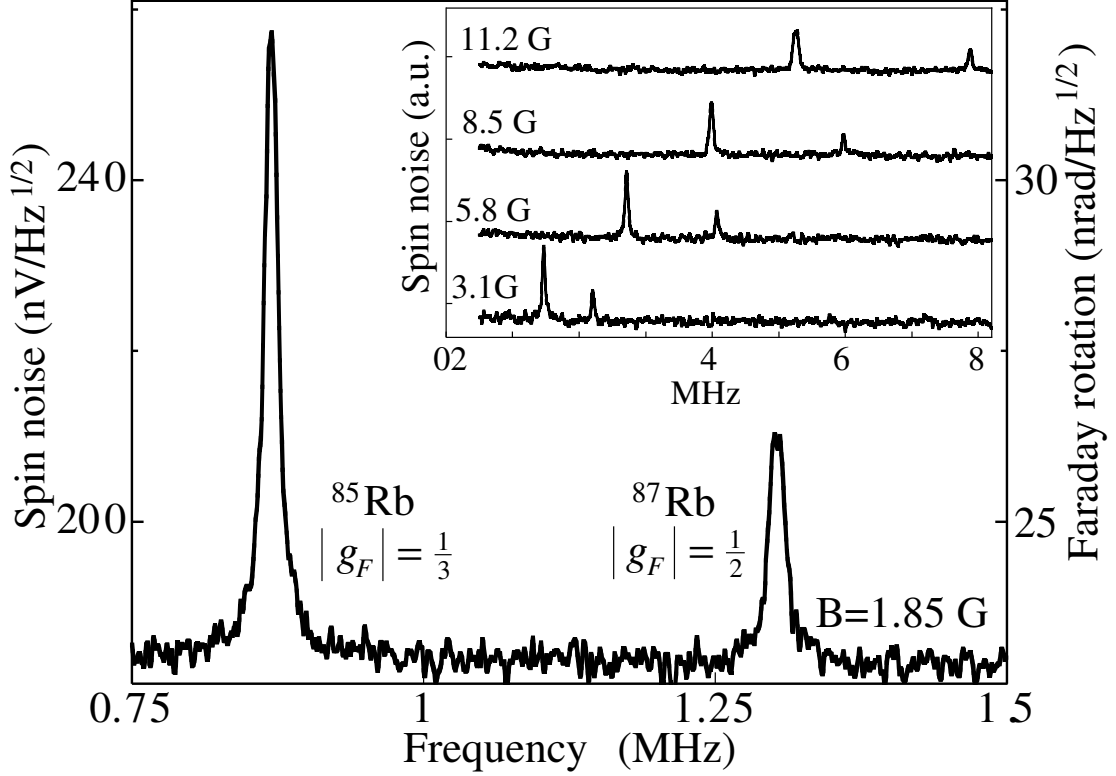


Figure 7.2: Faraday-rotation noise of Ru atoms as measured by Crooker *et al.* [156]. The Faraday fluctuations are of the order of  $\text{nrad}/\sqrt{\text{Hz}}$ .

transverse spin-spin correlation function

$$S(t) = \langle \hat{s}_x(t) \hat{s}_x(0) + \hat{s}_x(0) \hat{s}_x(t) \rangle. \quad (7.1)$$

The average of operators can be expressed by the trace  $\langle \hat{s}_x(t) \hat{s}_x(0) \rangle = \text{Tr}[\hat{s}_x(t) \hat{s}_x(0) \rho]$ , where  $\rho$  is the SU(2) density matrix describing one localized spin in the sample, and  $\hat{s}$  is the  $2 \times 2$  Pauli spin operator. The time evolution of the operator  $\hat{s}_x$  in the Heisenberg picture reads

$$\hat{s}_x(t) = \frac{\hbar}{2} \exp[i \int_0^t \hat{H}(\tau) d\tau] \sigma_x \exp[-i \int_0^t \hat{H}(\tau) d\tau], \quad (7.2)$$

if Hamiltonians at different times commute, which will be the case for a magnetic field. It is convenient to represent the correlator  $S(t)$  as a diagram with the operators  $\hat{s}_x(0)$  and  $\hat{s}_x(t)$  placed on a Keldysh time contour  $t_K$ , see Fig. 7.4. The spin states  $\uparrow, \downarrow$  propagate along the upper time contour from the time 0 to  $t$ , and on the lower line from  $t$  to 0. This takes into account the Heisenberg time evolution of  $\hat{s}_x(t)$  as in Eq. (7.2).

Instead of reading the time contour along  $t_K$  for the individual spin states of the Hilbert space, it is more intuitive to read the diagram from left to right, and interpret the double



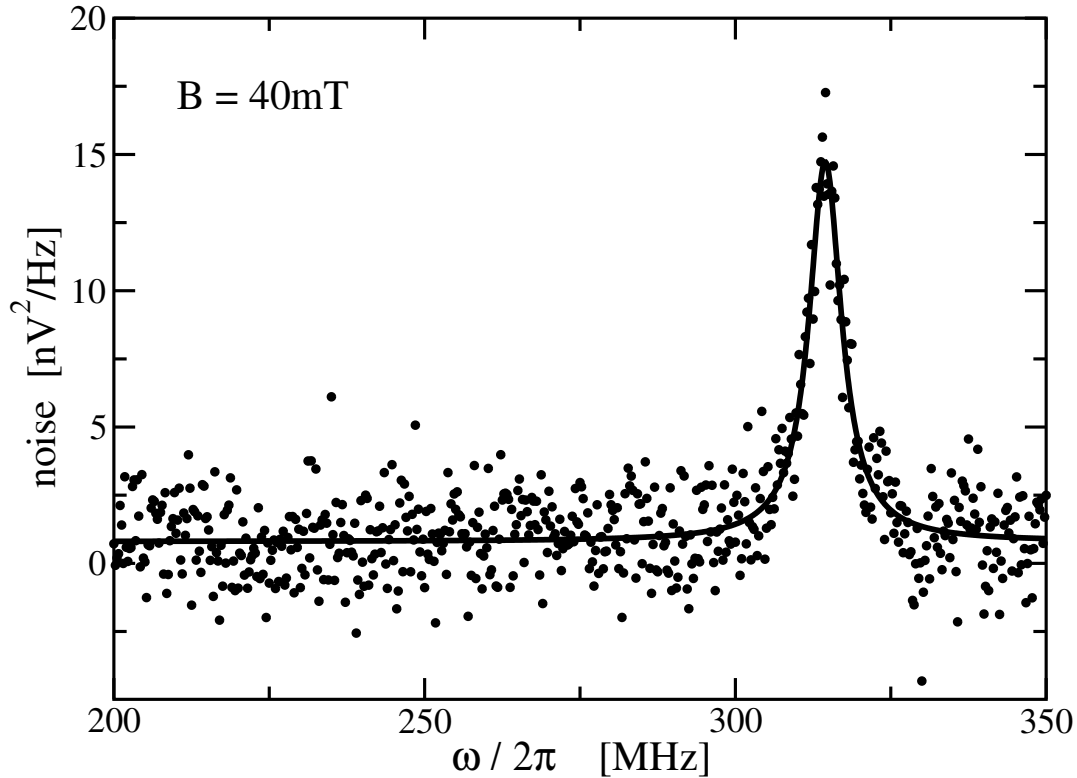


Figure 7.3: Faraday-rotation noise of a spin ensemble measured by Oestreich *et al.* [157], together with a fit to a Lorentzian function as expected for a single spin, see Eq. (7.5).

line of upper and lower Keldysh propagator as the time evolution of the whole density matrix  $\rho_{\sigma'}^{\sigma}$ . At time 0 the spin state of the initial density matrix  $\rho(0)$  is measured by the operator  $\mathbf{s}$ . Then, the density matrix propagates from time 0 to time  $t$ , and the spin is measured again. From this perspective, Eq. (7.1) can be rewritten as

$$S(t) = \frac{1}{2} \text{Tr}[\mathbf{s} \mathbf{\Pi}(t) \mathbf{s} \rho]. \quad (7.3)$$

The (Liouville) operator  $\mathbf{s}$  accounts for placing  $\hat{s}_x$  at the upper or lower Keldysh contour, flipping the spin from  $\sigma$  to  $\bar{\sigma}$ . By summing both possibilities, the time symmetrization of Eq. (7.1) is taken into account. The factor of 1/2 in Eq. (7.3) corrects for a double counting during this procedure. The (Liouville) operator  $\mathbf{s}$  is a fourth order tensor with  $s_{\sigma'\bar{\sigma}}^{\sigma\sigma'} = s_{\sigma'\bar{\sigma}}^{\sigma'\bar{\sigma}} = \hbar/2$  and zero otherwise.

Between the two spin measurements at time 0 and time  $t$ , the propagation of the density matrix is described by  $\Pi_{\sigma'\sigma'}^{\sigma\sigma'}(t) = \exp \left\{ -i \int_0^t [\langle \sigma | \hat{H}(\tau) | \sigma \rangle - \langle \sigma' | \hat{H}(\tau) | \sigma' \rangle] d\tau \right\}$ . Since the spin quantization axis is chosen along the magnetic field, the states  $\sigma, \sigma'$  are eigenstates of the Hamilton operator, and no elements of  $\Pi$  with different spin indices on the upper

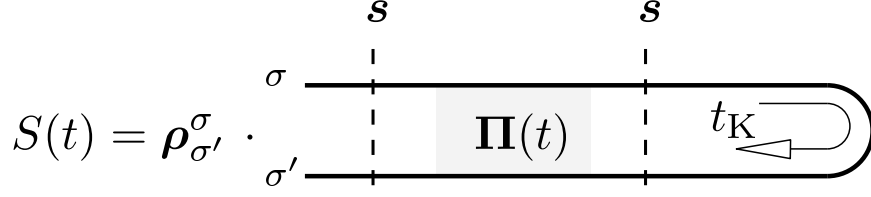


Figure 7.4: Diagrammatic representation of  $S(t)$ . The operators  $\hat{s}_x$  are placed on the time contour at time 0 and  $t$ , respectively.

(or the lower) propagator appear.

The formulation of Eq. (7.3) offers the possibility to phenomenologically include transverse spin relaxation in the calculation. If the initial density matrix was in a diagonal state, the first spin operator  $\hat{s}_x$  brings it into a non-diagonal state  $\rho_\sigma^\sigma$ . During the time evolution from 0 to  $t$  non-diagonal density matrix elements decay exponentially with the time scale set by the spin-coherence time  $T_2$ . This is accounted for by multiplying  $\Pi_{\sigma\sigma}^{\sigma\sigma}(t)$  with  $\exp(-t/T_2)$ .

The Hamilton operator describing the spin states in the presence of a static magnetic field is  $H(t) = -\omega_0 \hat{s}_z$  with  $\omega_0 = g\mu_B B$ . Consequently the propagator is then given by

$$\Pi_{\sigma\sigma}^{\sigma\sigma} = 1, \quad \Pi_{\downarrow\downarrow}^{\uparrow\uparrow} = e^{i\omega_0 t - t/T_2}, \quad \Pi_{\uparrow\uparrow}^{\downarrow\downarrow} = e^{-i\omega_0 t - t/T_2}. \quad (7.4)$$

The resulting power spectrum  $S(\omega) = \int_0^\infty dt [\exp(-i\omega t) + \exp(i\omega t)] S(t)$  of the time-dependent correlator  $S(t)$  equals then

$$S(\omega) = \frac{\hbar^2}{2} \left( \frac{T_2}{1 + T_2^2(\omega - \omega_0)^2} + \frac{T_2}{1 + T_2^2(\omega + \omega_0)^2} \right). \quad (7.5)$$

It shows a Lorentzian resonance centered at the Larmor frequency  $\omega_0$ . In Fig. 7.3, we performed a fit of a Lorentzian to the experimental data of Oestreich *et al.* [157].

The origin of the resonance can be understood by tracking the time evolution of the spin between the two measurements. Let us assume that at time  $t = 0$  the spin is aligned parallel to the direction of measurement, as shown in Fig. 7.5. The outcome of the first measurement therefore equals  $s_x = +\hbar/2$ . This spin then precesses in the static external magnetic field. If the time between first and second measurement is an integer times the time for a full revolution of the spin, the outcome of the second measurement will most probable be  $s_x = +\hbar/2$ , i.e., the results of the two measurements coincide. The spin relaxation on the time scale  $T_2$  decreases the probability to measure the same spin state. For half-integer multiples of the spin revolution time, the measurement results will have opposite signs. The spin-spin correlation function is, therefore, an oscillating function in time, which is exponentially damped due to decoherence. The corresponding power spectrum is a Lorentzian centered at the Larmor frequency  $\omega_0$  with a width of  $T_2$ . This argument also holds, if the initial spin state is a coherent superposition of spin up and down, which implies, that the initial spin is unimportant. This can also be seen from

the fact, that Eq. (7.5) is independent of the initial density matrix. Therefore, in contrast to ESR and ESR-like experiments, no initial net magnetization of the sample is needed.

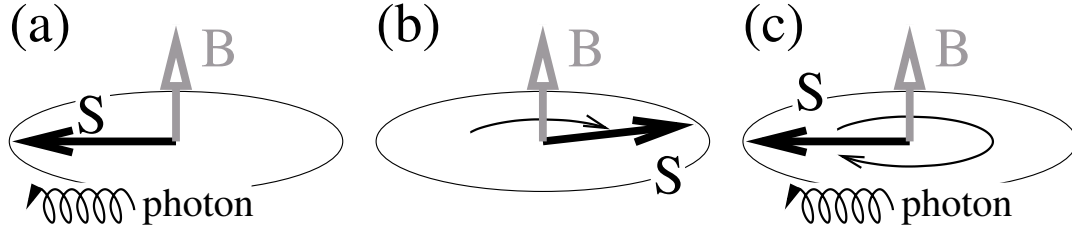


Figure 7.5: Sketch of the electron-spin dynamics in the Faraday setup with a static magnetic field. (a) At time  $t = 0$ , the spin is measured. (b) Between the two measurements, the spin precesses in a static transversal magnetic field  $\mathbf{B}$ . (c) If the second measurement takes place after a full revolution of the spin, it reproduces the outcome of the first measurement.

## 7.4 Spin life time and line broadening

The experimental relevant variables of such a Faraday-rotation fluctuation experiment as well as in any other electron-spin-resonance like experiment is the line position and the line width. With the knowledge of the applied field strength, the line position in frequency is a direct measure of the Landé  $g$ -factor. The spin coherence time is given by the inverse of the line width. There are several physical mechanisms limiting the spin coherence time.

### 7.4.1 Spin-orbit coupling

One source of decoherence is spin-orbit coupling. Spin-orbit coupling can lead to a variety of different relaxation mechanisms. The most important mechanisms are Elliott-Yafet [158, 159] and D'yakonov-Perel' [160, 161].

In the presence of spin-orbit coupling, the spin-up and spin-down states are not longer energy eigenstates of electrons with finite momentum. The new momentum eigenstates are an admixture of the two spin states. Therefore, if an electron experiences any kind of scattering event, by a phonon or a lattice disturbance for example, there exist a finite overlap of the different spin states, and spin flip scattering can occur. This mechanism is called Elliott-Yafet mechanism [158, 159].

For the D'yakonov-Perel' spin relaxation mechanism [160, 161], spin-orbit interaction can be seen as a magnetic field, which depends on the momentum of the electron. Since the electron motion in the semiconductor is random due to random scattering events, also this magnetic field is inducing random precession of the spin, which generates decoherence.

While spin-orbit coupling is expected to be the dominant limitation of spin coherence in extended structures, it is expected, that the spatial confinement of electrons in nanostructures strongly suppresses these spin-relaxation mechanisms [77, 152], leading to long spin coherence times.

### 7.4.2 Hyperfine interaction

The source of spin decoherence, which is expected to dominate spin relaxation in nanostructures is the coupling of the electron spins to the nuclear spins via hyperfine interaction [79–81, 162]. The nuclear spins are usually randomly distributed, so that on average they do not generate a magnetic field. However, in a statistic distribution of nuclear spins, statistic fluctuations are present. The electron spin can then precess in the hyperfine field generated by bunches of accidentally aligned nuclear spins.

### 7.4.3 Inhomogeneous line broadening

Currently available experimental setups, like the Faraday-rotation fluctuation, Hanle and time-resolved Faraday-rotation measurements, but also standart ESR setups are not capable of measuring an individual spin. To get a reasonable signal, an average over a spin ensemble has to be performed. However, this ensemble averaging does not only increase the signal strength, but also can leads to a broadening of the resonance. Due to local variations of either the  $g$ -factor in the sample or the strength of the external magnetic field, but also due to the different realizations of the hyperfine field in the vicinity of individual spins, each spin precess with a slightly different frequency. By adding the individual spin contributions to the measurement signal, the inverse line width becomes  $T_2^*$  instead of the bare spin-coherence time  $T_2$ .

Especially in materials containing elements with a high nuclear spin, hyperfine interaction can be the dominating source of decoherence. On the other side, inhomogeneous broadening due to  $g$ -factor variations becomes more and more important with a decrease of sample homogeneity. For example in chemically synthesized nanostructures, like nanocrystalline CdSe quantum dots, spin life-time measurements are completely dominated by inhomogeneous broadening [163, 164]. Since the size and shape of the synthesized quantum dots vary, also the  $g$ -factor will be different for each dot.

Such an inhomogeneous broadening of the line width can be avoided by a spin-echo experiments, as first demonstrated for NMR by Hahn [165] and for ESR by Blume [166]. The idea behind this approach is to prepare an initial polarized spin state, and let it precess in a magnetic field. After some time  $T$  the spin direction is flipped by a  $\pi$ -pulse. From the perspective of the spin-system the static magnetic field switches, and as a consequence, the spins precess in backward direction. At time  $2T$ , irrespective of the precession frequency of the individual spins, all spins will align again, giving rise to an ‘echo’ of the original spin

state. Considering the height of the spin echo as function of time  $2T$  constitutes a direct measurement of the bare spin-coherence time.

To reduce inhomogeneous broadening in a Faraday-rotation fluctuation measurement, we propose an experiment, that is analog to spin-echo spectroscopy. The experiment will be not as powerfull as pulse-ESR, since it will be capable of subtracting the influence of  $g$ -factor and field strength variations only, and not reduce the influence of hyperfine interaction. However, in contrast to pulse-ESR it will be a continuous wave experiment, and therefore does not require any time resolution, which considerably simplifies the experimental implementation.

## 7.5 Proposal to reduce inhomogeneous broadening

We suggest to use an oscillating magnetic field instead of a static one in the Faraday-rotation fluctuation setup. Then the resonance will not appear at the (locally varying) Larmor frequency determined by the *strength* of the magnetic field, but at multiples of the magnetic-field *frequency*. Since the field frequency does not vary locally, inhomogeneous broadening due to chemical or structural sample inhomogeneities is avoided. However, the line broadening due to hyperfine interaction will persist.

The difference to the case of a static magnetic field is that the spin precession between the two measurements changes its direction as a function of time. The spin detected by the initial measurement first precesses in one direction but then stops and precesses back. After a full oscillation period of the external field, the spin will be just back at its starting point, see Fig. 7.6. If the second measurement takes place at this time, the outcome will be equal to the first measurement, i.e., the measurements will be correlated.

Technically, an oscillating magnetic field is described by the time dependent Hamiltonian

$$H(t) = -\omega_0 \sin(\gamma t + \phi) \cdot \hat{s}_z \quad (7.6)$$

where  $\gamma$  labels the field oscillation frequency. With this Hamiltonian, the propagator  $\mathbf{\Pi}(t)$ , including a phenomenological relaxation term, can be constructed. Since the experiment should be a continuous-wave experiment, there shall be no correlation between the phase of the magnetic field oscillation, and the absolute time of measurement of the spins. Therefore, the propagator is averaged over the relative phase  $\phi$ , and equals  $\Pi_{\downarrow\downarrow}^{\uparrow\uparrow}(t) = \int_0^{2\pi} (d\phi/2\pi) \exp[-t/T_2 - i\omega_0/\gamma (\cos(\gamma t + \phi) - \cos \phi)]$ . The explicit calculation of this integral is shown in Appendix D. The power spectrum of the spin-spin correlation function

$$S(\omega) = \hbar^2 \sum_{n=-\infty}^{+\infty} \left[ J_n \left( \frac{\omega_0}{\gamma} \right) \right]^2 \frac{T_2}{1 + T_2^2 (\omega + n\gamma)^2} \quad (7.7)$$

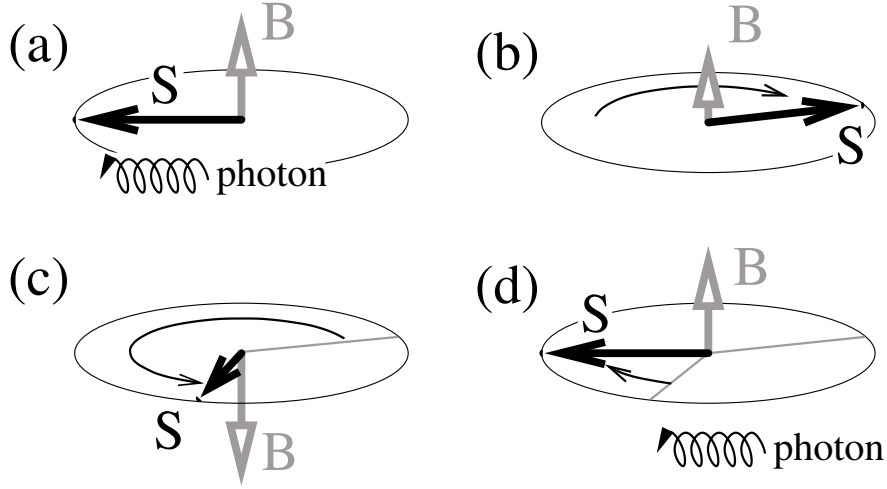


Figure 7.6: Sketch of the spin dynamics in the Faraday setup with an oscillating field: (a) The initial measurement of the spin state. (b) In the external field the spin precesses in one direction. (c) When the field changes its sign, the spin precesses in the opposite direction. (d) After a full field-oscillation time, the spin is again in its initial state.

consists of a series of Lorentzian resonances of the width  $T_2^{-1}$ , as plotted in Fig. 7.7. The signal strength is proportional to the square of Bessel functions  $J_n$  of the first kind. If the argument of these Bessel functions is of the order of 1, one can expect approximately half of the signal magnitude compared to the case of a static magnetic field [157].

The relevant property of the correlation spectrum is, that the resonances appear at multiples of the oscillation frequency  $\gamma$  of the external magnetic field. Since this frequency does not vary locally over the sample, the width of the resonances is not influenced by variations of the  $g$ -factor in the sample. This is different to the case of a static magnetic field, where the position of the resonance is defined by the Larmor frequency of the spins.

The appearance of these multi-resonances is extensively discussed in the context of ESR and NMR, see Ref. [167] and citations therein. In magnetic resonance experiments, the absorption of radiation is measured, which can induce transitions between Zeeman splitted energy levels. By adding a modulating signal on top of the static magnetic field, responsible for the Zeeman splitting, a spectrum comparable to Eq. (7.7) is found. However, the spectrum is shifted by the Larmor frequency associated with the static magnetic field. Therefore, by averaging over an ensemble of spin systems, the spectrum is again influenced by inhomogeneous broadening. In contrast, for the Faraday-rotation fluctuation spectroscopy scheme that we propose, no static magnetic field is needed, and inhomogeneous broadening is less pronounced.

To understand the sequence of peak heights in Fig. 7.7,  $S(\omega)$  is shown in Fig. 7.8 as a gray scale plot as function of  $\omega/\gamma$  and  $\omega_0/\gamma$ . The horizontal lines indicate the parameters

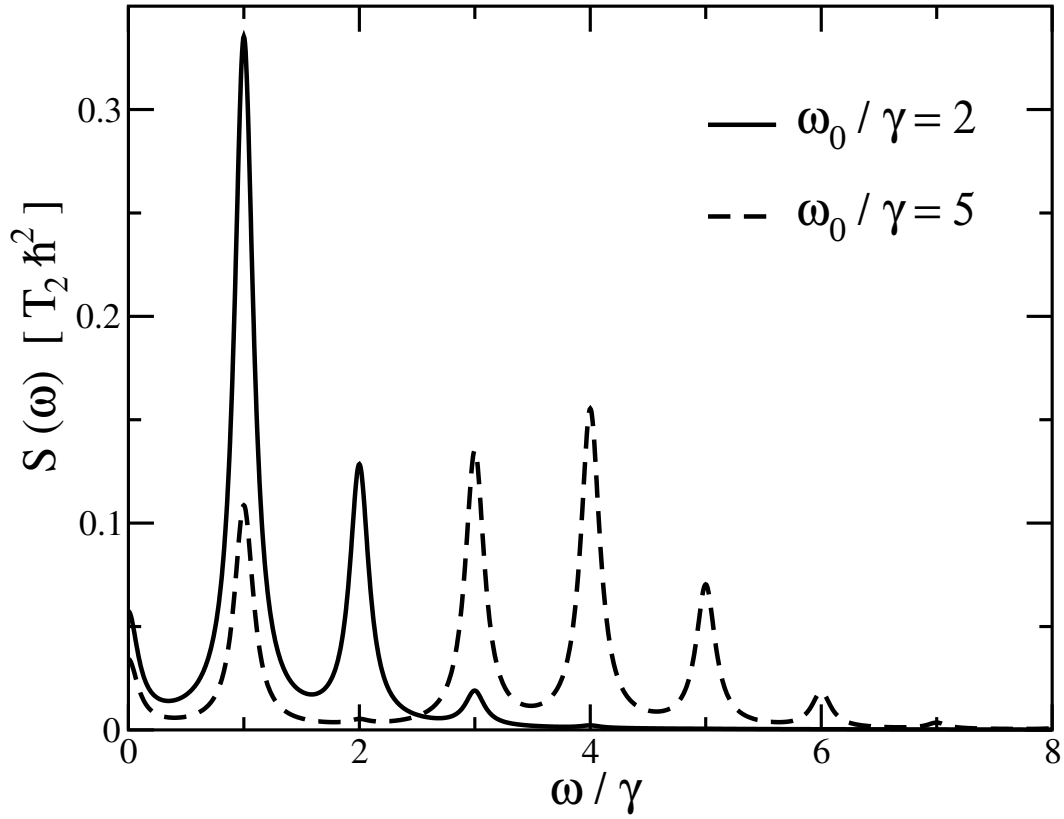


Figure 7.7: Spectrum of the spin-spin correlation function for different ratios of magnetic field strength to oscillation frequency. For a higher ratio  $\omega_0/\gamma$ , more resonance lines appear for higher frequencies, while the signal strength decreases. Here, we chose  $T_2^{-1} = 0.1\gamma$ .

for the two spectra in Fig. 7.7. If the time between the two spin measurements falls significantly below the time needed by a spin to close its trajectory, no spin correlation can be measured. Therefore Fig. 7.8 shows no signal in the parameter range  $\omega > \omega_0$ .

While the only physical limitation of the proposed experiment is that the sample structure must exhibit spin-orbit coupling, the generation of the oscillating magnetic field defines the technical limitation. To measure the line width  $T_2$ , individual lines must be resolved. Therefore the separation of the lines given by the field frequency  $\gamma$  must exceed  $T_2^{-1}$ . Furthermore, to get the resonance at  $\omega \neq 0$ , the field strength  $\omega_0$  must be comparable to the field frequency  $\gamma$ .

Oestreich *et al.* measured a  $T_2^*$  of 50ns in a GaAs sample. If we use this time as the lowest boundary for  $T_2$ , and demand a separation to width ratio of 5:1, the frequency of the oscillating magnetic field should be of the order of 100 MHz, and have a strength of 16 mT. Such a field configuration is technically challenging. Even though GaAs is a less interesting sample, since it is assumed, that hyperfine interaction is dominating the line width, a proof of principle should be possible with such a sample.

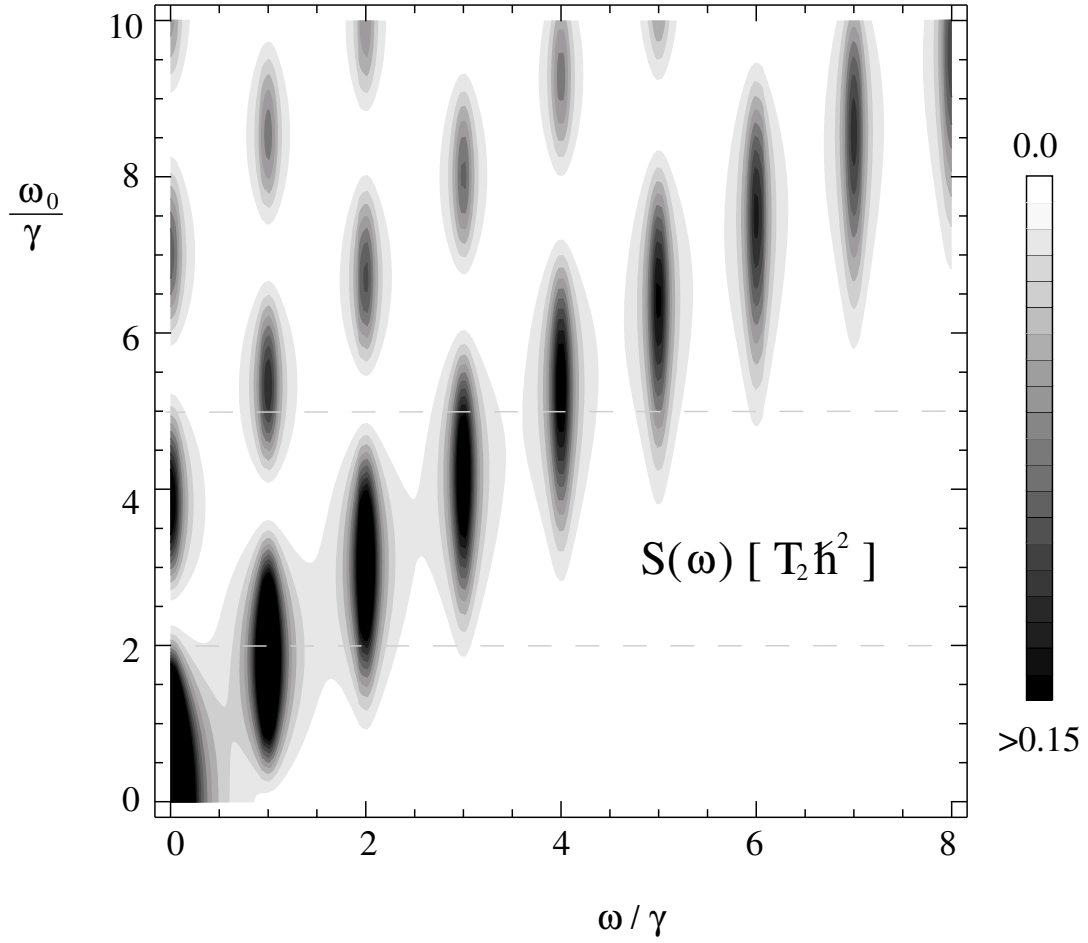


Figure 7.8: Spin-spin correlation spectrum, as function of the ratio  $\omega_0/\gamma$  and frequency  $\omega$  for  $T_2^{-1} = 0.1\gamma$ .

Inhomogeneous broadening due to sample variations becomes more important either for systems with larger spatial fluctuations like quantum-dot ensembles [151, 164], or for systems with larger spin-coherence times (= less hyperfine interaction). The latter also have the advantage, that the experimental requirements for the oscillating magnetic field relax. For example in Si, where hyperfine interaction is weaker compared to GaAs, a  $T_2$  of  $1\mu\text{s}$  would be detectable with a technical easily realizable field of  $180\mu\text{T}$  at an oscillation frequency of 5 MHz. In the case of a Rb gas sample with a spin-coherence time exceeding  $100\mu\text{s}$  [156], the field requirements relax even further. Since for maximum signal strength,  $\omega/\omega_0$  should be of the order 1, and for lower frequencies other sources of noise such as  $1/f$ -noise become more important, the magnetic field strength has a lower practical bound.



## 7.6 Connection to quantum computation

Recently such a “Bessel staircase” as in Fig. 7.8 was measured by Oliver *et al.* [168], not in a spin system but for the excitation probability in a strongly-driven superconducting flux qubit used as Mach-Zehnder interferometer.

A flux qubit is a system with effectively two quantum mechanical states  $|0\rangle$  and  $|1\rangle$ , where each state represents a circular super-current which encloses either  $N$  or  $N + 1$  flux quanta. By applying an external magnetic flux, the energies of the states change, see Fig. 7.9. At a certain external magnetic field, it becomes energetically favorable, that another flux quantum enters the superconducting ring, i.e., the two levels  $|0\rangle$  and  $|1\rangle$  cross. However, due to the Josephson junction in the qubit, this level crossing is avoided, leading to a gap of the energy  $\Delta$ .

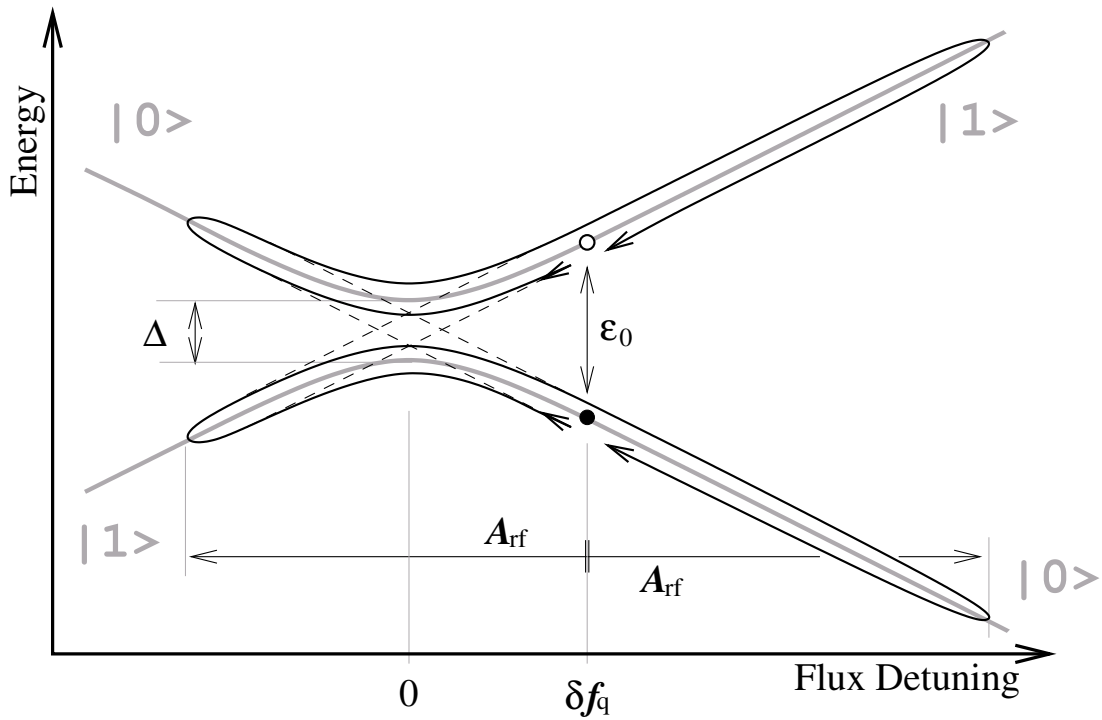


Figure 7.9: Avoided level crossing of the flux qubit.

Oliver *et al.* [168] prepared the qubit in the initial state  $|0\rangle$  by applying a static flux detuning  $\delta f_q$ , marked by the black dot in Fig. 7.9. Then, they applied an oscillating magnetic field resulting in an oscillating detuning of the qubit. If the oscillation frequency and the strength of the magnetic field exceeds the energy level separation  $\Delta$ , the qubit does not adiabatically follow the avoided level crossing (straight line), but Landau-Zener transitions between the levels can take place (dashed lines).

After applying the oscillating magnetic field with a maximum strength of  $A_{\text{rf}} \propto V_{\text{rf}}$

for  $1\mu\text{s}$ , the probability to find the qubit in the state  $|1\rangle$ , (marked by the open circle in Fig. 7.9) was measured by a dc-SQUID. Since the state of the qubit can evolve via different paths, like in a Mach-Zehnder interferometer, during the oscillation of the flux detuning, the resulting occupation probability shows an interference pattern, see Fig. 7.10, which Oliver *et al.* labeled *Bessel staircase*.

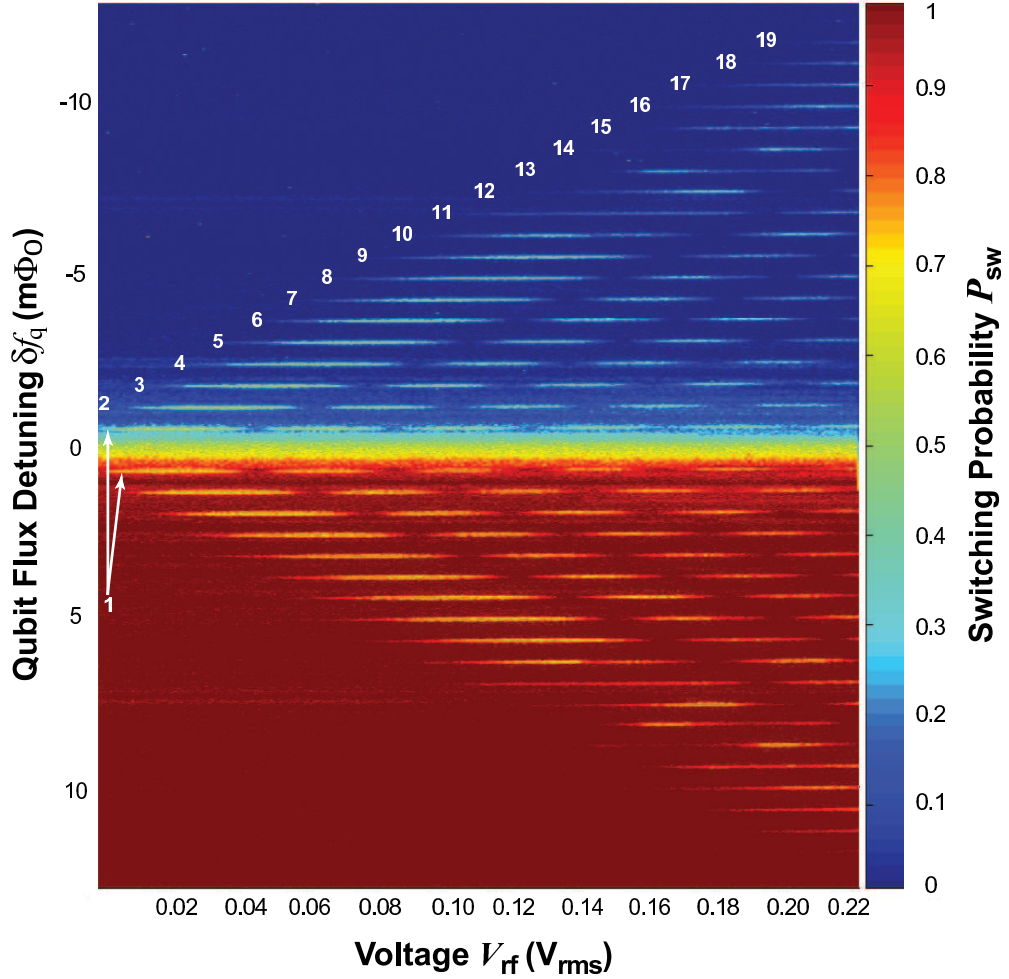


Figure 7.10: Measured probability to find the qubit in the state  $|1\rangle$  (or  $|0\rangle$ ), after irradiating the qubit state  $|0\rangle$  (or  $|1\rangle$ ) with an oscillating magnetic field. If the static flux detuning  $\delta f_q$  exceeds the oscillation amplitude  $A_{\text{rf}} \propto V_{\text{rf}}$ , the qubit never reaches the avoided level crossing, see Fig. 7.9, and no transition can be observed.

The reason that this qubit experiment and a Faraday-rotation fluctuation spectrum shows similar results is the fact, that both, qubit and spin are two level systems. The main difference between the two presented experiments is the line width of the resonances. In

the Faraday setup the width is given by incoherent spin relaxation, while in the qubit case the coherent influence of the Josephson coupling determines the width. The qubit can be described by the Hamiltonian

$$H = -\frac{1}{2} \left( \Delta \sigma_x + [\delta f_q + A_{\text{rf}} \cos(\omega t)] \sigma_z \right). \quad (7.8)$$

The qubit experiment corresponds to the following spin dynamics. At the beginning of the experiment, the spin is prepared in the state  $|0\rangle = |\uparrow\rangle$ . The Josephson coupling resembles a static magnetic field in the x-direction, and the magnetic field aligned along the z direction generates the static Zeeman splitting  $\delta f_q + A_{\text{rf}} \cos(\omega t)$  of the energy levels  $|\uparrow\rangle = |0\rangle$  and  $|\downarrow\rangle = |1\rangle$ . After a fixed time [ $1\mu\text{s}$  in the experiment of Oliver *et al.* [168]], one measures the chance to find the spin in the state  $|\downarrow\rangle = |1\rangle$ .

Without the Josephson coupling  $\Delta$ , i.e., without a magnetic field in the x-direction, the spin states  $|\uparrow\rangle$  and  $|\downarrow\rangle$  would be eigenstates, and no spin flip would be detectable. The Josephson coupling however leads to a spin precession away from the z-direction. Thereby a situation similar to the Faraday-rotation experiment is reached. The transversal spin components precess forward and backward in the oscillating magnetic field generating the Bessel staircase structures. In contrast to the Faraday experiment, the transition between the states  $|\uparrow\rangle$  and  $|\downarrow\rangle$  are not incoherently induced by decoherence, but a coherent rotation by the Josephson coupling. Therefore the line width of the resonances in the qubit experiment is not given by the coherence time, but is a more complex function of  $\Delta$  as discussed in Ref. [168].

In the Faraday setup, one measures the spin-spin correlation as function of the noise frequency. In the qubit case, the measured quantity is also a correlation function: to measure the state  $|1\rangle$  after a fixed irradiation time, if the state was  $|0\rangle$  at the beginning of the experiment. However, one does not measure this correlation as function of frequency, but at a fixed frequency corresponding to the inverse irradiation time. The role of the noise frequency is played by the static flux detuning  $\delta f_q$ . If one performs the calculation for the spin-spin correlation function in Section 7.5 with a static and an oscillating magnetic field, one would recover Eq. (7.7), but with  $\omega$  replaced by  $\omega + \Delta$ . Therefore  $S(\omega)$  and  $S(\Delta)$  show the same functional form.

## 7.7 Chapter summary

In this Chapter, the Faraday-rotation fluctuation experiments by Crooker *et al.* [156] and Oestreich *et al.* [157] were theoretically discussed. Further, a new way to measure the spin-coherence time  $T_2$  is proposed, namely to measure Faraday-rotation fluctuations in the presence of an oscillating magnetic field. Such an experiment can measure the spin coherence time  $T_2$  of electron spins *with reduced inhomogeneous broadening*. The spin-spin correlation function shows resonances in the power spectrum at multiples of the oscillation frequency of the external field. As this frequency is not subject to local variations,

the resonance line width is given only by the bare spin coherence time  $T_2^{-1}$  and the influence of hyperfine interaction. This contrasts with Hanle or time-resolved Faraday-rotation measurements that are fragile against all sources of inhomogeneous broadening. Faraday-rotation fluctuation in the presence of an oscillating magnetic field is on one side a less powerful tool than pulse-ESR, since the influence of hyperfine interaction persists. On the other side, it is experimentally simpler to realize, since in contrast to pulse-ESR the Faraday-rotation measurement does not require any time resolution at all.

# Chapter 8

## Conclusions

In this dissertation, the possibility to *generate*, *manipulate*, and *detect* single spins in transport through a quantum-dot spin valve was discussed.

In Chapter 2, we introduced the mathematical description of a quantum-dot spin valve. As quantum dot, we used the Anderson impurity model, and the ferromagnets were modeled in the Stoner picture. We have chosen this system since it is the *simplest non-trivial device* to examine the influence of strong charge interaction on spin currents. Within this approach, we want to describe experiments measuring transport through grains embedding in F/I/F tunnel junctions, carbon nanotubes or  $C_{60}$  molecules contacted by ferromagnetic leads, or impurities contacted by ferromagnetic STM.

In the quantum-dot spin valve, a bias voltage leads to the accumulation of a non-equilibrium spin on the otherwise non-magnetic single-level quantum dot, as discussed in Chapter 3. This accumulation can be seen as the *preparation* of a certain spin state. The time-averaged accumulated spin adapts to outer circumstances in such a way, that the sum of incoming and outgoing spin currents vanish. A rigid calculation of the spin current through a tunnel barrier between ferromagnet and single-level quantum dot showed, that the transfer of angular momentum has two qualitatively different contributions. One spin current contribution is associated with the fact that the charge current from or to a spin polarized system is also spin polarized. This current, thus, transfers angular momentum along the magnetization direction of the ferromagnet or along the accumulated spin. Furthermore, in systems with strong charge interaction, such as quantum dots, the spin current also has a transversal component, perpendicular to both, lead magnetization and dot polarization. This component leads to an intrinsic spin precession of the spin on the quantum dot, that can be described in terms of an exchange field. Several previous publications, which tried to describe spin transport through quantum dots in weak coupling by an ‘ad hoc’ rate equation approach missed this exchange interaction.

At the interface between magnetized lead and spin-polarized dot, magnetoresistance occurs. Therefore the accumulated spin influences the transport characteristics of the

device. Each manipulation of the dot spin is *detectable* in the conductance of the quantum-dot spin-valve device, as shown in Chapter 4. Two different ways to influence the spin were discussed. By an external magnetic field, one can induce a precession of the dot spin, which reduces the overall spin-valve effect. Such an experiment is an all electrical analogue to the optical Hanle effect, and can be used to measure the spin coherence time  $T_2$  of a *single* quantum dot. Furthermore, one can *electrically manipulate the spin* in a direct way. Since the many-body exchange field is a function of bias and gate voltage, these voltages can directly affect the spin degree of freedom of the dot. In particular, this interaction-driven intrinsic spin precession modifies the dependence of the linear conductance on the opening angle of the lead magnetizations. The strength of this modification is tunable by gate voltage. In nonlinear response, the bias voltage dependence of the exchange field can give rise to regions of negative differential conductance.

These results are not specific for quantum-dot spin valves but apply for any two-level system tunnel-coupled to leads. As example, we discussed the transport through a double dot connected in series in Chapter 6. In this system, the tunnel coupling of one dot to one lead each causes a renormalization of the respective energy levels. If the renormalization is different for the left and right dot, the renormalization changes the energy level difference between the two dots. The conductance through a serial double dot depends very sensitively on this energy level difference. Therefore we propose to use a double-dot system as detector for this energy renormalization effects. Especially the stability diagram in the nonlinear transport regime can be used to prove the existence of a tunnel-induced energy level renormalization, which is the origin of the intrinsic dot-spin precession in the quantum-dot spin-valve case.

While the *dc*-conductance depends only on the *time-averaged* spin on the dot, the frequency dependent current-current correlation function is sensitive to the *time-dependent* evolution of the dot spin. Therefore a current noise measurement, as discussed in Chapter 5, can reveal additional informations about the spin in the quantum-dot spin valve. At the Larmor frequency, corresponding to the sum of exchange and external applied field, the single-spin precession leads to a resonance in the noise. Responsible for this features is the tunnel-out process of a dot electron to the drain lead. The tunnel probability depends via tunnel magnetoresistance on the relative angle of dot spin and drain magnetization. Since the magnetization of the lead is fixed, the precession of the dot spin causes an oscillation of the tunnel-out probability, and, as a consequence, leads to current-current correlations. In a quantum-dot system, contacted to ferromagnetic leads, the current-current correlation function gives information about the spin-spin correlation function. Therefore a current-noise measurement serves as an *unorthodox electron-spin-resonance* experiment, measuring a single dot only.

Having in mind the correspondence of charge-charge and spin-spin correlation function in the quantum-dot spin valve, we got interested in Faraday-rotation fluctuation spectroscopy in Chapter 7. Such an experiment measures the frequency-dependent fluctuation of the polarization plane of a laser, transmitted through the sample. These fluctuations

contain information about the spin-spin correlation function of localized electrons within the sample. Measuring the spin noise at a certain noise frequency corresponds to measure the spin state in time intervals, which equal multiples of the inverse frequency. If a spin precess with this specific frequency, one measures the spin always after full revolutions, i.e., one measures the same spin state each time. In other words, the measurements are correlated. Therefore the spin-spin correlation function shows a Lorentzian resonance at the Larmor frequency of the electrons. Thereby the width of the resonance is given by the spin coherence time  $T_2$ . Beside the theoretical explanation of already conducted experiments, we also propose a new way to measure the spin-coherence time  $T_2$  with *reduced inhomogeneous broadening*, namely to measure Faraday-rotation fluctuations in the presence of an oscillating magnetic field. This experiment physically resembles an ESR-pulse setup. However, since Faraday-rotation fluctuation measurements are *continuous-wave* experiments, i.e., they do not need any time or phase resolution, the experimental efforts are significantly reduced, compared to standard ESR-pulse schemes.





# Appendix A

## Green's Functions of the Quantum Dot

For the calculation of the charge as well as of the spin current, the Fourier transformed Keldysh Green's functions

$$\begin{aligned} G_{\sigma\sigma'}^>(t) &= -i\langle c_\sigma(t)c_{\sigma'}^\dagger(0) \rangle \\ G_{\sigma\sigma'}^<(t) &= +i\langle c_{\sigma'}^\dagger(0)c_\sigma(t) \rangle \\ G_{\sigma\sigma'}^{\text{ret}}(t) &= \Theta(t)G_{\sigma\sigma'}^>(t) + \Theta(-t)G_{\sigma\sigma'}^<(t) - G_{\sigma\sigma'}^<(t) \\ G_{\sigma\sigma'}^{\text{adv}}(t) &= (G_{\sigma\sigma'}^{\text{ret}}(t))^* \end{aligned} \tag{A.1}$$

of the quantum-dot states are needed. In this Appendix the detailed derivation of the zeroth order Green's functions is presented. The Green's function is an average of one dot creation and one dot annihilation operator. Since only the zeroth order Green's functions are needed to describe first-order transport one does not need to consider tunneling events at all. However, the result will not be the Green's function of an isolated dot, but the Green's function will depend on the stationary density matrix, which will be affected by tunneling.

In the lesser and greater Keldysh Green's functions, the Fermion operators are not time ordered. Therefore they appear in the same order along the Keldysh time contour, as written in Eq. (A.1), see Fig.A.1. The operator ordering in the not-time ordered expression  $\langle c_\sigma(t)c_{\sigma'}^\dagger(0) \rangle$  is read from right to left, and corresponds to the operator ordering on the Keldysh time contour, which is read from top-left  $\rightarrow$  top-right  $\rightarrow$  bottom-right  $\rightarrow$  bottom-left. The creation (annihilation) operator adds or subtracts an electron from the dot state at the respective time. The dashed line in the diagrams symbolize this particle transfer from one vertex to the other. This particle transfer is due to the Green's function Fermi operators, and not due to tunneling. The spin of the added and removed electron is given by the indices of the Green's function.

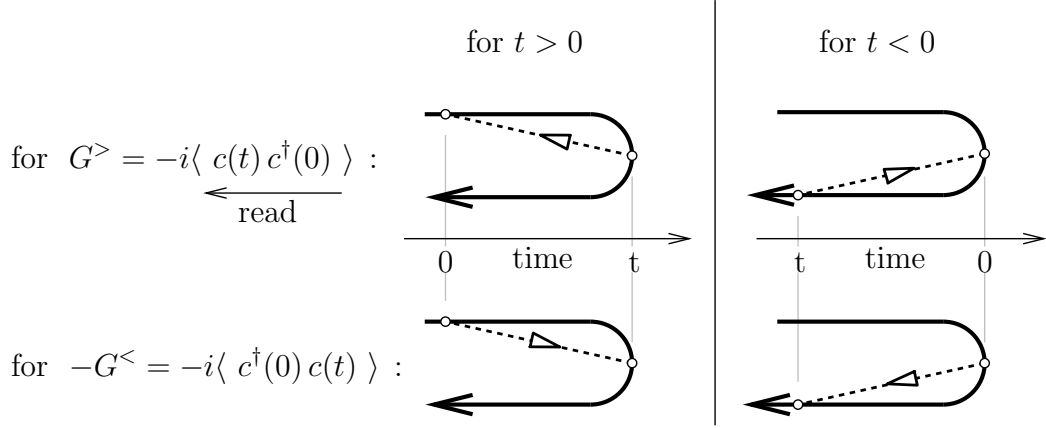


Figure A.1: Sketch of the operator ordering on the Keldysh time line.

From the time contour diagrams in Fig.A.1, the Fourier transformed expressions of the greater and lesser Green's functions can be directly deduced. One must track all possible combinations of initial, intermediate, and final dot states  $\chi = 0, \uparrow, \downarrow, d$ , which are compatible with spin and charge conservation. Each line transports the energy of the respective dot state. In the diagrammatical language, the Fourier transformation has two technical consequences: first,  $\hbar$  times the frequency argument  $\omega$  is assigned to the dashed line between the two vertices, and second, because the time integration runs from  $-\infty$  to  $\infty$ , both diagram types for  $t < 0$  and  $t > 0$  must be added together. Each diagram represents a resolvent  $1/(\Delta E + i0^+)$ , where  $\Delta E$  is the difference between the left- and rightgoing energies including the frequency of the dashed line. The Green's function is the sum of all resolvents, where each resolvent (diagram) is further multiplied by the density matrix element  $P_\chi^\eta$ , where  $\eta$  is the initial dot state, and  $\chi$  the final dot state on the time contour. All diagrams representing the non-time ordered Green's functions are drawn in Fig. A.2.

By replacing the diagrams in Fig. A.2 by the resolvents, and by the use of Cauchy's formula, we get

$$\begin{aligned}
 G_{\sigma\sigma}^>(\omega) &= -2\pi i P_\sigma \delta(\omega - \varepsilon - U) - 2\pi i P_0 \delta(\omega - \varepsilon) \\
 G_{\sigma\sigma}^<(\omega) &= +2\pi i P_\sigma \delta(\omega - \varepsilon) + 2\pi i P_d \delta(\omega - \varepsilon - U) \\
 G_{\sigma\bar{\sigma}}^>(\omega) &= 2\pi i P_{\bar{\sigma}}^\sigma \delta(\omega - \varepsilon - U) \\
 G_{\sigma\bar{\sigma}}^<(\omega) &= 2\pi i P_{\bar{\sigma}}^\sigma \delta(\omega - \varepsilon)
 \end{aligned} \tag{A.2}$$

where  $\sigma \neq \bar{\sigma}$ .

$$\begin{aligned}
G_{\uparrow\downarrow}^{\geq} &= P_{\downarrow}^{\uparrow} \cdot \begin{array}{c} \text{diagram 1} \end{array} + P_{\downarrow}^{\uparrow} \cdot \begin{array}{c} \text{diagram 2} \end{array} \\
G_{\uparrow\downarrow}^{\leq} &= - \left\{ P_{\downarrow}^{\uparrow} \cdot \begin{array}{c} \text{diagram 3} \end{array} + P_{\downarrow}^{\uparrow} \cdot \begin{array}{c} \text{diagram 4} \end{array} \right\} \\
G_{\sigma\sigma}^{\geq} &= P_{\bar{\sigma}}^{\bar{\sigma}} \cdot \begin{array}{c} \text{diagram 5} \end{array} + P_{\bar{\sigma}}^{\bar{\sigma}} \cdot \begin{array}{c} \text{diagram 6} \end{array} \\
&\quad + P_0^0 \cdot \begin{array}{c} \text{diagram 7} \end{array} + P_0^0 \cdot \begin{array}{c} \text{diagram 8} \end{array} \\
G_{\sigma\sigma}^{\leq} &= P_{\sigma}^{\sigma} \cdot \begin{array}{c} \text{diagram 9} \end{array} + P_{\sigma}^{\sigma} \cdot \begin{array}{c} \text{diagram 10} \end{array} \\
&\quad + P_d^d \cdot \begin{array}{c} \text{diagram 11} \end{array} + P_d^d \cdot \begin{array}{c} \text{diagram 12} \end{array}
\end{aligned}$$

Figure A.2: Examples for the diagrams representing the greater and lesser Green's functions.

By the work of Meir and Wingreen, the electrical current can be calculated with these greater and lesser Keldysh Green's functions. The spin current in contrast also depends on the time ordered retarded and advanced Green's functions. With a suitable choice of the spin quantization axes, only the time ordered Green's functions with different spin indices are needed. The time ordered  $G_{\sigma\bar{\sigma}}^{\text{ret}}(\omega)$  and  $G_{\sigma\bar{\sigma}}^{\text{adv}}(\omega)$  can be constructed from the not time ordered lesser and greater Green's functions by  $G^{\text{ret}}(t) = \Theta(t)G^{\geq}(t) - \Theta(t)G^{\leq}(t)$ . By taking the operator ordering on the time contour into account as sketched in Fig. A.1, the retarded Green's function has the diagrammatic representation as shown in Fig. A.3, and has the analytic value of

Figure A.3: Diagrams representing of a time ordered Green's function.

$$G_{\sigma\bar{\sigma}}^{\text{ret}}(\omega) = P_{\bar{\sigma}}^{\sigma} \frac{1}{\omega - e - U + i0^+} + P_{\bar{\sigma}}^{\sigma} \frac{1}{\omega - e + i0^+}. \quad (\text{A.3})$$

# Appendix B

## Generalized Transition Rates for a Quantum-Dot Spin Valve

For the calculation of the self-energy  $W_{\eta\eta'}^{\chi\chi'}$ , the explicit shape of the tunnel Hamiltonian in Eq. (2.1) is needed. Therefore first a reference frame of the dot-spin quantization axis must be defined, which then determines the strength and phase of the spin-dependent tunnel events. Of course, in the end, all physical results must not depend on the choice of the reference frame.

### B.1 Choice of reference frame

In the absence of a magnetic field, it is convenient to choose neither  $\hat{\mathbf{n}}_L$  nor  $\hat{\mathbf{n}}_R$  as quantization axes, but instead to quantize the dot spin  $\sigma = \uparrow, \downarrow$  along the  $z$ -direction of the coordinate system in which the basis vectors  $\hat{\mathbf{e}}_x$ ,  $\hat{\mathbf{e}}_y$ , and  $\hat{\mathbf{e}}_z$  are along  $\hat{\mathbf{n}}_L + \hat{\mathbf{n}}_R$ ,  $\hat{\mathbf{n}}_L - \hat{\mathbf{n}}_R$ , and  $\hat{\mathbf{n}}_R \times \hat{\mathbf{n}}_L$ , respectively, see also Fig. B.1(a). The tunnel Hamiltonian for the left tunneling barrier then reads

$$H_{T,L} = \frac{t_L}{\sqrt{2}} \sum_k a_{Lk+}^\dagger (e^{+i\phi/4} c_\uparrow + e^{-i\phi/4} c_\downarrow) + a_{Lk-}^\dagger (-e^{+i\phi/4} c_\uparrow + e^{-i\phi/4} c_\downarrow) + \text{H.c.} \quad (\text{B.1})$$

and for the right barrier,  $H_{T,R}$ , the same with the replacements  $L \rightarrow R$  and  $\phi \rightarrow -\phi$ . The average tunnel coupling to one lead is then given by  $\Gamma_r = \sum_{\sigma=\pm} 2\pi |t_r/\sqrt{2}|^2 \rho_{r,\sigma} = \sum_{\sigma=\pm} \Gamma_{r,\sigma}/2$ .

While individual parts of the tunnel Hamiltonians do not conserve spin separately, the sum of all parts strictly does. Due to the special choice of the quantization axis, the lead electrons are coupled equally strong to up- and down-spin states in the quantum dot. There are, however, phase factors involved, similar to Aharonov-Bohm phases in multiply connected geometries. The formal similarity of the quantum-dot spin valve to a two-dot Aharonov-Bohm interferometer is visualized in Fig. B.1(b).

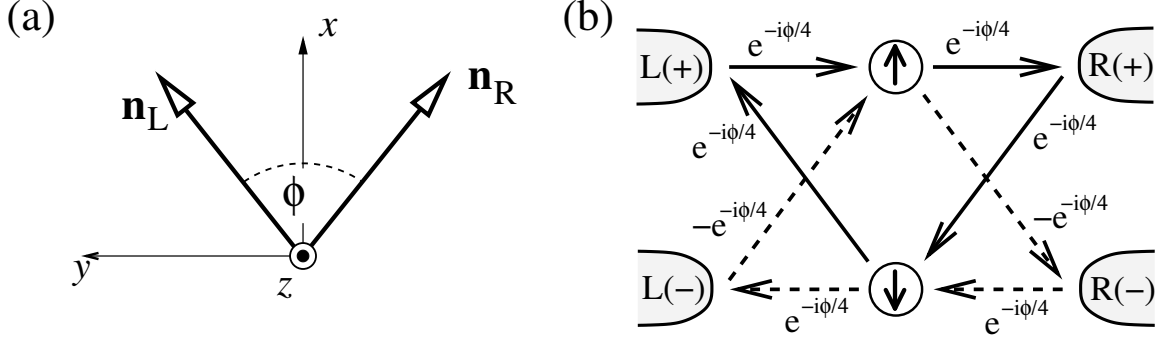


Figure B.1: (a) The chosen coordinate system. The magnetization directions  $\hat{\mathbf{n}}_L$  and  $\hat{\mathbf{n}}_R$  enclose an angle  $\phi$ . (b) Graphical representation of the phase factors in the tunnel Hamiltonian, Eq. (B.1). In this representation, the quantum-dot spin valve bears similarities to an Aharonov-Bohm setup, with the different arms modeling the two different spin channels  $\uparrow$  and  $\downarrow$ . Thereby the Aharonov-Bohm flux corresponds to the relative angle of the lead magnetizations.

## B.2 Diagrammatic calculation of the matrix $W$

The self-energy  $W_{\eta\eta'}^{\chi\chi'}$  can be represented as a block diagram, which is a part of a Keldysh time contour. Examples of first-order diagrams are shown in Fig. B.2. The real-time axis runs horizontally from the left to the right while the upper (lower) line represents the forward (backward) propagator of the dot state  $\chi, \eta = \{0, \uparrow, \downarrow, d\}$ . Note, that the indices of the  $W$ 's are reversed in comparison to the diagram corners.

In the here presented work, only the lowest order transport is considered. Therefore, the transition rates  $\mathbf{W}$  include only processes, which include the transfer of one electron, i.e., the diagrams have only one tunnel line. These types of diagrams can be constructed by the following rules:

1. Draw all topologically different diagrams with one tunneling line connecting two vertices on either the same or opposite propagators. Assign the states  $\chi = 0, \uparrow, \downarrow, d$  to the four corners, and the corresponding energies  $\varepsilon_\chi$  to all propagators, as well as an energy  $\omega$  to the tunneling line.
2. For the time interval on the real axis confined by two neighboring vertices, assign the resolvent  $-i/(\Delta E + i0^+)$ , where  $\Delta E$  is the energy difference between left and right going tunnel lines and propagators.
3. For each vertex connecting a double-occupied state  $d$  to the up state  $\uparrow$ , the diagram acquires a prefactor of  $(-1)$ .

$$\begin{aligned}
W_{\downarrow 0}^{\uparrow 0} &= \begin{array}{c} \begin{array}{cc} 0 & \xrightarrow{\quad} \uparrow \\ \text{(\downarrow)} & \nearrow \text{(\uparrow)} \\ 0 & \xrightarrow{\quad} \downarrow \end{array} + \begin{array}{cc} 0 & \xrightarrow{\quad} \uparrow \\ \text{(\uparrow)} & \nearrow \text{(\downarrow)} \\ 0 & \xrightarrow{\quad} \downarrow \end{array} \end{array} \\
W_{dd}^{dd} &= \sum_{\sigma} \left\{ \begin{array}{cc} d & \xrightarrow{\sigma} d \\ & \searrow \bar{\sigma} \\ d & \xrightarrow{\quad} d \end{array} + \begin{array}{cc} d & \xrightarrow{\quad} d \\ & \searrow \bar{\sigma} \\ d & \xrightarrow{\sigma} d \end{array} \right\} \\
W_{\downarrow \uparrow}^{\uparrow \uparrow} &= \begin{array}{c} \begin{array}{cc} \uparrow & \xrightarrow{0} \downarrow \\ \text{(\uparrow)} & \searrow \text{(\downarrow)} \\ \uparrow & \xrightarrow{\quad} \uparrow \end{array} + \begin{array}{cc} \uparrow & \xrightarrow{d} \downarrow \\ \text{(\downarrow)} & \searrow \text{(\uparrow)} \\ \uparrow & \xrightarrow{\quad} \uparrow \end{array} \end{array}
\end{aligned}$$

Figure B.2: Examples for the diagrams representing the generalized transition rates  $\mathbf{W}$ .

4. Assign to each tunneling line the factor  $\gamma_{\sigma\sigma'}^+(\omega)$  [ $\gamma_{\sigma\sigma'}^-(\omega)$ ] when the tunneling line is going backward (forward) with respect to the Keldysh contour. The factors  $\gamma^{\pm}(\omega)$  come from the contraction of two lead operators in the tunnel Hamiltonian and resemble the transition rates predicted by Fermi's golden rule, including a sum over all intermediate lead states ( $r = R/L, \sigma = +/-$ ). Dependent on the time ordering, the transition rate is proportional to the electron  $f^+$  or the hole distribution function  $f^- = 1 - f^+$ . With the relative phases extracted from Fig. B.1, the  $\gamma$ 's read

$$\gamma_{\sigma\sigma}^{\pm}(\omega) = \frac{1}{2\pi} \sum_{r,\chi=\pm} \frac{\Gamma_{r\chi}}{2} f_r^{\pm}(\omega), \quad (\text{B.2})$$

$$\begin{aligned}
\gamma_{\uparrow\downarrow}^{\pm}(\omega) &= \frac{1}{4\pi} (\Gamma_{L+} f_L^{\pm} e^{i\phi/2} + \Gamma_{R+} f_R^{\pm} e^{-i\phi/2} \\
&\quad - \Gamma_{L-} f_L^{\pm} e^{i\phi/2} - \Gamma_{R-} f_R^{\pm} e^{-i\phi/2}) = \gamma_{\downarrow\uparrow}^{\pm*}(\omega). \quad (\text{B.3})
\end{aligned}$$

Here,  $\sigma$  and  $\sigma'$  are the spins of the electron that leaves and enters the vertices connected by the line. Due to the choice of the spin quantization axes, the spin indices do not need to be equal, but still the theory assumes strict spin conservation.

5. The diagram gets a prefactor of  $(-1)^b$ , where  $b$  is number of internal vertices on the backward propagator.
6. Integrate over the energy  $\omega$  of the tunneling lines. This integral can be calculated trivially by using Cauchy's formula.

Arranged in the matrix notation introduced in Section 5.2.5 we get

$$\mathbf{W}|_{\omega=0} = \Gamma_L \mathbf{A}_L + (L \rightarrow R), \quad (\text{B.4})$$

with the matrix  $\mathbf{A}_L$  given by

$$\begin{pmatrix} -2f_L^+(\varepsilon) & f_L^-(\varepsilon) & f_L^-(\varepsilon) & 0 & pf_L^-(\varepsilon)e^{i\phi_L} & pf_L^-(\varepsilon)e^{-i\phi_L} \\ f_L^+(\varepsilon) & -y_L & 0 & f_L^-(\varepsilon+U) & -\frac{p}{2}(x_L - i\alpha_L)e^{i\phi_L} & -\frac{p}{2}(x_L + i\alpha_L)e^{-i\phi_L} \\ f_L^+(\varepsilon) & 0 & -y_L & f_L^-(\varepsilon+U) & -\frac{p}{2}(x_L + i\alpha_L)e^{i\phi_L} & -\frac{p}{2}(x_L - i\alpha_L)e^{-i\phi_L} \\ 0 & f_L^+(\varepsilon+U) & f_L^+(\varepsilon+U) & -2f_L^-(\varepsilon+U) & -pf_L^+(\varepsilon+U)e^{i\phi_L} & -pf_L^+(\varepsilon+U)e^{-i\phi_L} \\ pf_L^+(\varepsilon)e^{-i\phi_L} & -\frac{p}{2}(x_L - i\alpha_L)e^{-i\phi_L} & -\frac{p}{2}(x_L + i\alpha_L)e^{-i\phi_L} & pf_L^-(\varepsilon+U)e^{-i\phi_L} & -y_L & 0 \\ pf_L^+(\varepsilon)e^{+i\phi_L} & -\frac{p}{2}(x_L + i\alpha_L)e^{i\phi_L} & -\frac{p}{2}(x_L - i\alpha_L)e^{i\phi_L} & pf_L^-(\varepsilon+U)e^{+i\phi_L} & 0 & -y_L \end{pmatrix}.$$

The angle  $\phi = 2\phi_L = -2\phi_R$  is the angle enclosed by the lead magnetizations. The leads are characterized by the Fermi functions  $f_r^+(\omega)$  and  $f_r^- = 1 - f_r^+$ . For shorter notation we further introduce  $x_L = f_L^-(\varepsilon) - f_L^+(\varepsilon + U)$  and  $y_L = f_L^-(\varepsilon) + f_L^+(\varepsilon + U)$ . The exchange field strength is then given by  $|B_r| = \Gamma_r p \alpha_r$ , see Eq. (5.15).

This approach to construct the master equation for the quantum-dot spin valve of course reproduce the results gained from balancing spin and charge currents, as presented in Chapter 3.



# Appendix C

## Master Equations for the Double-Dot Problem

With the definition  $P_{\chi_2}^{\chi_1} := \langle \chi_1 | \boldsymbol{\rho}_{\text{st}} | \chi_2 \rangle$ , the master equation Eq. (6.5) can be written as:

$$0 = i\hbar \frac{d}{dt} P_{\chi_2}^{\chi_1} = \langle \chi_1 | [H_{\text{Dots}}, \boldsymbol{\rho}_{\text{st}}] | \chi_2 \rangle + \langle \chi_1 | [H_{\Delta}, \boldsymbol{\rho}_{\text{st}}] | \chi_2 \rangle + i \sum_{\chi_3, \chi_4} W_{\chi_2 \chi_4}^{\chi_1 \chi_3} P_{\chi_4}^{\chi_3}. \quad (\text{C.1})$$

In the following the tensor  $W_{\chi_4 \chi_2}^{\chi_3 \chi_1}$  is calculated in the basis of localized eigenstates of  $H_{\text{Dots}}$ , i.e.,  $\chi_i \in \{|0\rangle, |L\sigma\rangle, |R\sigma\rangle, |L\sigma R\sigma'\rangle\}$ , including the spin degree of freedom.

### C.1 Diagrammatic rules

Within the diagrammatical approach, the tensor  $W_{\chi_4 \chi_2}^{\chi_3 \chi_1}$  is represented as block diagram, which is a part of the Keldysh time contour as shown in Fig. C.1. The upper and lower line of the Keldysh time contour  $t_K$  represent the propagation of the double-dot system forward and backward in time. They connect the matrix element characterized by the labels on the left side with the matrix element characterized by the labels on the right side. In the sequential-tunnel approximation all transitions are allowed where a single electron first leaves and then re-enters the double dot or vice versa. The two tunnel Hamiltonians are represented by vertices on the propagators. These vertices are connected by the contraction of the lead Fermi operators (indicated by a dashed line). Each line is characterized by its energy  $\omega$ , the spin  $\sigma$  of the transferred electron, as well as the corresponding reservoir label  $r \in \{L, R\}$ . A vertex with an outgoing (incoming) tunneling line represents an electron leaving (entering) the double dot on the specified side  $r$ . All possible transitions in lowest order in the external coupling  $\Gamma$  belong to one of the eight diagrams depicted in Fig. C.2.

The tensor  $W_{\chi_4 \chi_2}^{\chi_3 \chi_1}$  is given by the sum of all diagrams with the corresponding eigenstates at the four corners, see Fig. C.2. The number of relevant diagrams is limited by spin and

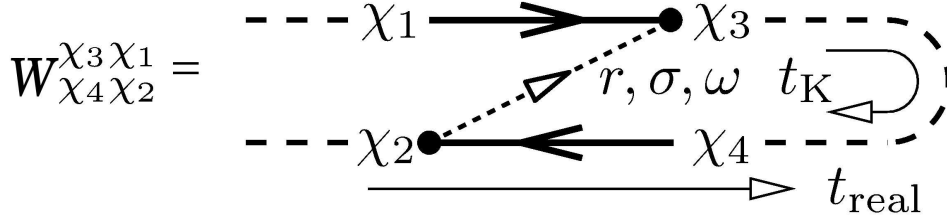


Figure C.1: Sketch of the time contour structure of a diagram. The upper (lower) horizontal line denotes the forward (backward) propagator of the double-dot system. The Keldysh time contour is labeled by  $t_K$ , while the real time runs from left to right.

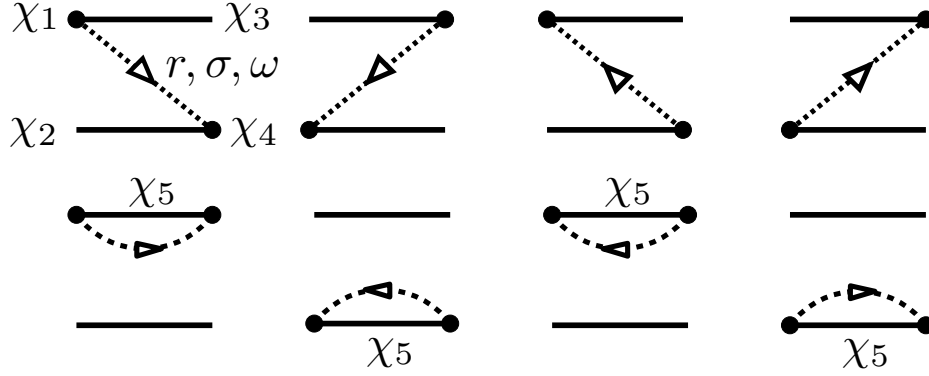


Figure C.2: All topologically different diagrams contributing to the tensor  $W_{\chi_4\chi_2}^{\chi_3\chi_1}$  calculated in first order in the external coupling  $\Gamma$ . Labeling of the eigenstates at the four corners and of the tunneling line like in first diagram.  $\chi_5$  labels an intermediate charge state of the double dot.

particle number conservation as well as to the serial system geometry. The rules to evaluate these diagrams in lowest order are:

1. Draw the upper and lower time contour. Add two tunnel vertices in any topological different way. The relevant criteria are the upper and lower contour, and the time ordering of the vertices on the real axes (from left to right), not only on the Keldysh time contour. Assign to each free segment of the contour a state of the double dot and the corresponding energy. For 'bubble' diagrams like in the lower row of Fig. C.2, an intermediate state  $\chi_5$  participates.
2. The two vertices are connected by a tunnel line. Each tunnel line is labeled with the energy of the tunneling electron  $\omega$ , its reservoir label  $r$  and its spin  $\sigma$ . Spin and reservoir label of the tunneling electron are uniquely determined by the eigenstates involved in the tunneling processes.

3. Assign to each diagram the resolvent  $-i/(\Delta E + i0^+)$  where  $\Delta E$  is the difference between energies belonging to left going lines and energies belonging to right going lines (the tunneling line as well as the propagators).
4. The tunneling line connecting two vertices and labeled by the reservoir index  $r$  gives rise to the factor

$$\gamma_r^\pm(\omega) = \frac{1}{2\pi} \Gamma_r f_r^\pm(\omega)$$

Here, the Fermi function  $f_r^+(\omega) = f_r(\omega) = 1/(1 + \exp[(\omega - \mu_r)/k_B T])$  corresponds to a tunneling line that is backward directed in the Keldysh time ordering (compare Fig. C.1), and  $f_r^-(\omega) = 1 - f_r(\omega)$  corresponds to a tunneling line forward directed in the Keldysh time ordering.

5. Each diagram gets a prefactor  $(-1)^v$  where  $v$  is the number of vertices on the backward propagator. (This rule generates a  $(-1)$  for the diagrams in the upper row of Fig. C.2.)
6. Sum over possible internal eigenstates  $\chi_5$  and integrate over the energy  $\omega$  of the tunneling electron.

In the parameter regime we are interested in, the following relations hold:  $kT > \Gamma \geq \varepsilon, \Delta$ . Therefore the energy difference between the single particle states is not resolved by the Fermi functions in the reservoir, so that we have to approximate the eigenenergies of  $\{|0\rangle, |L\sigma\rangle, |R\sigma\rangle, |L\sigma R\sigma'\rangle\}$  by  $\{0, E_L \approx E_R \approx \bar{E}, 2\bar{E} + U\}$ . While a double occupation of a single dot for the initial or final states is excluded by setting  $f_r(\bar{E} + U') = 0$ , the intermediate state  $\chi_5$  is allowed to be such a state. These states have the eigenenergy  $2\bar{E} + U'$ .

In Fig. C.3, the diagrammatic expansion of the tensor elements  $W_{L\sigma,0}^{L\sigma,0}$  and  $W_{R\sigma,R\sigma}^{L\sigma,L\sigma}$  are shown.  $W_{L\sigma,0}^{L\sigma,0}$  is purely real and its magnitude has the meaning of a transition rate for a tunneling-in process starting from the empty double dot and resulting in a single electron with spin  $\sigma$  sitting in the left dot. In contrast,  $W_{R\sigma,R\sigma}^{L\sigma,L\sigma}$  also has an imaginary part which renormalizes the energy levels. Calculated in lowest order in  $\Gamma$ , each element of the tensor  $\mathbf{W}$  can be expressed by terms of the form

$$X_r^{(n,m)}(E) = \int d\omega \frac{-i \gamma_r^n(\omega)}{m(E - \omega) + i0^+}, \quad (\text{C.2})$$

where  $n$  and  $m$  are either  $(-)$  or  $(+)$ . In this notation, the algebraic expression for  $W_{R\sigma,R\sigma}^{L\sigma,L\sigma}$  is:

$$\begin{aligned} W_{R\sigma,R\sigma}^{L\sigma,L\sigma} = & X_r^{(-,+)}(\bar{E}) + X_r^{(-,-)}(\bar{E}) + g_\sigma (X_r^{(+,+)}(\bar{E} + U) + X_r^{(+,-)}(\bar{E} + U)) \\ & + (g_\sigma - 1) (X_r^{(+,+)}(\bar{E} + U') + X_r^{(+,-)}(\bar{E} + U')) , \end{aligned} \quad (\text{C.3})$$

where, within this Appendix, we allow for an arbitrary spin degeneracy  $g_\sigma$ . Since  $f_r(\bar{E} + U') = 0$  the real part of the last row in Eq. (C.3) vanishes, however this is not the case

Figure C.3: Relevant diagrams contributing to two specific entries of  $\mathbf{W}$ , in a lowest order expansion in  $\Gamma$ . Every diagram corresponding to a specific entry is labeled by the same eigenstates at its four corners.

for the imaginary part, which causes the level renormalization. The imaginary part of the diagrams is determined by the principal value of the integrals in Eq. (C.2) and can be expressed as a sum over digamma functions, see Eq. (6.9).

## C.2 System of master equations

Since the Hamiltonian given in Eq. (6.1) is independent of the orientation of the spin, each spin-realization of a charge state is equally probable. Therefore one can define  $P_0 = \langle 0 | \rho_{\text{st}} | 0 \rangle$ ,  $P_{\text{r}}^{\text{r}} = \sum_{\sigma} \langle \text{r} \sigma | \rho_{\text{st}} | \text{r}' \sigma \rangle$ , and  $P_2 = \sum_{\sigma, \sigma'} \langle \text{L} \sigma \text{R} \sigma' | \rho_{\text{st}} | \text{L} \sigma \text{R} \sigma' \rangle$ . Furthermore the stationary density matrix is diagonal in spin and particle number. Thus the reduced density matrix  $\rho_{\text{st}}$  describing the double dot is given by the  $4 \times 4$  matrix

$$\rho_{\text{st}} = \begin{pmatrix} P_0 & 0 & 0 & 0 \\ 0 & P_{\text{L}}^{\text{L}} & P_{\text{R}}^{\text{L}} & 0 \\ 0 & P_{\text{L}}^{\text{R}} & P_{\text{R}}^{\text{R}} & 0 \\ 0 & 0 & 0 & P_2 \end{pmatrix}. \quad (\text{C.4})$$

The diagonal elements of the density matrix are the probabilities to find the double dot empty ( $P_0$ ), the left ( $P_{\text{L}}^{\text{L}}$ ) or right dot ( $P_{\text{R}}^{\text{R}}$ ) singly occupied, or the two dots simultaneously occupied by one electron ( $P_2$ ). Superpositions of the two single occupied states are possible  $P_{\text{R}}^{\text{L}} = (P_{\text{L}}^{\text{R}})^*$ .

One can define an effective tensor for  $\mathbf{W}$ , that only depends on the orbital part of the matrix elements (denoted in the following formula by  $\chi_1, \chi_2, \chi_3, \chi_4$ ) and no longer on the spin variables. The new tensor elements are defined by:

$$W_{\chi_4 \chi_2}^{\chi_3 \chi_1} = \sum_f W_{\chi_4^f \chi_2^f}^{\chi_3^f \chi_1^f} \quad (\text{C.5})$$

Here  $i$  labels any possible spin-realization for the initial states,  $\chi_1, \chi_2$ , and  $f$  for the final states  $\chi_3, \chi_4$ . (Due to spin degeneracies the two particle states are four fold degenerate, and the left and right states are each two-fold degenerate.) The tunnel tensor  $W_{\chi_4 \chi_2}^{\chi_3 \chi_1}$  is independent of the spin-realization  $i$ . The spin degeneracy appears only as a prefactor, but does not change the functional form of the elements. For example,  $W_{\text{L},0}^{\text{L},0} = \sum_{\sigma} W_{\text{L},0}^{\text{L}\sigma,0}$  describing the transition from  $P_0$  to  $P_{\text{L}}$  is twice as big for spin-degenerate electrons as for spin-less fermions. On the other hand  $W_{\text{L},\text{L}}^{\text{L},\text{L}} = W_{\text{L}\uparrow, \text{L}\uparrow}^{\text{L}\uparrow, \text{L}\uparrow} + W_{\text{L}\downarrow, \text{L}\uparrow}^{\text{L}\downarrow, \text{L}\uparrow} = W_{\text{L}\downarrow, \text{L}\downarrow}^{\text{L}\downarrow, \text{L}\downarrow} + W_{\text{L}\uparrow, \text{L}\downarrow}^{\text{L}\uparrow, \text{L}\downarrow}$  describing the loss term of  $P_{\text{L}}$  is the same for spin-degenerate or spin-less fermions since  $W_{\text{L}\downarrow, \text{L}\uparrow}^{\text{L}\downarrow, \text{L}\uparrow} = 0 = W_{\text{L}\uparrow, \text{L}\downarrow}^{\text{L}\uparrow, \text{L}\downarrow}$ .

This treatment of the spin allows a general solution of the problem including both, the case of spin polarized electrons and the case of spin degenerate electrons. For the interested reader, we specify the degeneracy of Fermions in the further Appendix by the variable  $g_{\sigma}$ :  $g_{\sigma} = 2$  for electrons,  $g_{\sigma} = 1$  for spin-less Fermions.

Instead of working with off-diagonal density matrix elements, a pseudo spin representation can be used. As any two level system, the  $2 \times 2$  hermitian submatrix of the singly occupied states in Eq. (C.4) can be treated as  $SU(2)$  representation of the pseudo spin Bloch vector  $\mathbf{I} = (P_{\text{R}}^{\text{L}} + P_{\text{L}}^{\text{R}}, iP_{\text{R}}^{\text{L}} - iP_{\text{L}}^{\text{R}}, P_{\text{L}}^{\text{L}} - P_{\text{R}}^{\text{R}})^T/2$ . For a complete set of variables, the variable  $P_1 = P_{\text{L}}^{\text{L}} + P_{\text{R}}^{\text{R}}$ , the probability of a singly-occupied double dot, is introduced.

With this change of variables, the dynamics of the double dot system can be mapped on the motion of a spin in an external magnetic field. This is in close analogy to the dynamics of a quantum dot connected to ferromagnetic leads, see Chapter 3.

Due to the serial geometry the external tunneling affects only the z-direction of the pseudo spin and the left and right contacts couple with a different sign to  $I_z$ . This is captured by the definitions  $\hat{\mathbf{n}}_L = (0, 0, 1)$  and  $\hat{\mathbf{n}}_R = (0, 0, -1)$ , which can be understood as pseudo-spin magnetizations of the leads. With this definitions the occupation probabilities obey the following master equations:

$$0 = \frac{d}{dt}P_0 = \sum_r \frac{\Gamma_r}{\hbar} (-g_\sigma f_r(\bar{E})P_0 + \frac{1}{2}f_r^-(\bar{E})P_1) + \sum_r \frac{\Gamma_r}{\hbar} f_r^-(\bar{E})\hat{\mathbf{n}}_r \cdot \mathbf{I} \quad (\text{C.6})$$

$$0 = \frac{d}{dt}P_2 = \sum_r \frac{\Gamma_r}{\hbar} (\frac{g_\sigma}{2}f_r(\bar{E} + U)P_1 - f_r^-(\bar{E} + U)P_2) - \sum_r \frac{\Gamma_r}{\hbar} g_\sigma f_r(\bar{E} + U)\hat{\mathbf{n}}_r \cdot \mathbf{I} \quad (\text{C.7})$$

$$P_1 = 1 - P_0 - P_2 \quad (\text{C.8})$$

In equilibrium ( $f_R = f_L$ ) the diagonal matrix elements are given by the Boltzmann statistics  $P_0 = 1/Z$ ,  $P_1 = 2g_\sigma \exp[-\bar{E}/k_B T]/Z$ ,  $P_2 = g_\sigma^2 \exp[-(\bar{E} + U)/k_B T]/Z$ ,  $Z = P_0 + P_1 + P_2$  and the accumulation term as well as all components of the pseudo spin vanish.

The dynamics of the single particle state is described by a Bloch-like equation:

$$0 = \frac{d}{dt}\mathbf{I} = \left(\frac{d\mathbf{I}}{dt}\right)_{\text{acc.}} - \left(\frac{d\mathbf{I}}{dt}\right)_{\text{rel.}} + \frac{1}{\hbar}(\mathbf{B} \times \mathbf{I}) \quad (\text{C.9})$$

Three different terms can be identified in the Bloch equation. The term

$$\left(\frac{d\mathbf{I}}{dt}\right)_{\text{acc.}} = \sum_r \hat{\mathbf{n}}_r \frac{\Gamma_r}{2\hbar} [g_\sigma f_r(\bar{E})P_0 + \frac{1}{2}(g_\sigma f_r(\bar{E} + U) - f_r^-(\bar{E}))P_1 - f_r^-(\bar{E} + U)P_2]$$

describes the accumulation of pseudo spin in z-direction due to the serial external coupling. The relaxation-like term

$$\left(\frac{d\mathbf{I}}{dt}\right)_{\text{rel.}} = \frac{1}{2} \sum_r \frac{\Gamma_r}{\hbar} (f_r^-(\bar{E}) + g_\sigma f_r(\bar{E} + U)) \mathbf{I}$$

limits the amount of pseudo spin. The isospin  $\mathbf{I}$  relaxes isotropic by electrons leaving or entering the singly occupied double dot destroying all pseudo-spin components.

The third term looks like a rotation of the pseudo spin around a fictitious magnetic field  $\mathbf{B} = (-\Delta, 0, \varepsilon_{\text{ren}})$ , where  $\varepsilon_{\text{ren}}$  denotes the renormalized level separation

$$\varepsilon_{\text{ren}} = E_L - \text{Re} \left[ X_L^{(-,-)}(\bar{E}) + g_\sigma X_L^{(+,-)}(\bar{E} + U) - (g_\sigma - 1) X_L^{(+,-)}(\bar{E} + U') \right] - (L \rightarrow R), \quad (\text{C.10})$$

where  $\text{Re}$  denotes the real part. The Cauchy principal value integrals are defined in Eq. (C.2). This third term describes coherent oscillations inside the double dot which

mix the accumulated spin in  $z$ -direction with the other components. The inter-dot tunneling characterized by  $\Delta$  yields a precession of the isospin around the  $x$ -axis, while the energy separation between the dot levels results in a rotation around the  $z$ -axis. It is important to note that the renormalized level separation between the dots changes due to the external coupling and it is not given by the bare level separation  $\varepsilon$ .

This system of master equations can be solved analytically, and the thereby gained density matrix determines the conductance of the double-dot device.





## Appendix D

### Calculation of the Spin-Spin Correlation Function

In the calculation of the spin-spin correlation function in an oscillating magnetic field, see Chapter 7, following integral appears:

$$\frac{1}{2\pi} \int_0^{2\pi} d\phi \int_0^\infty dt e^{-t/T_2 - i\omega t - i\frac{\Delta}{\gamma} [\cos(\gamma t + \phi) - \cos(\phi)]}. \quad (\text{D.1})$$

With the Jacobi-Anger Expansion (see Abramowitz & Stegun, 1972, page 361 )

$$e^{i\frac{\Delta}{\gamma} \cos(\gamma t + \phi)} = \sum_{n=-\infty}^{\infty} i^n J_n \left( \frac{\Delta}{\gamma} \right) e^{in(\gamma t + \phi)} \quad (\text{D.2})$$

the time and the phase integration can be separated to

$$\sum_{n=-\infty}^{\infty} i^n J_n \left( -\frac{\Delta}{\gamma} \right) \frac{1}{2\pi} \int_0^{2\pi} d\phi e^{+i\frac{\Delta}{\gamma} \cos(\phi)} e^{in\phi} \int_0^\infty dt e^{-t/T_2 - i\omega t} e^{in\gamma t}, \quad (\text{D.3})$$

while Bessel functions of the first kind were introduced. In this form, the time integration can be easily performed. The phase integration on the other side now resembles just the intergal representation of the Bessel function

$$J_n \left( \frac{\Delta}{\gamma} \right) = \frac{1}{2\pi i^n} \int_0^{2\pi} d\phi e^{+i\frac{\Delta}{\gamma} \cos(\phi)} e^{in\phi}. \quad (\text{D.4})$$

The original integral therefore equals

$$\sum_{n=-\infty}^{\infty} i^{2n} J_n \left( \frac{\Delta}{\gamma} \right) J_n \left( -\frac{\Delta}{\gamma} \right) \frac{1}{1/T_2 + i(\omega - n\gamma)}. \quad (\text{D.5})$$

With the identities  $i^{2n} = (-1)^n$ , and  $J_n(-x) = (-1)^n J_n(x)$ , the final result is given by

$$\sum_{n=-\infty}^{\infty} J_n \left( \frac{\Delta}{\gamma} \right)^2 \frac{T_2}{1 + iT_2(\omega - n\gamma)}. \quad (\text{D.6})$$



# Bibliography

- [1] C. W. Beenakker, Phys. Rev. B **44**, 1646 (1991).
- [2] D. V. Averin, A. N. Korotkov, and K. K. Likharev, Phys Rev. B **44**, 6199 (1991).
- [3] L. I. Glazman and K. A. Matveev, Pis'ma Zh. Eksp. Fiz. **48**, 403 (1988) [JETP Lett. **48**, 445 (1988)].
- [4] T. A. Fulton and G. J. Dolan, Phys. Rev. Lett. **59**, 109 (1987).
- [5] J. H. F. Scott-Thomas, S. B. Field, M. A. Kastner, H. I. Smith, and D. A. Antoniadis, Phys. Rev. Lett. **62**, 583 (1989).
- [6] For reviews see:
  - M. A. Kastner, Rev. Mod. Phys. **64**, 849 (1992).
  - L. P. Kouwenhoven, D. G. Austing, and S. Tarucha, Rep. Prog. Phys. **64**, 701 (2001).
  - *Mesoscopic Electron Transport*, edited by L. L. Sohn, L. P. Kouwenhoven, and G. Schön, (Kluwer, Dordrecht, The Netherlands, 1997).
  - R. C. Ashoori, Nature **379**, 413 (1996).
  - *Single Charge Tunneling*, NATO ASI Series **294**, edited by H. Grabert and M. H. Devoret, (Plenum Press, New York, 1992).
  - D.V. Averin, K.K. Likharev in *Mesoscopic Phenomenon in Solids*, edited by B. L. Altshuler, P. A. Lee, and R. A. Webb (Amsterdam, North-Holland, 1991).
- [7] G. Prinz, Science **282**, 1660 (1998).
- [8] S. A. Wolf, D. D. Awschalom, R. A. Buhrman, J. M. Daughton, S. von Molnár, M. L. Roukes, A. Y. Chtchelkanova, and D. M. Treger, Science, **294**, 1488-1495 (2001).
- [9] I. Zutic, J. Fabian, and S. Das Sarma, Rev. Mod. Phys. **76**, 323 (2004).
- [10] M. N. Baibich, J. M. Broto, A. Fert, F. Nguyen Van Dau, F. Petroff, P. Etienne, G. Creuzet, A. Friederich, and J. Chazelas, Phys. Rev. Lett. **61**, 2472 (1988).

- [11] G. Binasch, P. Grünberg, F. Saurenbach, and W. Zinn, *Phys. Rev. B* **39**, 4828 (1989).
- [12] M. Jullière, *Phys. Lett. A* **54**, 225 (1975).
- [13] S. S. P. Parkin, X. Jiang, C. Kaiser, A. Panchula, K. Roche, and M. Samant, *Proc. IEEE* **91**, 661 (2003).
- [14] S. Tehrani, B. Engel, J. M. Slaughter, E. Chen, M. DeHerrera, M. Durlam, P. Naji, R. Whig, J. Janesky, and J. Calder, *IEEE Trans. Magn.* **36**, 2752 (2000).
- [15] S. Maekawa and U. Gäßvert, *IEEE Trans. Magn.* **18**, 707 (1982).
- [16] T. Miyazaki and N. Tezuka, *J. Mag. Magn. Mater.* **139**, L231 (1995).
- [17] J. S. Moodera, L. R. Kinder, T. M. Wong, and R. Meservey, *Phys. Rev. Lett.* **74**, 3273 (1995).
- [18] J. C. Slonczewski, *Phys. Rev. B* **39**, 6995 (1989).
- [19] J. S. Moodera and L. R. Kinder, *J. Appl. Phys.* **79**, 4724 (1996).
- [20] H. Jaffrès, D. Lacour, F. Nguyen Van Dau, J. Briatico, F. Petroff, and A. Vaurès, *Phys. Rev. B* **64**, 064427 (2001).
- [21] A. Brataas, G. E. W. Bauer, and P. J. Kelly, cond-mat/0602151.
- [22] A. Fert and I. A. Campbell, *Phys. Rev. Lett.* **21**, 1190 (1968).
- [23] T. Valet and A. Fert, *Phys. Rev. B* **48**, 7099 (1993).
- [24] M. Johnson and R. H. Silsbee, *Phys. Rev. Lett.* **55**, 1790 (1985); *Phys. Rev. B* **37**, 5326 (1988).
- [25] F. J. Jedema, H. B. Heersche, A. T. Filip, J. J. A. Baselmans and B. J. van Wees, *Nature* **416**, 713 (2002).
- [26] W. Rudziński and J. Barnaś, *Phys. Rev. B* **64**, 085318 (2001).
- [27] G. Usaj and H. U. Baranger, *Phys. Rev. B* **63**, 184418 (2001).
- [28] A. Cottet, W. Belzig, and C. Bruder, *Phys. Rev. Lett.* **92**, 206801 (2004); A. Cottet and W. Belzig, *Europhys. Lett.* **66**, 405 (2004); A. Cottet, W. Belzig, and C. Bruder, *Phys. Rev. B* **70**, 115315 (2004).
- [29] S. Braig and P. W. Brouwer, *Phys. Rev. B* **71**, 195324 (2005).
- [30] J. Barnaś and A. Fert, *Phys. Rev. Lett.* **80**, 1058 (1998).
- [31] S. Takahashi and S. Maekawa, *Phys. Rev. Lett.* **80**, 1758 (1998).

- [32] A. Brataas, Yu. V. Nazarov, J. Inoue, and G. E. W. Bauer, *Phys. Rev. B* **59**, 93 (1999).
- [33] J. Barnaś, J. Martinek, G. Michałek, B. R. Bułka, and A. Fert, *Phys. Rev. B* **62**, 12363 (2000).
- [34] J. Martinek, J. Barnaś, S. Maekawa, H. Schoeller, and G. Schön, *Phys. Rev. B* **66**, 014402 (2002).
- [35] B. G. Wang, J. Wang, and H. Guo, *J. Phys. Soc. Jpn.* **70**, 2645 (2001); N. Sergueev, Q. F. Sun, H. Guo, B. G. Wang, and J. Wang, *Phys. Rev. B* **65**, 165303 (2002).
- [36] J. König and J. Martinek, *Phys. Rev. Lett.* **90**, 166602 (2003).
- [37] P. W. Anderson, *Phys. Rev.* **124**, 41 (1961).
- [38] I. Weymann, J. Barnas, J. König, J. Martinek, and G. Schön, *Phys. Rev. B* **72**, 113301 (2005); I. Weymann, J. König, J. Martinek, J. Barnas, and G. Schön, *Phys. Rev. B* **72**, 115334 (2005).
- [39] J. Martinek, Y. Utsumi, H. Imamura, J. Barnaś, S. Maekawa, J. König, and G. Schön, *Phys. Rev. Lett.* **91**, 127203 (2003); J. Martinek, M. Sindel, L. Borda, J. Barnaś, J. König, G. Schön, and J. von Delft, *Phys. Rev. Lett.* **91**, 247202 (2003).
- [40] K. A. Matveev, *Sov. Phys. JETP* **72**, 892 (1991).
- [41] Y. Chye, M. E. White, E. Johnston-Halperin, B. D. Gerardot, D. D. Awschalom, and P. M. Petroff, *Phys. Rev. B* **66**, 201301(R) (2002).
- [42] K. Ono, H. Shimada, and Y. Ootuka, *J. Phys. Soc. Jpn.* **66**, 1261 (1997).
- [43] M. Zaffalon and B. J. van Wees, *Phys. Rev. Lett.* **91**, 186601 (2003).
- [44] L. Y. Zhang, C. Y. Wang, Y. G. Wei, X. Y. Liu, and D. Davidović, *Phys. Rev. B* **72**, 155445 (2005).
- [45] L. F. Schelp, A. Fert, F. Fettar, P. Holody, S. F. Lee, J. L. Maurice, F. Petroff, and A. Vaurés, *Phys. Rev. B* **56**, R5747 (1997).
- [46] K. Yakushiji, S. Mitani, K. Takanashi, S. Takahashi, S. Maekawa, H. Imamura, and H. Fujimori, *Appl. Phys. Lett.* **78**, 515 (2001).
- [47] K. Yakushiji, F. Ernuly, H. Imamura, K. Yamane, S. Mitani, K. Takanashi, S. Takahashi, S. Maekawa, and H. Fujimori, *Nature materials* **4**, 57 (2005).
- [48] M. M. Deshmukh and D. C. Ralph, *Phys. Rev. Lett.* **89**, 266803 (2002).
- [49] L. Balents and R. Egger, *Phys. Rev. Lett.* **85**, 3464 (2000); *Phys. Rev. B* **64**, 035310 (2001).

- [50] M. Y. Veillette, C. Bena, and L. Balents, Phys. Rev. B **69**, 075319 (2004).
- [51] A. Jensen, J. Nygaard and J. Borggreen in *Proceedings of the International Symposium on Mesoscopic Superconductivity and Spintronics*, edited by H. Takayanagi and J. Nitta, (World Scientific 2003), pp. 33-37.
- [52] B. Zhao, I. Mönch, H. Vinzelberg, T. Mühl, and C. M. Schneider, Appl. Phys. Lett. **80**, 3144 (2002).
- [53] K. Tsukagoshi, B. W. Alphenaar, and H. Ago, Nature **401**, 572 (1999).
- [54] S. Sahoo, T. Kontos, J. Furer, C. Hoffmann, M. Gräber, A. Cottet, and C. Schönenberger, Nature Physics **1**, 102 (2005).
- [55] A. Cottet, T. Kontos, W. Belzig, C. Schönenberger and C. Bruder, cond-mat/0512176.
- [56] A. N. Pasupathy, R. C. Bialczak, J. Martinek, J. E. Grose, L. A. K. Donev, P. L. McEuen, and D. C. Ralph, Science, **306**, 86 (2004).
- [57] A. Kubetzka, M. Bode, O. Pietzsch, and R. Wiesendanger, Phys. Rev. Lett. **88**, 057201 (2002).
- [58] Y. Manassen, R. J. Hamers, J. E. Demuth, and A. J. Castellano, Phys. Rev. Lett. **62**, 2531 (1989).
- [59] C. Durkan and M. E. Welland, Appl. Phys. Lett. **80**, 458 (2002).
- [60] D. Mozyrsky, L. Fedichkin, S. A. Gurvitz, and G. P. Berman, Phys. Rev. B **66**, 161313 (2002).
- [61] J.-X. Zhu and A. V. Balatsky, Phys. Rev. Lett. **89**, 286802 (2002); Phys. Rev. B **67**, 174505 (2003).
- [62] L. N. Bulaevskii, M. Hruška, and G. Ortiz, Phys. Rev. B **68**, 125415 (2002).
- [63] L. N. Bulaevskii and G. Ortiz, Phys. Rev. Lett. **90**, 040401 (2003).
- [64] A. V. Balatsky, Y. Manassen, and R. Salem, Phys. Rev. B **66**, 195416 (2002).
- [65] J. König, H. Schoeller, and G. Schön, Phys. Rev. Lett. **76**, 1715 (1996); J. König, J. Schmid, H. Schoeller, and G. Schön, Phys. Rev. B **54**, 16820 (1996); H. Schoeller, in *Mesoscopic Electron Transport*, edited by L.L. Sohn, L.P. Kouwenhoven, and G. Schön (Kluwer, Dordrecht, 1997); J. König, *Quantum Fluctuations in the Single-Electron Transistor* (Shaker, Aachen, 1999).
- [66] Y. Meir and N. S. Wingreen, Phys. Rev. Lett. **68**, 2512 (1992).

- [67] G. D. Mahan in *Many particle physics* (Kluwer Academic / Plenum Publishers, 1990).
- [68] A. Brataas, Y. V. Nazarov, and G. E. W. Bauer, *Eur. Phys. J. B* **22**, 99 (2001).
- [69] D. H. Hernando, Y. V. Nazarov, A. Brataas, and G. E. W. Bauer, *Phys. Rev. B* **62**, 5700 (2000).
- [70] A. Brataas, Y. Tserkovnyak, G. E. W. Bauer, and B. I. Halperin, *Phys. Rev. B* **66**, 060404(R) (2002).
- [71] J. König, J. Martinek, J. Barnas, and G. Schön, in "CFN Lectures on Functional Nanostructures" *Lecture Notes in Physics* **658**, p.145-164, edited by K. Busch *et al.*, (Springer, 2005).
- [72] A.C. Hewson, *The Kondo Problem to Heavy fermions* (Cambridge Press, 1993).
- [73] J. Fransson, O. Eriksson, and I. Sandalov, *Phys. Rev. Lett.* **88**, 226601 (2002).
- [74] D. Weinmann, W. Häusler, and B. Kramer, *Phys. Rev. Lett.* **74**, 984 (1995).
- [75] A. K. Huettel, H. Qin, A. W. Holleitner, R. H. Blick, K. Neumaier, D. Weinmann, K. Eberl, and J. P. Kotthaus, *Europhys. Lett.* **62**, 712 (2003).
- [76] K. Ono, D. G. Austing, Y. Tokura, and S. Tarucha, *Science* **297**, 1313 (2002).
- [77] A. V. Khaetskii and Y. V. Nazarov, *Phys. Rev. B* **64**, 125316 (2001).
- [78] V. N. Golovach, A. Khaetskii, and D. Loss, *Phys. Rev. Lett.* **93**, 016601 (2004).
- [79] S. I. Erlingsson and Y. V. Nazarov, *Phys. Rev. B* **66**, 155327 (2002).
- [80] I. A. Merkulov, A. L. Efros, and M. Rosen, *Phys. Rev. B* **65**, 205309 (2002).
- [81] A. V. Khaetskii, D. Loss, and L. Glazman, *Phys. Rev. Lett.* **88**, 186802 (2002).
- [82] J. M. Kikkawa and D. D. Awschalom, *Phys. Rev. Lett.* **80**, 4313 (1998).
- [83] R. J. Epstein, D. T. Fuchs, W. V. Schoenfeld, P. M. Petroff, and D. D. Awschalom, *Appl. Phys. Lett.* **78**, 733 (2001).
- [84] D. Davidović, private communication.
- [85] Ya. M. Blanter and M. Büttiker, *Phys. Rep.* **336**, 1 (2000).
- [86] C. Beenakker and C. Schönenberger, *Physics Today* **56** (5), 37 (2003).
- [87] A. Thielmann, M. H. Hettler, J. König, and G. Schön, *Phys. Rev. B* **71**, 045341 (2005).
- [88] W. Belzig, *Phys. Rev. B* **71**, 161301(R) (2005).

- [89] A. N. Korotkov, Phys. Rev. B **49**, 10381 (1994).
- [90] S. Hershfield, J. H. Davies, P. Hyldgaard, C. J. Stanton, and J. W. Wilkins, Phys. Rev. B **47**, 1967 (1993).
- [91] U. Hanke, Yu. M. Galperin, K. A. Chao, and N. Zou, Phys. Rev. B **48**, 17209 (1993); U. Hanke, Yu. M. Galperin, and K. A. Chao, Phys. Rev. B **50**, 1595 (1994).
- [92] A. Thielmann, M. H. Hettler, J. König, and G. Schön, Phys. Rev. B **68**, 115105 (2003).
- [93] R. Lü and Z. R. Liu, cond-mat/0210350.
- [94] F. Elste and C. Timm, Phys. Rev. B **73**, 235305 (2006).
- [95] H. Birk, M. J. M. de Jong, and C. Schönenberger, Phys. Rev. Lett. **75**, 1610 (1995).
- [96] G. Kießlich, A. Wacker, E. Schoell, A. Nauen, F. Hohls, and R. J. Haug, Phys. Status Solidi C **0**, 1293 (2003).
- [97] A. Nauen, I. Hapke-Wurst, F. Hohls, U. Zeitler, R.J. Haug, and K. Pierz, Phys. Rev. B **66**, 161303(R) (2002).
- [98] E. Onac, F. Balestro, B. Trauzettel, C. F. J. Lodewijk, and L. P. Kouwenhoven, Phys. Rev. Lett. **96**, 026803 (2006).
- [99] R. Deblock, E. Onac, L. Gurevich, and L. P. Kouwenhoven, Science **301**, 203 (2003).
- [100] S. A. Gurvitz IEEE Transactions on Nanotechnology **4**, 1 (2005).
- [101] Ivana Djuric, Bing Dong, H. L. Cui, IEEE Transactions on Nanotechnology **4**, 71, (2005); J. Appl. Phys. **99**, 63710 (2006); Appl. Phys. Lett. **87**, 032105 (2005).
- [102] H. B. Sun and G. J. Milburn, Phys. Rev. B **59**, 10748 (1997).
- [103] G. Kießlich, A. Wacker, and E. Schöll, Phys. Rev. B **68**, 125320 (2003).
- [104] C. Flindt, T. Novotný, and A.-P. Jauho, Phys. Rev. B **70**, 205334 (2004); T. Novotný, A. Donarini, C. Flindt, and A.-P. Jauho, Phys. Rev. Lett. **92**, 248302 (2004).
- [105] R. Aguado and T. Brandes, Phys. Rev. Lett. **92**, 206601 (2004).
- [106] A. N. Korotkov and D. V. Averin, Phys. Rev. B **64**, 165310 (2001).
- [107] A. Shnirman, D. Mozyrsky, and I. Martin, Europhys. Lett. **67**, 840 (2004).



- [108] G. Johansson, P. Delsing, K. Bladh, D. Gunarsson, T. Duty, K. Käck, G. Wendin, and A. Aassime, cond-mat/0210163; *Proceedings of the NATO ARW "Quantum Noise in Mesoscopic Physics"*, edited by Y. V. Nazarov, (Kluwer, Dordrecht 2003), pp 337-356.
- [109] B. R. Bulka, J. Martinek, G. Michalek, and J. Barnas, Phys. Rev. B **60**, 12246 (1999); B. R. Bulka, *ibid.* **62**, 1186 (2000).
- [110] G. Johansson, A. Käck, and G. Wendin Phys. Rev. Lett. **88**, 046802 (2002); A. Käck, G. Wendin, and G. Johansson, Phys. Rev. B **67**, 035301 (2003).
- [111] S.A. Gurvitz Phys. Rev. B **57**, 6602 (1998); S.A. Gurvitz and Ya.S. Prager, Phys. Rev. B **53**, 15932 (1996).
- [112] S. A. Gurvitz, D. Mozyrsky, and G. P. Berman, Phys. Rev. B **72**, 205341 (2005).
- [113] R. Aguado and L. P. Kouwenhoven, Phys. Rev. Lett. **84**, 1986 (2000).
- [114] U. Gavish, Y. Levinson, and Y. Imry, Phys. Rev. B **62**, R10637 (2000).
- [115] H.-A. Engel and D. Loss, Phys. Rev. Lett. **93**, 136602 (2004); E. V. Sukhorukov, G. Burkard, and D. Loss, Phys. Rev. B **63**, 125315 (2001).
- [116] W. Shockley, J. Appl. Phys. **9**, 635 (1938); L. Fedichkin and V. V'yurkov, Appl. Phys. Lett. **64**, 2535 (1994).
- [117] A. Thielmann, M. H. Hettler, J. König, and G. Schön, Phys. Rev. Lett. **95**, 146806 (2005).
- [118] F. M. Souza, J. C. Egues, and A. P. Jauho, cond-mat/0209263; Brazilian J. of Physics **34**, 24 (2004).
- [119] L. D. Landau and E.M. Lifschitz, *Lehrbuch der theoretischen Physik III*, translated by G. Heber (Akademie Verlag Berlin, 1967)
- [120] W. G. van der Wiel, S. De Franceschi, J. M. Elzerman, T. Fujisawa, S. Tarucha, and L. P. Kouwenhoven, Rev. Mod. Phys. **75**, 1 (2003).
- [121] J. M. Elzerman, R. Hanson, J. S. Greidanus, vanBeveren, L.H. Willems, S. De Franceschi, L. M. K. Vandersypen, S. Tarucha, and L. P. Kouwenhoven, Phys. Rev. B **67**, 161308(R) (2003); J. R. Petta, A. C. Johnson, C. M. Marcus, M. P. Hanson, and A. C. Gossard, Phys. Rev. Lett. **93**, 186802 (2004).
- [122] F. R. Waugh, M. J. Berry, C. H. Crouch, C. Livermore, D. J. Mar, R. M. Westervelt, K. L. Campman, and A. C. Gossard, Phys. Rev. B **53**, 1413 (1996).
- [123] T. Fujisawa, T. Hayashi, H.D. Cheong, Y.H. Jeong, and H. Hirayama Physica E **21**, 1046 (2004).

- [124] V. N. Golovach and D. Loss, *Semicond. Sci. Technol.* **17**, 355 (2002); D. Loss and D.P. DiVincenzo, *Phys. Rev. A* **57**, 120 (1998).
- [125] M. Rontani, S. Amaha, K. Muraki, F. Manghi, E. Molinari, S. Tarucha, and D. G. Austing, *Phys. Rev. B* **69**, 85327 (2004).
- [126] D. Jacob, B. Wunsch, and D. Pfannkuche, *Phys. Rev. B* **70**, 081314(R) (2004); B. Wunsch, D. Jacob, and D. Pfannkuche, *Physica E* **26**, 464 (2005).
- [127] T. Hayashi, T. Fujisawa, H. D. Cheong, Y. H. Jeong, and Y. Hirayama, *Phys. Rev. Lett.* **91**, 226804 (2003).
- [128] L. P Kouwenhoven, D. G. Austing, and S. Tarucha, *Rep. Prog. Phys.* **64**, 701 (2001).
- [129] A. K. Hüttel, S. Ludwig, K. Eberl, and J. P. Kotthaus, *Phys. Rev. B* **72**, 81310 (2005).
- [130] T. H. Oosterkamp, S. F. Godijn, M. J. Uilenreef, Yu. V. Nazarov, N. C. van der Vaart, and L. P. Kouwenhoven, *Phys. Rev. Lett.* **80**, 4951 (1998).
- [131] R. H. Blick, D. Pfannkuche, R. J. Haug, K. v. Klitzing, and K. Eberl, *Phys. Rev. Lett.* **80**, 4032 (1998).
- [132] T. Brandes, *Physics Reports* **408**, 315 (2005).
- [133] Yu. V. Nazarov, *Physica B* **189**, 57 (1993).
- [134] H. Sprekeler, G. Kießlich, A. Wacker, and E. Schöll, *Phys. Rev. B* **69**, 125328 (2004).
- [135] S. A. Gurvitz, *Phys. Rev. B* **56**, 15215 (1997); S. A. Gurvitz, *Phys. Rev. B* **57**, 6602 (1998).
- [136] S.A. Gurvitz and Ya.S. Prager, *Phys. Rev. B* **53**, 15932 (1996).
- [137] T. H. Stoof and Yu. V. Nazarov, *Phys. Rev. B* **53**, 1050 (1996); B. L. Hazelzet, M. R. Wegewijs, T. H. Stoof, and Yu. V. Nazarov, *Phys. Rev. B* **63**, 165313 (2001).
- [138] N. C. van der Vaart, S. F. Godijn, Yu. V. Nazarov, C. J. P. M. Harmans, J. E. Mooij, L. W. Molenkamp, and C. T. Foxon, *Phys. Rev. Lett.* **74**, 4702 (1995).
- [139] T. Ota, K. Ono, M. Stopa, T. Hatano, S. Tarucha, H. Z. Song, Y. Nakata, T. Miyazawa, T. Ohshima, and N. Yokoyama, *Phys. Rev. Lett.* **93**, 066801 (2004).
- [140] J. Fransson and O. Eriksson, *J. Phys.: Condens. Matter* **16**, L85 (2004); J. Fransson and O. Eriksson, *Phys. Rev. B* **70**, 085301 (2004).
- [141] R. Ziegler, C. Bruder, and H. Schoeller, *Phys. Rev. B* **62**, 1961 (2000).
- [142] M. Tews, *Ann. d. Physik* **13**, 249 (2004).

- [143] K. Blum, *Density Matrix Theory and Applications*, 2nd ed., (Plenum Press, New York, 1996).
- [144] U. Hartmann and F. K. Wilhelm, Phys. Rev. B. **67**, 161307(R) (2003).
- [145] H. Schoeller and J. König, Phys. Rev. Lett. **84**, 3686 (2000).
- [146] K. Ishibashi, M. Suzuki, T. Ida, and Y. Aoyagi, Appl. Phys. Lett. **79**, 1864 (2001).
- [147] D. Pfannkuche, R. H. Blick, R. J. Haug, K. von Klitzing, and K. Eberl, Superlattices & Microstructures **23**, 1255 (1998).
- [148] R. I. Dzhioev, V. L. Korenev, I. A. Merkulov, B. P. Zakharchenya, D. Gammon, Al. L. Efros, and D. S. Katzer, Phys. Rev. Lett. **88**, 256801 (2002).
- [149] R. J. Epstein, D. T. Fuchs, W. V. Schoenfeld, P. M. Petroff, and D. D. Awschalom, Appl. Phys. Lett. **78**, 733 (2001).
- [150] N. P. Stern, M. Poggio, M. H. Bartl, E. L. Hu, G. D. Stucky, and D. D. Awschalom, cond-mat/0507699.
- [151] J. A. Gupa, D. D. Awschalom, X. Peng, and A. P. Alivisatos, Phys. Rev. B **59**, 10421 (1999).
- [152] A. V. Khaetskii and Y. V. Nazarov, Phys. Rev. B **61**, 12639 (2000).
- [153] T. Fujisawa, D. G. Austing, Y. Tokura, Y. Hirayama, and S. Tarucha, Phys. Rev. Lett. **88**, 236802 (2002).
- [154] J. M. Elzerman, R. Hanson, L. H. Willems van Beveren, B. Witkamp, L. M. K. Vandersypen, and L. P. Kouwenhoven, Nature **430**, 431 (2004).
- [155] D. Loss and D. DiVincenzo, Phys. Rev. A **57**, 120 (1998).
- [156] S. A. Crooker, D. G. Rickel, A. V. Balatsky, and D. L. Smith, Nature **431**, 49 (2004).
- [157] M. Oestreich, M. Römer, R. J. Haug, and D. Hägele, Phys. Rev. Lett. **95**, 216603 (2005).
- [158] R. J. Elliott, Phys. Rev. **96**, 266 (1954).
- [159] Y. Yafet, Solid State Physics, **14**, 1, (1963).
- [160] M. I. D'yakonov and V. I. Perel', Sov. Phys. JETP **33**, 1053 (1971).
- [161] M. I. D'yakonov and V. I. Perel', Sov. Phys. Solid State **13**, 3023 (1972).
- [162] S. I. Erlingsson, Y. V. Nazarov, and V. I. Falko, Phys. Rev. B **64**, 195306 (2001).

- [163] N. P. Stern, M. Poggio, M. H. Bartl, E. L. Hu, G. D. Stucky, and D. D. Awschalom, cond-mat/0507699.
- [164] J. A. Gupta, R. Knobel, N. Samarth, and D. D. Awschalom, *Science* **292**, 2458 (2001).
- [165] E. L. Hahn, *Phys. Rev.* **80**, 580 (1950).
- [166] R. J. Blume, *Phys. Rev.* **109**, 1867 (1958).
- [167] M. Kälin, I. Gromov, and A. Schweiger, *J. of Magnetic Resonance* **160**, 166 (2003).
- [168] W. D. Oliver, Y. Yu, J. C. Lee, K. K. Berggren, L. S. Levitov, and T. P. Orlando, *Science* **310** 1653, (2005).

## Acknowledgements

I want to thank all people contributing to this work. In first place, I thank my advisor, Prof. Dr. Jürgen König for his support in recent years. He gave me the possibility to work in his group, to present my work at numerous conferences, and introduced me to the world of science and academics.

Further, I thank Jan Martinek. Most parts of the thesis are the result of the close cooperation with him.

I appreciate a joint paper with Bernhard Wunsch, and Daniela Pfannkuche.

I thank all colleagues at TFP for my pleasant stay in Karlsruhe, and all members of TP3 in Bochum, especially Daniel Urban and Björn Kubala for lively discussion about life, the universe and the rest. I owe sincere thanks to Kerstin Ludwig, who rescued me from dealing with the bureaucracy in any possible way.

I thank J. Barnaś, G. E. W. Bauer, S. Debald, C. Flindt, D. Hägele, M. Hettler, M. Oestreich, D. Ralph, A. Thielmann, and W. Wetzels for valuable discussions.

Finally, I want to thank my wife Scrolan for her unconditional love and support, as well as for enduring this long period of spacial separation.

This work was supported by the Deutsche Forschungsgemeinschaft via SFB 491 and under the Emmy-Noether Program.



# Lebenslauf

**Name:** Braun

**Vorname:** Matthias

**geboren:** am 11. April. 1978 in Bamberg

**Familienstand:** verheiratet mit Scrolan Braun geb. Krov

**Eltern:** Hans-Joachim Braun und Roswitha Braun geb. Christmayr

**Schule:** Aug. 1984 – Juli 1988: Grundschule (St. Kunigund/Bamberg)  
Sept. 1988 – Juni 1997: Gymnasium (Dientzenhofer Gymnasium/Bamberg)  
Juni. 1997: Abitur

**Zivildienst:** 01. April. 1998 – 30. April. 1999: CVJM Jugendheim Altenstein

**Studium:** Okt. 1997 – Aug. 2001: Physik an der Universität Würzburg  
Aug. 2001 – Sep. 2002: Physik an der University of Texas at Austin  
Okt. 2000: Vordiplom  
Aug. 2002: Master of Arts (Physics)

**Master Thesis:** “Current induced modification of the magnon dispersion relation”,  
angefertigt bei Prof. A. H. MacDonald am “Department of Physics”  
der University of Texas at Austin

**Promotion:** Feb. 2003 – Sep 2003: Doktorand bei Dr. Jürgen König am “Institut  
für Theoretische Festkörperphysik” der Universität Karlsruhe (TH)  
Okt. 2003 – März 2006: Doktorand bei Prof. Dr. Jürgen König am  
“Institut für Theoretische Physik III” der Ruhr-Universität Bochum

